Assessing and Analyzing Near-Surface Radar Snow Accumulation Layers at Summit, Greenland

by

Thomas Buckmaster Overly

Submitted to the graduate degree program in Geography and the
Graduate Faculty of the University of Kansas
in partial fulfillment of the requirements for the degree of
Master's of Arts.

____
Dr. Xingong Li (Co-Chair)

____
Dr. David Braaten (Co-Chair)

____
Dr. Johannes Feddema

____
Dr. Cornelis van der Veen (Reader)

Date Defended: ________________

The Masters Committee for Thomas Buckmaster Overlycertifies
that this is the approved version of the following thesis:

Assessing and Analyzing Near-Surface Radar Snow Accumulation Layers at Summit, Greenland

Committee:

Dr. Xingong Li (Co-Chair)

Dr. David Braaten (Co-Chair)

Dr. Johannes Feddema

Dr. Cornelis van der Veen (Reader)

Date Approved: __________________

Abstract

High vertical-resolution 0.5-2 GHz frequency-modulated continuous-wave radar data collected near Summit on the Greenland Ice Sheet reveal continuous horizons connecting the GRIP and GISP2 deep ice cores. Traced radar horizons to 150 meters depth are compared to physical properties, age-depth relationships, and accumulation rates from ice cores near Summit. Having established the radar horizons as annual accumulation markers, a 350-year record of accumulation rate is derived and analyzed spatially and temporally. Accumulation characteristics such as spatial noise, long-term accumulation rate, and climate fluctuations are determined. Averaging accumulation across 1000-2000 m eliminates most spatial noise associated with small-scale surface perturbations, providing a good approximation of the local accumulation rate. Overall, a detailed record of accumulation is gained, indicating that near-surface radar surveys can take the place of shallow ice cores for examining accumulation history, improving knowledge of spatial and temporal variability, spatial and temporal noise, and other accumulation characteristics.

Acknowledgements

In chronological order:

Lee Dexter, Dawn Hawley, Tom Paradis, Cat Moody, City of Prescott AZ, Aric Stewart, Dad for driving the silver twinkie back, Mom for 617, Will, Bean, Nathan Rigney, SIPN, Jon, Michael, Ryan, Craig, Shaun, Michael and Darcy, Joe and Robin, Curt Sorensen, Xingong Li, David Braaten, William Blake, John Paden, Vijay Ramasami, John Paden, John Paden again, Geography FC, Kate Pickett, Heather Renee Putnam, Pannir Kanagaratnam, Joel Plummer, Chandini, J. Chris Brown, Torry Akin, Earl Frederick, Laakki Ramsøe, Sidse Larsen, Ashley Thompson, Soren Larsen, Tim Rink, Kelly Mason, Susanne Buchardt har vi overhovedet skinke på menuen? Dorthe for support, encouragement and layer tracing ideas, Thorbjörn Axelsson, Prasad Gogineni, Tommie Cassen, Steve Ingalls, Johan Feddema, Kyle Begole, Victor A. Jara-Olivares, John Ledford, Chris Allen, Claude Laird, Kees van der Veen, Logan Smith, Lawrence Memorial Hospital Oncology, Dr. Soule, Nurse Vic, Nurse Chris, my parents-again, my friends, J. Chris Brown, Hilary and Chris, Suesela Gogineni, Josh Long, Mark Hummer, Alyson Abel, Cheri Hamilton, Pete Shortridge, Denmark-America Foundation and Fulbright Commission, Susanne igen, Sune Olander Rasmussen, Dorthe igen, Centre for Is of Klima, Faezeh Nick, Bo Vinther, H.C. Steen-Larsen, Mai Winstrup, Anders Svensson, J.P., Jennifer, Chuck Kinney Jr., Ditte, Ashley, Stephan Fuchs, Ben Echeverria, Leigh Stearns, William Blake again, Anthony Hoch, Cameron Lewis, Ashley Thompson and Chris Gifford...

...all of you (and countless unmentioned) at various points either motivated, reignited, caused laughter, brought joy, expanded my perspective, berated and supported me when needed, or simply did your job to my benefit, or gave your time without expectation... This thesis is just a silly document. But also a timeline of growth, frustration, and perseverance. None of it is solely my own and for that I acknowledge and thank you.

This work would not exist without intrinsic and instrumental support from J. Chris Brown and Kees van der Veen. I dedicate this thesis to my brother Will and my parents, Orbie and Roberta Overly. Thank you for your unconditional love and perpetual support.

Contents

List of Figures

List of Tables

Chapter 1

Introduction

1.1 Background

Ice sheets and glaciers provide numerous ways to trace climate histories ranging from short term climate variations at local scales to coarser long term records representing global scale climate changes. Tracing the mass balance of an ice sheet is crucial to interpreting such records. In its simplest terms, ice-sheet mass balance refers to the interplay between inputs from snow accumulation and precipitation compared to outputs from ice flow, melting, and glacier calving. Accurate knowledge of the spatial distribution of snow accumulation on ice sheets is fundamental to understanding the past, present, and future ice-sheet mass balance changes [Frezzotti et al., 2007]. Snow accumulation on an ice sheet is an important input to numerical simulations and models used to reconstruct and forecast ice sheet dynamics [Frezzotti et al., 2007]. Previous accumulation records, derived from ice cores, snowpits, and stake forests, have limited spatial coverage [Fischer et al., 1995; Box et al., 2004]. More recent high vertical-resolution radar measurements augment the interpretation of ice cores and provide valuable information on ice sheet accumulation [Jacobel and Hodge, 1995; Dahl-Jensen et al., 1997; Spikes et al., 2004; Arcone et al., 2005; Frezzotti et al., 2005; Steinhage et al., 2005; Hawley et al., 2006; Eisen et al., 2008].

Since the early 1960s airborne radio-echo sounding (RES) has been used to obtain information on ice thickness of smaller glaciers as well as the Greenland and Antarctic ice sheets [Robin et al., 1969; Harrison, 1973; Paren and Robin, 1975]. In addition to the ice surface and the bedrock, a number of internal horizons in the ice are often seen in the recovered radar images. These reflections of electromagnetic waves generally occur where the complex dielectric constant changes [Hempel et al., 2000]. Complex dielectric constant is a value that refers to a mediums ability to store, dissipate, or transmit electric energy. Complex dielectric constant (ϵ) is comprised of two parts: the real permittivity (ϵ') and the imaginary part (ϵ'') [Eisen et al., 2007]. Changes in either of these may result in reflection of a radar pulse.

A number of researchers have investigated the origin of the sudden changes in the complex permittivity in ice and identified three major causes: changes in (1) density, (2) acidity, and (3) crystal-orientation fabrics [Robin et al., 1969; Harrison, 1973; Gudmandsen, 1975; Paren and Robin, 1975; Clough, 1977; Ackley and Keliher, 1979; Millar, 1981; Robin and Millar, 1982; Moore, 1988; Fujita and Mae, 1994; Jacobel and Hodge, 1995; Fujita et al., 1999, 2000; Hempel et al., 2000; Fujita et al., 2002; Arcone et al., 2004; Fujita et al., 2006; Eisen et al., 2007].

Despite various explanations for the cause of internal reflectors, a general consensus exists that the horizons represent former deposition surfaces and are therefore horizons of equal age known as isochrones [Gudmandsen, 1975; Bogorodsky et al., 1982; Arcone et al., 2004; Eisen et al., 2004; Kanagaratnam et al., 2004; Spikes et al., 2004]. In Greenland, isochrones can be traced continuously for hundreds of kilometers [Gudmandsen, 1975; Chuah et al., 1996]. These radar reflection horizons have been physically linked to ice-core profiles [Kanagaratnam et al., 2004; Spikes et al., 2004; Arcone et al., 2005; Frezzotti et al., 2005; Steinhage et al., 2005; Eisen et al., 2006, 2007]. Accurate ice core age and characterization of physical properties, connected to radar reflection horizons, allow for the timing and potential cause of the isochronal radar reflections to be determined. Prominent reflections horizons, dated using ice core records, can be used to compute accumulation rates.

The Polar Radar for Ice Sheet Measurement (PRISM) project at the University of Kansas has developed a ground based ultra-wideband radar (0.5–2 GHz) to detect near-surface internal horizons in ice sheets [Gogineni et al., 2007]. This thesis builds upon previous knowledge of internal layers, attempting to establish what the layers represent and how they might be useful in describing accumulation on the Greenland Ice Sheet. Throughout this thesis, the term “horizon” will refer to the dark stratified radar reflections, while “layer” refers to a dark horizon over a white horizon, winter over summer, thus an annual “layer”.

1.2 Near-Surface Radar Surveys

The frequency, bandwidth, and source signal of a radar system determine the possible detectable targets (internal horizons in this case) [Kingsley and Quegan, 1992]. A basic radar system transmits a radio pulse at the speed of light away from the radar and towards a target. The transmitted pulse is scattered by the target and reflected back to the radar. The delay in time, between the transmitted pulse and the reflection, or echo, received from the target, can be used to calculate the distance to the target, r (meters). This distance, or range to target, r, equals the speed of light (m/sec), c, multiplied by the time (seconds), τ, for the signal to travel the two-way distance between the target and the radar, divided by two (Equation 1.1) [Kingsley and Quegan, 1992; Kanagaratnam, 2002; Parthasarathy, 2003]:

$$r = \frac{c\tau}{2} \tag{1.1}$$

When detecting the range to multiple targets, the targets must be spaced at a distance greater than the distance traveled by the radar's pulse during transmission. Another way to describe distance between targets is using time. A target is detectable, or resolvable, if the time delay between the echoes from two targets is greater than the pulse duration, $\Delta\tau$. Radar resolution is established by the pulse duration. Pulse duration, $\Delta\tau$, is equal to one divided by the bandwidth, B, of the radar (Equation 1.2).

$$\Delta\tau = \frac{1}{B} \tag{1.2}$$

Inserting the radar's pulse duration from Equation 1.2 into Equation 1.1 gives the radar's resolution, Δr :

$$\Delta r = \frac{c\Delta\tau}{2} \tag{1.3}$$

Thus radar resolution refers to the minimum distance two targets must be spaced in order to resolve if there are two separate targets rather than one large target. Substituting Equation 1.2 into Equation 1.3 and rearranging gives Δr :

$$\Delta r = \frac{c}{2B} \tag{1.4}$$

The accuracy of the distance to a target, or range accuracy, depends on the bandwidth of the transmitted signal. In general, a wider bandwidth improves a radar's ability to detect targets Kingsley and Quegan [1992]. Figure 1.1, adapted from Kingsley and Quegan [1992], displays why the detection of targets varies with different bandwidths. Figure 1.1 (a) emits a single continuous tone and measures the phase of the echo to find a rough position for the detected horizon, but only Horizon 4 is detected. Figure 1.1 (b), a second frequency is added to the transmission to reduce ambiguities and improve the detection of targets. Adding further frequencies (more bandwidth) eliminated ambiguities in range and allows for the detection of all four horizons (Figure 1.1 (c)). In comparison to previous radar surveys, the great benefit of the radar used in this thesis is its wide bandwidth, 1.5GHz, spanning frequencies 0.5–2.0GHz. Inserting the actual values into Equation 1.4 gives Δr equal to a resolution of 0.10m:

$$\Delta r = \frac{c}{2B} = \frac{3 \times 10^8}{2 \times (1.5 \times 10^9)} = 0.10m \tag{1.5}$$

Several recent radar surveys focus on detecting horizons in the upper 100 meters of firn. A 100 MHz radar was used in Antarctica to resolve multiple horizons down to depths of 100 meters [Vaughan et al., 1999]. The radar's pulse length of 2.5 meters resulted in

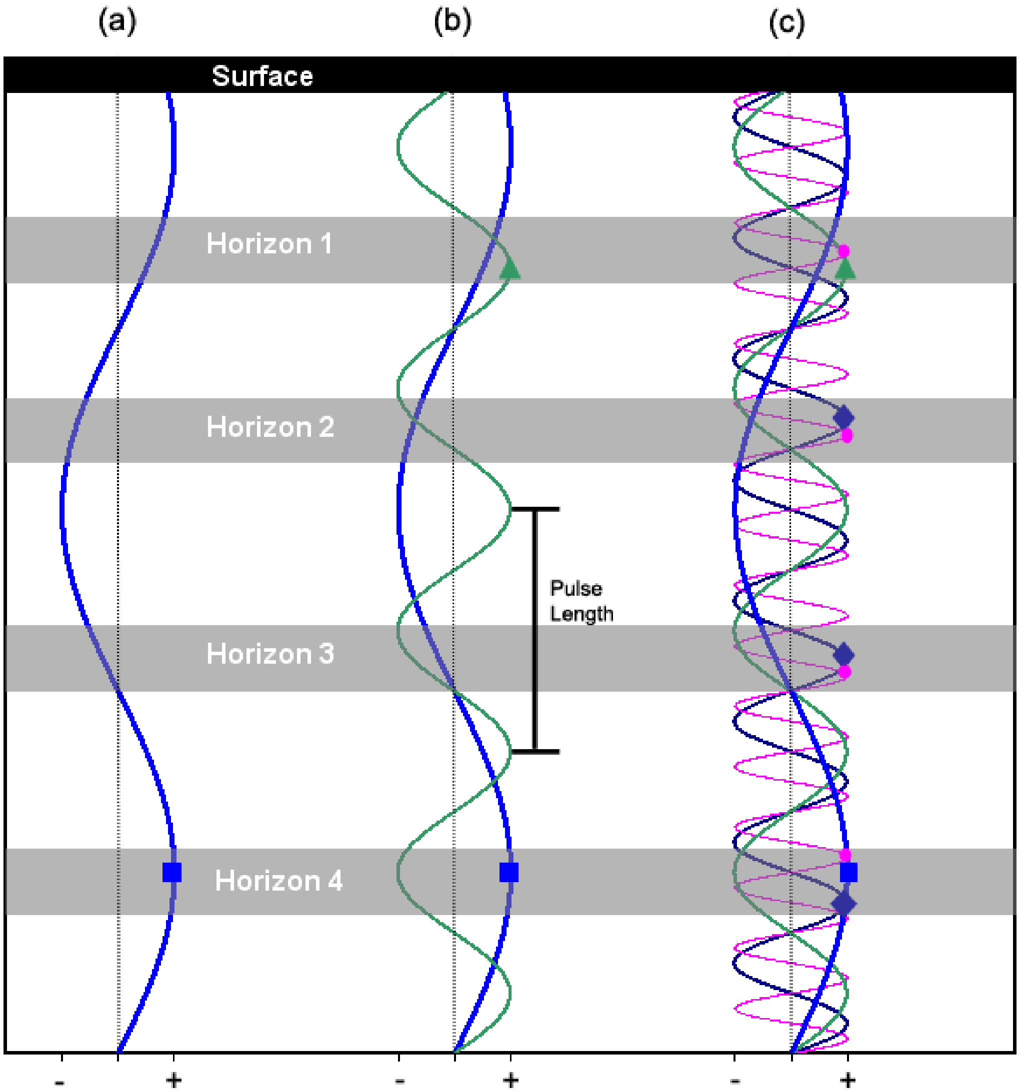

Figure 1.1: Radar bandwidth influence on range accuracy and resolution Targets are detected at the peak positive phase (or at a phase measurement of 90rom the path of the signal) of the pulse length. (a) With a single frequency, accuracy is poor and only Horizon 4 is detected. (b) With two frequencies (an expanded bandwidth), accuracy and ambiguity are improved, Horizons 1 and 4 are detected. (c) Using multiple frequencies (wide bandwidth), ambiguities are removed, accuracy is improved, and all four horizons are detected. Adapted from Kingsley and Quegan [1992].

interference from surrounding horizons, thus the horizons do not represent annual markers. Eisen et al. [2004] operated a radar at 200 and 250 MHz in Antarctica with a vertical resolution of one meter and depth penetration to 100 meters. From the surface down to seventy-five meters, five prominent reflection horizons were dated, with age uncertainties ranging from 8–21 years [Eisen et al., 2004]. Spikes et al. [2004] used a 400 MHz radar in

West Antarctica to detect stratigraphy down to 100 meters, with a 35-centimeter resolution. This spacing was generally greater than the separation of annual layers at the survey site, thus accumulation variability was determined on multi-decadal time-scales (25–48 years) using only the prominent horizons. Arcone et al. [2004] operated a 400 MHz radar in West Antarctica to trace stratigraphic continuity and variation in relation to accumulation and ice flow. The radar used in their study has a lower absolute bandwidth (300–500 MHz), with penetration to depths of seventy meters, and an interface resolution of 30–40 cm in firn. Arcone et al. [2005] tracked a limited number of prominent horizons at various depths down to fifty-six meters. Steinhage et al. [2005] used a 250 MHz system in Greenland to map internal structure down to 120 meters depth. The study does not explicitly state the radar's resolution, but based on the system specifications, it can be assumed to have a resolution of 0.5 meters. Seven strong reflection horizons were identified, dated, and tracked. Thomas (2008) identified several strong reflection horizons in the upper 100 meters of firn in Antarctica using a 200 MHz ground-based radar. Each of the surveys cited above resolve multiple near-surface horizons, but radar resolution was not high enough to observe annual layers. Hawley et al. [2006] were able to identify annual layers using high frequency airborne radar in Greenland. The radar's 13.5 GHz carrier frequency (1GHz bandwidth) reveals detailed annual accumulation layers, but to a limited depth of ten meters. So far, previous studies were limited either to resolving only the most prominent horizons in the upper 100 meters or seeing annual layer to a limited depth (approximately six annual layers to a depth of ten meters) [Hawley et al., 2006].

1.3 Internal Reflections in Near Surface Firn

As mentioned above, continuous internal reflections in ice are thought to potentially result from changes in density [Robin et al., 1969], conductivity [Paren and Robin, 1975], and crystal orientation fabric [Harrison, 1973]. Recent analysis suggests internal reflections in the upper firn may be dependent on a combination of density, conductivity, and radar frequency. Fujita et al. [1999, 2002], using 60 MHz and 179MHz radars, state that the upper 700 m of the ice sheet is dominated by the stratified changes in permittivity [Fujita et al., 1999, 2002]. Fujita et al. [2002] found that the upper 700 m of the ice sheet is dominated by the stratified changes in permittivity, in agreement with Fujita et al. [1999]. Permittivity related to density might explain all scattering above 700 m because it is known that density changes are caused by trapped air in ice down to depths of 500-1000 m [Fujita et al., 2002]. Arcone et al. [2004], using a 400 MHz radar, found density contrasts that persist well into the firn. Thin (1-2 mm) ice layers in concurrently drilled ice cores and widespread hoar and/or thin ice layer formation events are possible explanations for the reflection horizons observed at depths where compaction should decrease density contrasts [Arcone et al., 2004]. Arcone et al. [2005] argued that horizon variations are consistent with the stratification processes caused by the post-depositional snow metamorphosis and sublimation that form couplets of hoar and ice. Core density profiles by Arcone et al. [2005] confirmed that the firn/ice transition was reached at only thirty-eight meters depth after weak radar reflections were observed at similar depths.

Specific radar frequencies may respond to different feature of the upper ice sheet. The established frequency to ensure that the radar reflections result from fluctuations in conductivity is 10 MHz or less, whereas a frequency of about 300 MHz or more is needed to ensure that the radar reflection corresponds to fluctuations in permittivity [Matsuoka et al., 2002]. The previous radar surveys reviewed in Section 1.2 used frequencies ranging from 100 MHz to 13.5 GHz, thus the reflections in these surveys are likely related to density, though most surveys cited only refer to the horizons as isochronal (being of the same age or deposited at the same time). Given that the horizons are isochronous, chemically caused conductivity changes may produce reflection horizons that can be sensed by low-frequency radars (Arcone et al., 2005). Variations in conductivity, related to acidity, dominate reflection returns only when radar frequency is below 60MHz, much lower than the 0.5-2.0GHz frequency radar that produced the data used in this thesis [Fujita and Mae, 1994]. Crystal orientation fabric only influences reflections at depths where changes in crystal fabric could occur (500-1000m), much deeper than the 150 m depths explored by this thesis [Fujita et al., 1999, 2002; Matsuoka et al., 2002; Eisen et al., 2007]. Thus, based on previous research, conductivity and crystal-orientation fabric, two factors known to change dielectric constant in snow and ice, seemingly have limited influence on the reflection horizons detected in this thesis. Yet, Eisen et al 2008, concede that "some uncertainty about how material properties in firn combine to form continuous reflecting horizons" [Eisen et al., 2008]. Addressing the combined role of density, conductivity, and crystal-orientation fabric upon ice's dielectric constant is beyond the scope of this work. Given the findings by Fujita et al. [2002]; Arcone et al. [2004]; Eisen et al. [2008], the high frequency of the PRISM Accumulation radar (0.5–2GHz), and the moderate depth of the radar data (200 m) [Parthasarathy, 2003; Kanagaratnam et al., 2004; Gogineni et al., 2007], the majority of the radar horizons are assumed to be density related. A brief summary on the density of snow/firn follows.

1.4 Snow/Firn Properties

Newly fallen snow typically has a density ranging between 50–70 kg/m^3 [Paterson, 1994]. Each layer of snow that falls on the Greenland ice cap is buried by subsequent snow falls and is gradually compressed by the weight of the overlying layers. Initial density changes are primarily caused by the rounding and settling of the individual grains, with the processes of recrystallization and deformation dominating subsequent densification [Colbeck, 1983]. The stage between snow and ice is called firn. The transition from firn to ice occurs at a density of 830 kg/m^3 when interconnecting air passages are closed off and air is only present in closed bubbles. A further increase in density to 917 kg/m^3 happens when the air in the bubbles is compressed. The rate of transformation from snow to ice depends on temperature and accumulation rate and is thus site specific. In central Greenland the transition from firn to ice is typically found at a depth of about seventy meters [Paterson, 1994].

The weight of overlying accumulation is not the only action by which layers increase in density. Icy layers, or crusts, form under many conditions that may be affected by precipitation, temperature and wind conditions. Sub-surface or surface heat fluxes and summer insolation can cause layers to change density and structure, forming depth hoars, while high winds may cause icy crusts to form. Hoar layer formation is caused by sublimation of ice crystals when temperature gradients between surface air and near-surface layers are large [Pfeffer and Mrugala, 2002]. Water vapor is exchanged from grain to grain, redistributing the density of the layers [Colbeck and Jamieson, 2001]. During periods of strong wind, kinetic energy is absorbed by the surface layer in the form of heat when ice and snow crystals blow across the surface of the ice sheet. This heating can cause a slight film of water, which freezes to form a thin ice crust [Steffen et al., 1999]. In addition to effects from heat flux and wind, firn density is dependent on initial particle size. The initial size or shape of the snow crystals may influence the rate at which particles combine to form larger particles. Intricately branched crystals have a large ratio of surface area to volume meaning intricate crystals have a large amount of potential energy compared to spherical or columnar shaped crystals and thus require greater energy to be reduced to a rounded particle of ice [LaChapelle, 1992].

1.5 Research Questions

In comparison to previous studies, PRISM radar significantly improves vertical measurement resolution while increasing the depth at which radar reflections are visible. Operated near Summit, Greenland, the radar resolves near-surface internal horizons to a depth of 150 meters with 10 centimeter free-space resolution [Parthasarathy, 2003]. Radar transects connecting the GRIP and GISP2 ice cores reveal continuous reflection horizons that may contain previously unknown variations in snow accumulation. Using the radar, this thesis will address the following questions:

1. Do the horizons represent annual snow accumulation?
2. Can the horizons be linked to specific physical properties (volcanic events, seasonal dust, density contrasts)?
3. How representative are ice cores of the surrounding layer data?
4. Can the accumulation layers be tied to the GRIP and GISP2 ice cores?

5. How does accumulation vary spatially and temporally?

1.6 Summary of Methods

This thesis examines high vertical-resolution radar data collected near Summit on the Greenland Ice Sheet. The continuous reflection horizons revealed by the radar are analyzed to determine if the horizons represent an annual signal that can be linked to physical properties. Ice cores drilled near the site of the radar data are a key component in dating and evaluating the reflection horizons in order to address Question 1. Deep ice cores and shallow cores properties such as electrical conductivity measurements (volcanic/acidity), $\delta^{18}O$, dust, and visual stratigraphy, will be directly compared to the radar horizons to determine if the layers represent annual snow accumulation. These comparisons also address Question 2, the hypothesis that the horizons can be tied to physical properties. Establishing the horizons as annual markers and connecting these horizons to physical properties in ice cores allows for the investigation of the three remaining research questions: Question 3, how representative are ice cores of the surrounding layer data? Question 4, can the accumulations layers be connected to the GRIP and GISP2 ice cores? Question 5, how does accumulation vary spatially and temporally? The previous comparisons of ice core and radar data indirectly tackle question 4, of tying the layers to the GRIP and GISP2 ice cores. Examining the standard deviation of accumulation rates at varying distances from the ice cores will determine how well ice cores represent surrounding layer data and how accumulation varies spatially, addressing questions 3 and 5. Spatial and temporal variability of accumulation is also addressed by comparing horizon perturbations and layer thickness variations to previous studies of surface roughness by Van der Veen et al. [1998, 2009]. This connection is examined further by comparing the radar-derived accumulation rate to the accumulation rates at GRIP and GISP2. Moving averages of annual accumulation rate and standard deviation of accumulation will be compared between radar and ice core data in order to assess temporal variability and long-term trends of accumulation.

Chapter 2

Data and Methods

2.1 Study Area

The Greenland Environmental Observatory (GEOSummit) on the Greenland Ice Sheet (72°34' N, 38°29' W, 3250 meters elevation, Figure 2.1) was established in 1989 by the U.S. National Science Foundation (NSF) and the Danish Commission for Scientific Research in Greenland [University of California-Merced, 2008]. Located atop 3200 m of ice and nearly 400 km from the nearest point of land, the multidisciplinary facility is home to research campaigns which take advantage of the unique location of the observatory. Since 1989, when the GISP2 ice-coring activities began, the site has hosted numerous atmospheric and glaciological investigations [University of California-Merced, 2008] to further research on the Greenland Ice Sheet. Radar data used in this study was collected near GEOSummit over a four-day period from July 20 and July 23, 2005. Eight radar transects, approximately thirty kilometers in length each, were taken connecting the joint European Greenland Ice Core Project (GRIP) [Survey, 1997] and GISP2 ice cores. In addition to the GISP2 and GRIP deep ice cores, several shallow cores (ranging from 16m to 100m depth) drilled by Ohio State University (Summit Cluster cores) and the Desert Research Institute (cores named D4, Katie, Sandy, and Summit99) are used for comparison to the radar data (Figure 2.2).

Temperatures near the summit of the ice sheet remain well below freezing year-round, limiting major seasonal melting. Infrequent melt layers result from wind crusts or abnormally warm or intense radiation days. For the period 1991-2000, the Summit region had a winter mean temperature of -40.9 °C, a summer mean temperature of -14.9 °C, with an annual average temperature of -29.7 °C [Box, 2002].

Bromwich et al. [1993] demonstrated that changes in snow accumulation in central Greenland over the period 1963–1988 were controlled primarily by precipitation rates as reflected in changes in the strength and position of the dominant storm tracks over the region, with little relation to temperature. Kapsner et al. [1995] support these findings, concluding that snow accumulation in central Greenland is controlled primarily by atmospheric dynamics rather than by temperature. The major climate influences for the Summit region relate to circulation of and changes in frontal systems in the north Atlantic

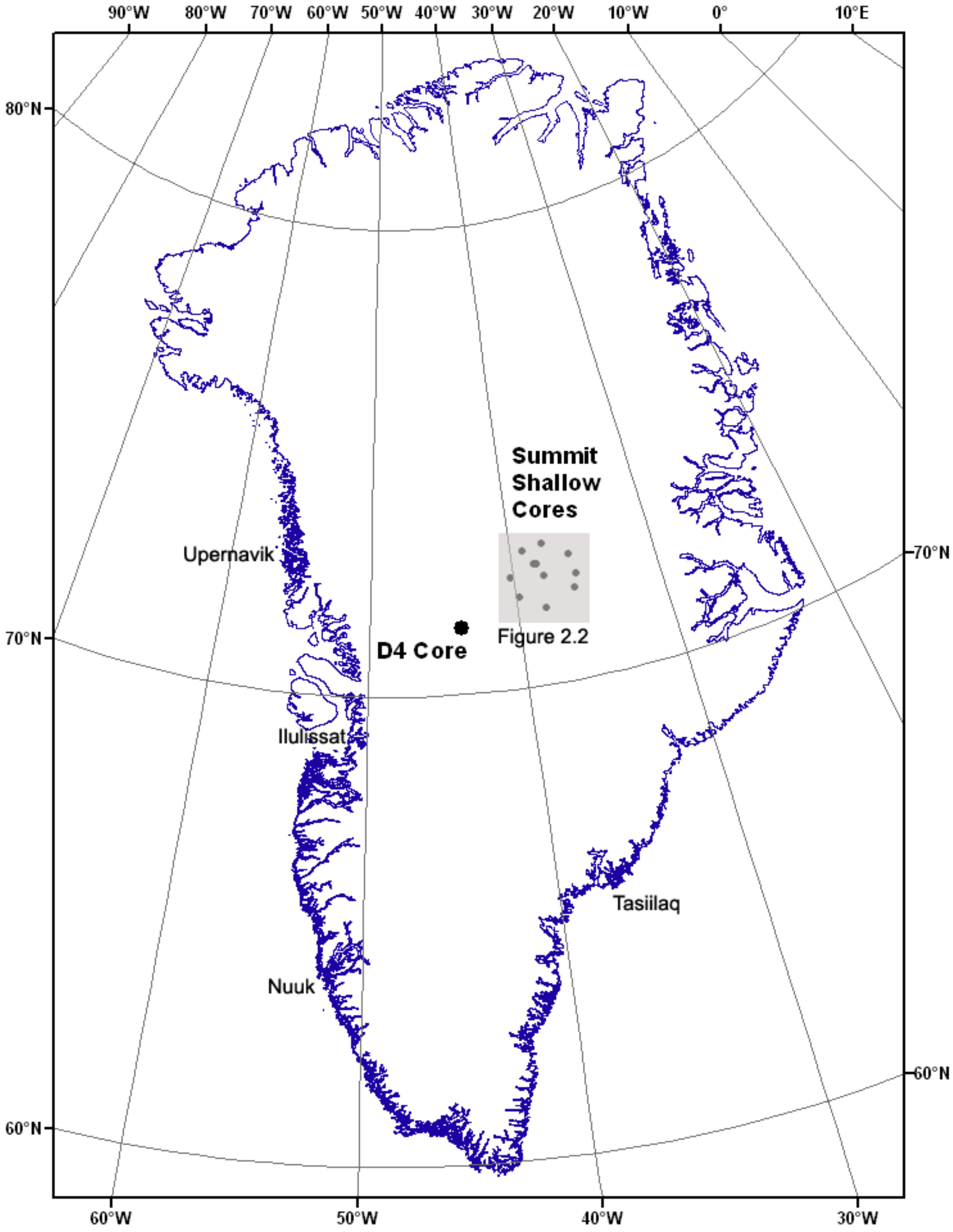

Figure 2.1: Greenland ice cores used in this study
Fourteen of the fifteen ice core records used in this study (see Table 2.1) are found near the summit of the Greenland Ice Sheet. The GRIP and GISP2 deep ice cores and the Ohio State University and Desert Research Institute shallow cores can be viewed in detail on the Summit Region Map (Figure 2.2). Physical properties of the D4 shallow core are compared to the radar (Section 3.2.3)

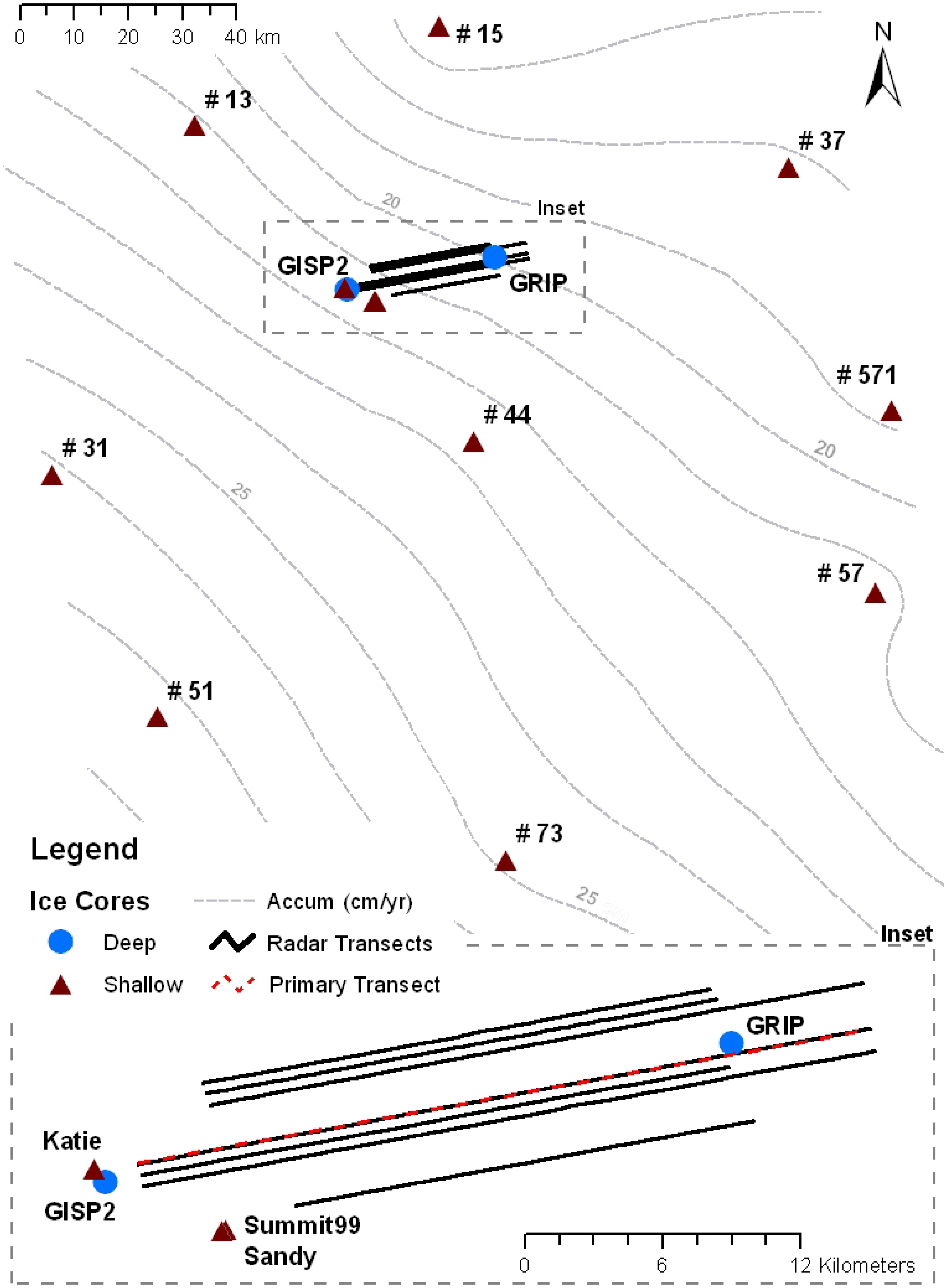

Figure 2.2: Radar transects and ice cores in the Summit region
Traced layers and derived accumulation rates are based on the primary transect (dashed red line). Accumulation contours adapted from Accumulation contours adapted from Van der Veen et al. [2001]. See Table 2.1 for full description of the ice cores used in this thesis.

region. The position of the Arctic frontal system, combined with katabatic winds, acts as a prevailing blocking high, preventing humidity transports to central Greenland [Dethloff et al., 2002]. Generally, when the North Atlantic Oscillation (NAO) is positive, stronger westerlies reduce the southwesterly flow that brings moisture to Greenland resulting in an overall average reduction of accumulation. Conversely, when NAO is negative, the large-scale atmospheric flow is from the southwest bringing more moisture to the ice sheet, particularly the southern region [Mosley-Thompson et al., 2005]. Mosley-Thompson et al. [2005] find very low correlation between NAO and net annual accumulation at Summit, and conclude that the NAO's influence on net accumulation over the Greenland ice sheet is spatially and temporally variable.

The long-term accumulation rate in the Summit region, derived from the GRIP and GISP2 deep ice cores and the OSU cores, gradually increases from east to west away from the ice divide [Bolzan and Strobel, 1994] (Figure 2.2). Both ice cores are located west of the ice divide, with accumulation at GRIP (0.230 m/yr) slightly lower than GISP2 (0.245 m/yr) [Dahl-Jensen et al., 1993; Meese et al., 1994]. The elevation of the radar transect decreases from east to west, decreasing from 3230 m at the GRIP core to 3211 m at GISP2 (Figure 2.3).

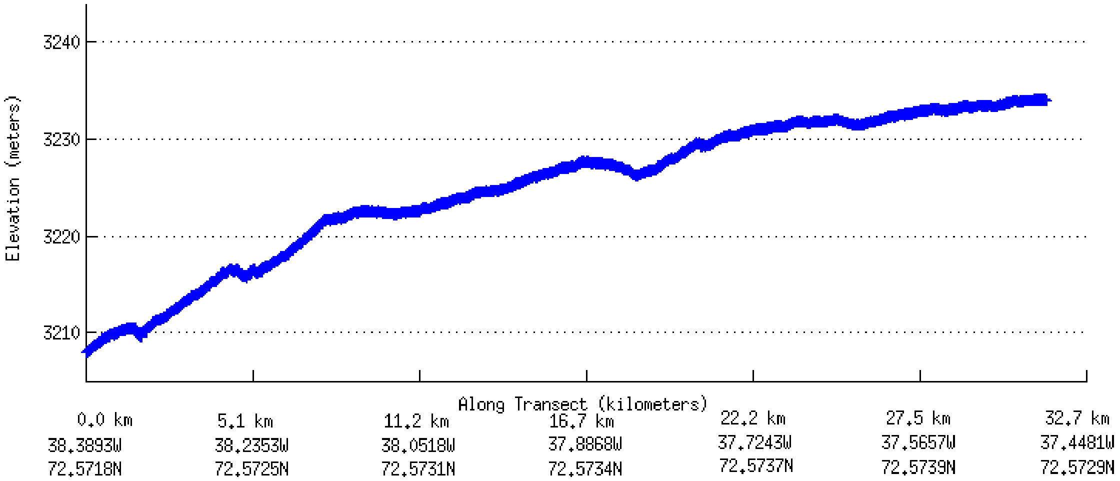

Figure 2.3: Elevation along primary radar transect
Elevation profile of primary radar transect from differentially corrected GPS. GISP2 is on the left hand side (West end) of the transect. GRIP is approximately 28 km to the east on the right hand side of the figure.

2.2 Accumulation Radar and Data

The accumulation radar implements a frequency-modulated continuous-wave (FM-CW) design, operating at frequencies of 0.5–2 GHz to obtain 10 cm free-space vertical resolution. In FM-CW radar, the transmitted signal's frequency is gradually increased or decreased (hence "modulated") with time (called the sweep time). During transmission, the echoes are received by the receiver and mixed with the transmit signal, and the result is low-pass filtered to produce a superposition of beat frequencies (or beat signal). The frequency of transmit and received signals will be different because of time delay, which is directly proportional to the range, associated with signal propagation to the target and back. Figure 2.4 shows a transmit signal, and its return from a point target.

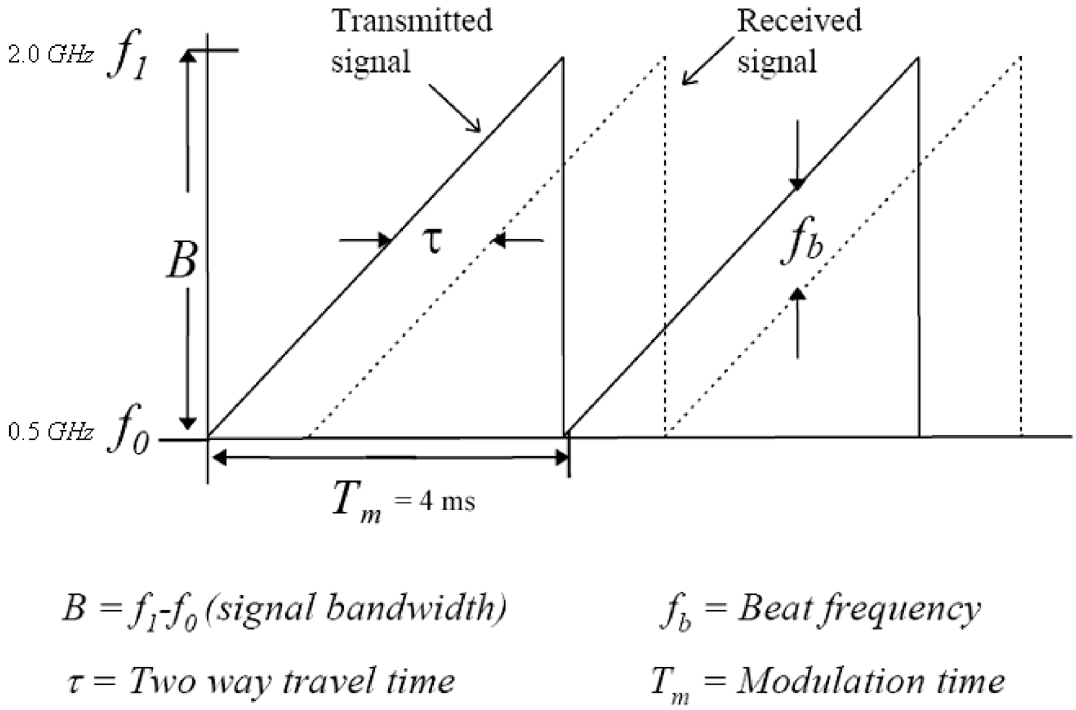

Figure 2.4: FM-CW radar concept
A transmit signal (solid line), and return signal (dotted line) from a point target. The two-way travel time is τ, the bandwidth of the transmit signal is *B*, the modulation time (or sweep time) is *Tm*. The frequency of this signal is given by *fb*, the beat frequency. The radar used in this thesis has a bandwidth of 1.5 GHz, ranging from 0.5–2.0 GHz, over a period, or sweep time, of 4 milliseconds [Parthasarathy, 2003].

The two-way travel time is τ, the bandwidth of the transmit signal is B, the sweep time is T, and the period is Tm. Multiplying two signals results in a sum and difference terms, and after low pass filtering, only the difference term remains. The frequency of this signal is given by fb, the beat frequency. A full description on the FM-CW radar used in this thesis can be found in [Parthasarathy, 2003].

The radar range (distance, or range/depth) to target, r, equals the speed of light, c, multiplied by the time, τ, for the signal to travel the two-way distance between the target and the radar, divided by two (Equation 1.1) [Kingsley and Quegan, 1992; Kanagaratnam, 2002; Parthasarathy, 2003]. The change in range, or vertical resolution of the radar Δr, equals the speed of light, c, multiplied by $\Delta\tau$ divided by two (Equation 1.3). The minimum separation between targets, $\Delta\tau$, that the radar can resolve is equal to one divided by the bandwidth, B, of the radar (Equation 1.2). Substituting for $\Delta\tau$ to solve Δr and then inserting the actual values gives Δr equal to the speed of light (3×10^8 m/sec) divided by two times the bandwidth of the radar (1.5×10^9), or $\Delta r = 0.10$m (Equation 1.5).

2.3 Radar Data Processing

The accumulation radar data collected was stored in the form of binary files. The data processing software developed in this thesis adapts processing and display algorithms developed by Kanagaratnam (2002) for use specifically with the radar system. Additional algorithms were developed to process the raw data, display the processed data, trace accumulation layers, and perform statistical analysis on the layer data. All algorithms were developed in Matlab and must be run in the Matlab operating environment. The end product maps near-surface horizons processed using mathematical domain transformations, system effect deconvolution, as well as image processing techniques such as median filtering. A full description of the processing methods used is given in Kanagaratnam (2002). The resulting radar data matrix contains reflection intensity values of changes in the snow's permittivity. Each column of data in the matrix represents 100 coherently averaged radar pulses down through the snow/ice (Figure 2.5b). The imaged reflection intensity in Figure 2.5d is a useful way for visualizing permittivity changes and therefore the internal layers of the ice sheet. The busy color scheme of Figure 2.5d, which shows the range of reflection intensity in volts, is simplified to a gray-scale image which emphasizes the alternating horizons (Figure 2.6). In this thesis, an individual black horizon roughly corresponds to the cold winter season of a year, while a white horizon represents the relatively warmer months of a year. A "layer" refers to both a white and black band of data. Traced "horizons" refer to the black intensely reflecting data. The darkest part of the horizon approximately represents the winter minima while the summer maxima occurs somewhere in the middle of the white horizons. Thus a calendar year is represented by the combination of both a dark and light horizon, forming an annual accumulation layer (the basis for calling these "layers" annual is presented in Section 3).

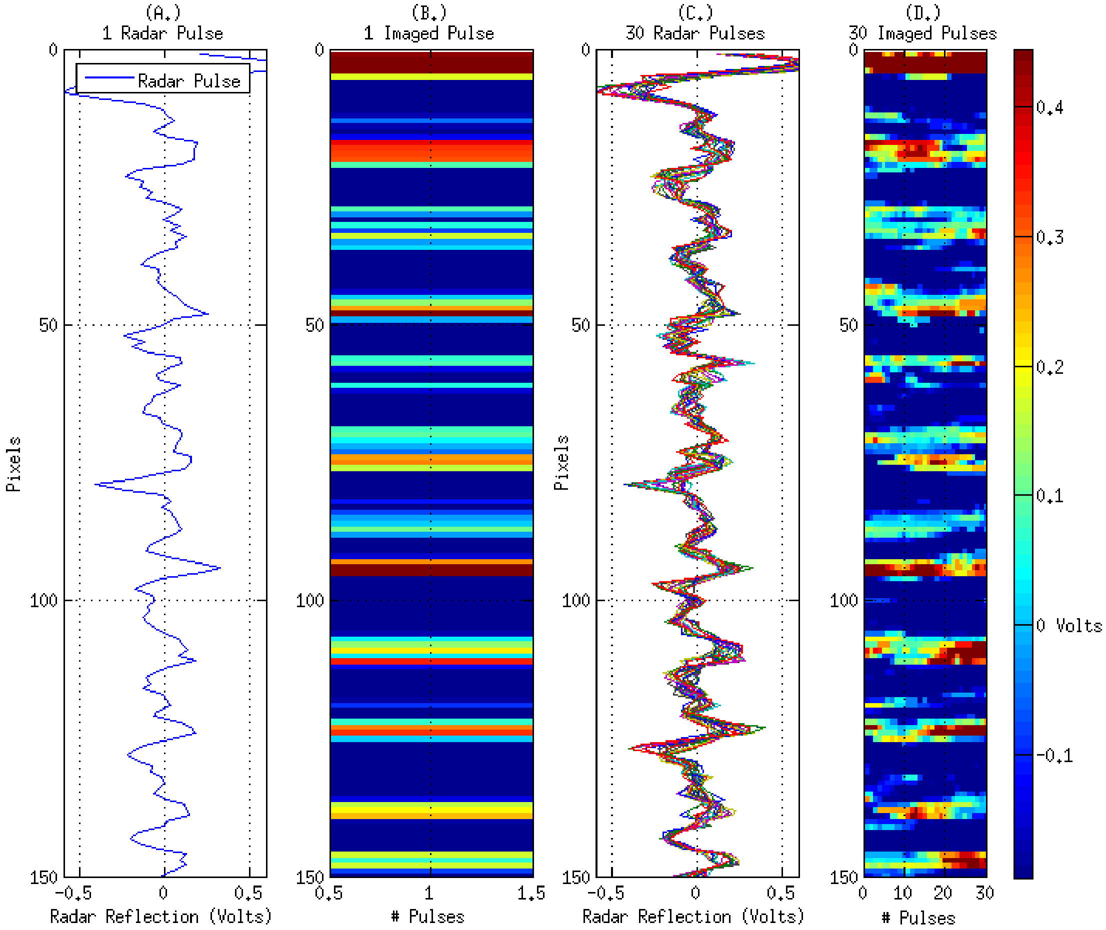

Figure 2.5: Displaying processed radar data
(a.) Reflection intensity of a single processed radar received signal (pulse); 150 rows of a single column of data are plotted; on the y-axis, 0 represents the surface of the ice sheet. (b.) Imaged reflection intensity of single radar pulse (c.) Reflection intensity of 30 radar pulses; 30 columns x 150 rows of data. (d.) Imaged reflection intensity of (c); the 30 pulses represent ∼81 meters horizontal distance across and ∼6 meters depth.

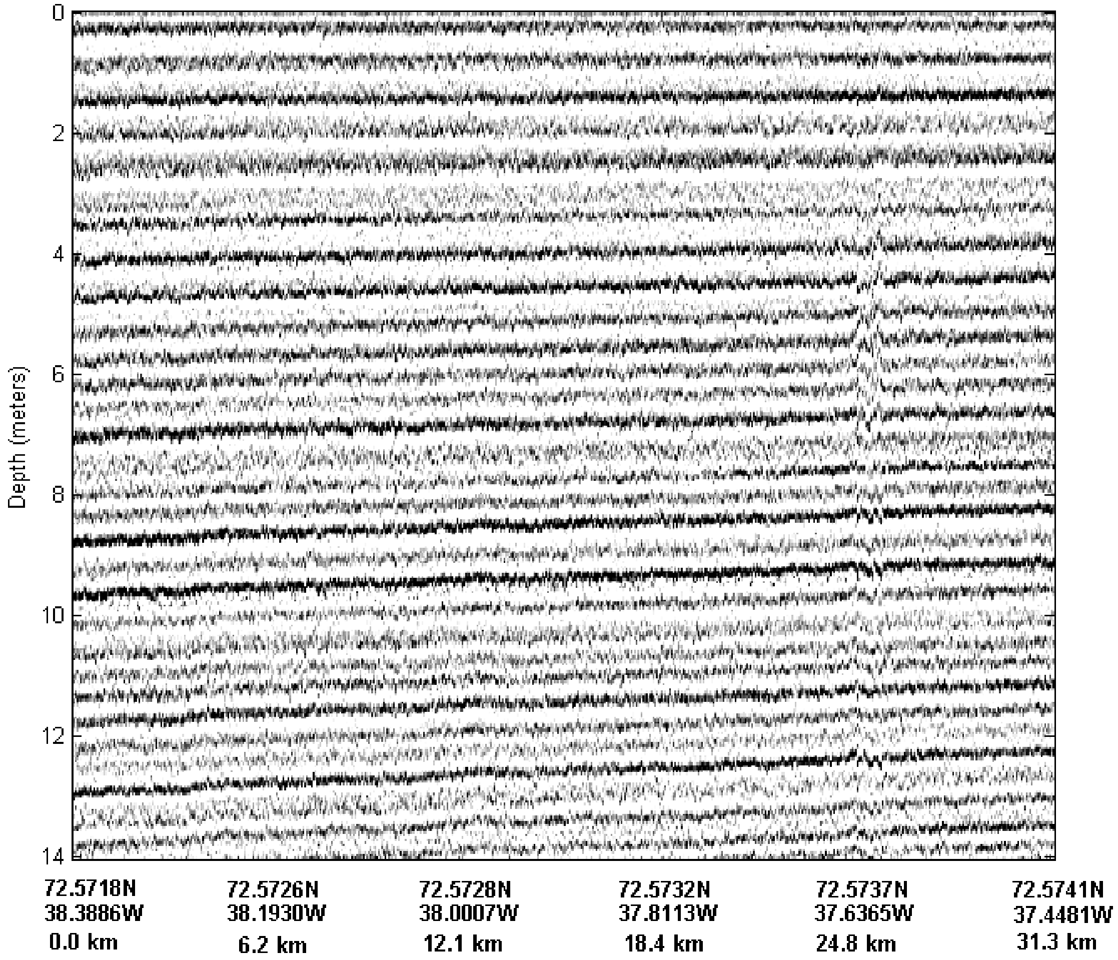

Figure 2.6: An example of processed radar layers
Radar reflection returns across the transect are displayed using a gray color scale. A "layer" refers to both a dark (winter) and light (summer) horizon. The image displays the primary transect (Figure 2.2), from around GISP2 on the left to eastward to GRIP on the right.

2.4 Horizon Tracing and Depth Calculation

2.4.1 Depth Calculation

As discussed in Section 1.3 Eisen et al. [2002], Kovacs et al. [1995], Robin et al. [1969], and others, have shown that the dielectric constant can be related to snow density. The rate at which the radar signal travels through the snow/ice is derived using established permittivity values for snow/ice and density data taken from ice cores (Figure 2.7).

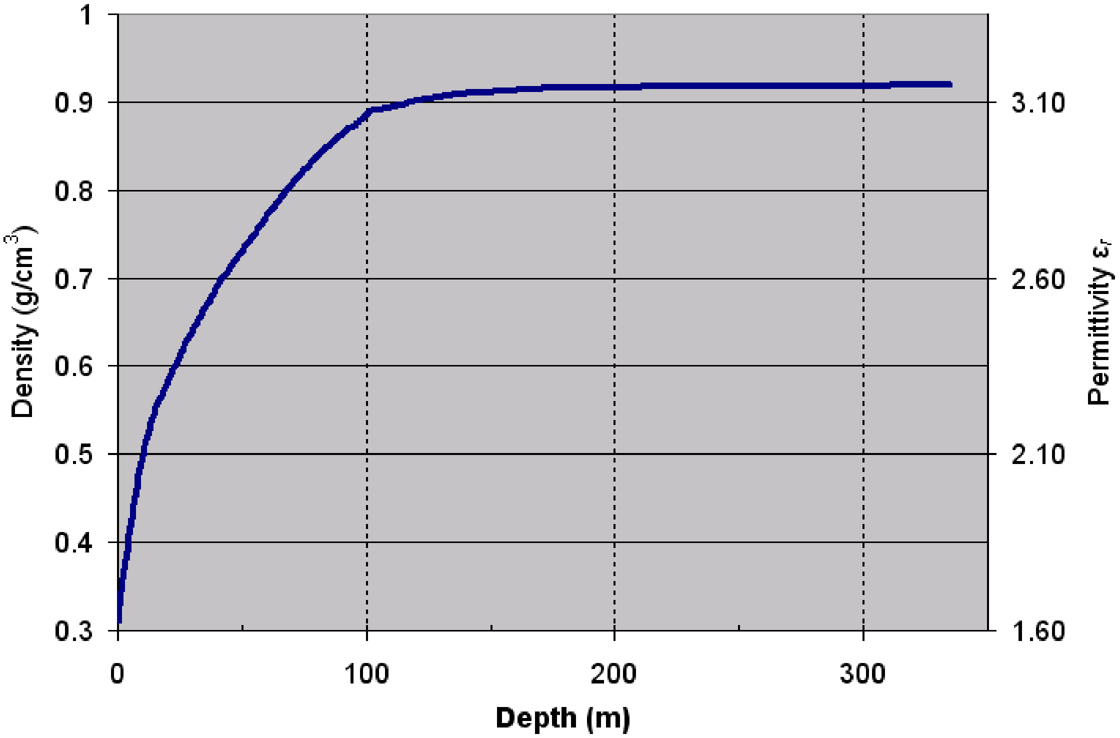

Figure 2.7: Composite density and calculated permittivity ϵ_r vs. depth
A composite density record extending to a depth of 300 meters compiled from four records [Bolzan and Strobel, 1994; GISP2, 1997a,f; Vinther, 2008b]. Inserting density values (left vertical axis) into Equation 2.2 gives permittivity, ϵ_r (right vertical axis).

The relationship between density and dielectric constant ϵ_r (also known as the relative complex permittivity) is depicted in Figure 2.7 and defined by Kovacs et al. [1995] as:

$$\epsilon_r = (1 + 0.845\rho)^2 \tag{2.1}$$

where ρ is the density of snow in g/cm^3. Using Equation 2.1, the density information was converted into a depth versus dielectric constant profile. The velocity of the signal (electromagnetic energy) is defined by the following equation:

$$v = \frac{c}{\sqrt{\epsilon_r}} \tag{2.2}$$

where c is the speed of light and ϵ_r is the permittivity of snow/ice. Multiplying the velocity of the signal by the two-way time (τ) of the radar gives the range/depth profile of the radar:

$$r = \frac{c}{\sqrt{\epsilon_r}} \times \frac{\tau}{2} \tag{2.3}$$

Connecting Equation 2.3 to physical space, the permittivity (ϵ_r) of the target medium influences the speed of the radar signal through that medium. Snow, which has a lower density than ice, permits the radar signal to travel faster through snow compared to ice. Thus, if the target medium is snow, $\epsilon_r = 1.6$, the vertical space represented by a pixel is 0.0483m. If the target medium is ice, $\epsilon_r = 3.17$, the vertical space represented by a pixel is 0.0343m (Figure 2.8 and Figure 2.9 for visualization of the difference in ϵ_r).

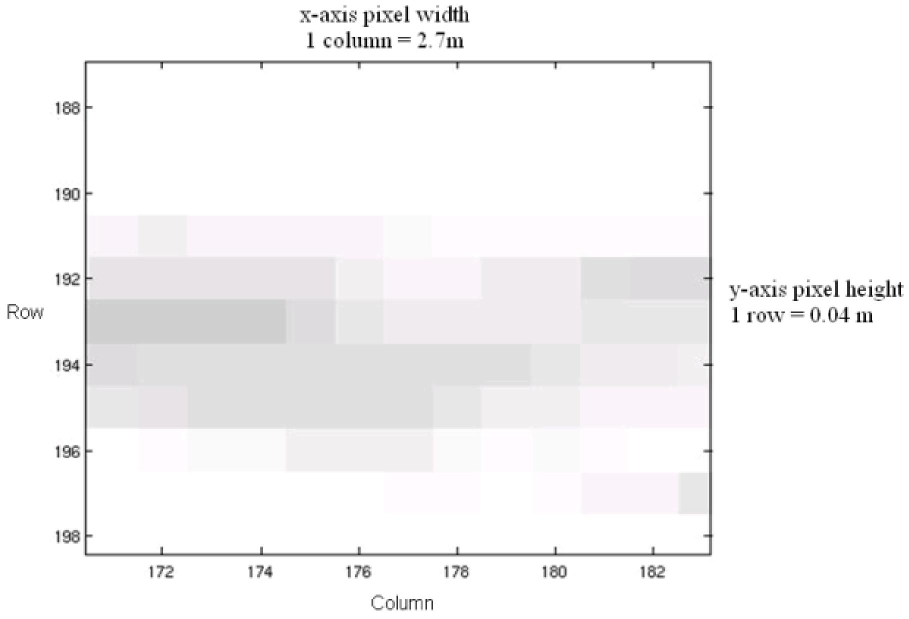

Figure 2.8: Pixel view of accumulation radar data
Using the above equations and the permittivity of snow, $\epsilon_r = 1.6$, the vertical distance along a pixel's y-axis is ~0.04m. Each column along the x-axis represents 100 coherently averaged radar pulses averaged over an approximate distance of ~2.7 meters horizontal distance per pixel.

The established range/depth profile is applied at each progressive depth to the composite density record (Figure 2.7) [Bolzan and Strobel, 1994; GISP2, 1997a; GRIP, 1997a; Vinther, 2008b] to produce a slightly non-linear depth scale (Figure 2.9). This calculated depth scale, r, is an improvement upon previous PRISM calculated depth scales [Kanagaratnam, 2002; Parthasarathy, 2003], which used a constant ϵ_r for the entire ice sheet (either $\epsilon_r = 1.6$, treating the entire snow/ice column as snow, or $\epsilon_r = 3.17$, treating the entire snow/ice column as ice). Rink (2006) used a variable ϵ_r derived from snow pits and ice cores to create a shallow depth/range profile [Rink, 2006]. The variable ϵ_r approach is applied in this thesis using density data from various shallow and deep ice cores.

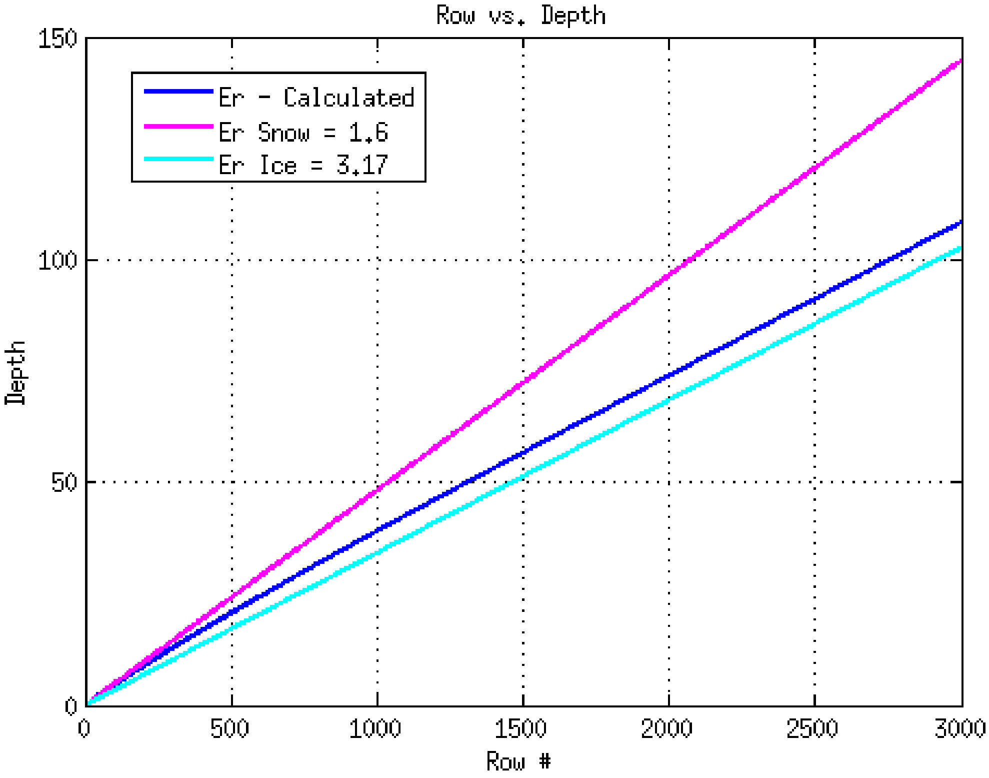

Figure 2.9: Depth-scale of different permittivities ϵ_r
Depth-scale r, Equation 2.3, is plotted using three different values for permittivity: 'Er - Calculated', calculated recursively by inserting composite density / permittivity from Figure 2.7 into Equation 2.3; 'Er - Snow' calculated using a constant permittivity of snow $\epsilon_r = 1.6$; 'Er - Ice' calculated using a constant permittivity of ice $\epsilon_r = 3.17$.

As shown in Figure 2.9, using a constant permittivity of snow or ice results in increasingly different depths as the radar signal penetrates down through the ice column. The differences in depth-scales reflect changes in density near the surface of the ice sheet. The x-axis represents radar travel time through the ice sheet, measured in "Rows" or vertical pixels (see also Figure 2.10 and Figure 2.8). Row zero represents the ice sheet surface. 'Er - Calculated' accounts for changes in snow/ice density and the corresponding impact on radar signal propagation through the ice sheet. Less dense snow permits the radar signal to travel more quickly down through the ice sheet, resulting in row 1500 representing a depth of approximately seventy meters. More dense ice impedes the speed of the radar signal, resulting in row 1500 representing a depth of approximately fifty meters. The calculated ϵ_r , using permittivity that varies with depth (Figure 2.7), is the most accurate depth-scale of the three and is used to calculate layer depth in this thesis 2.9. The derived depth-scale, ‘Er - Calculated’, is applied across the entire radar transect. Attaching this depth scale and GPS data to the radar horizons provides a physical location for the accumulation radar data. Figure 2.8 describes how radar data are connected to a physical location.

2.4.2 Horizon Tracing

In order to address the research questions set forth in Section 1.5, the visible reflections must be traced two-dimensionally across space and depth. The horizon tracing algorithm was a work-in-progress throughout this thesis work. Initial tracing algorithms were based on suggestions from Dorthe Dahl-Jensen and Susanne Buchardt. Originally, two different tracing techniques were developed to handle variations in slope, spacing, and amplitude in the horizons at different depths. Subsequent versions gradually strayed from the original method and the current version discussed here is capable of tracing horizons at all depths.

The horizon tracing algorithm operates as a function, with the user providing several variables and the function returning a data structure of the traced horizon. The horizon tracing algorithm uses a general trend line to trace the horizon’s position. The general trend line can be manually entered by clicking on the start and end point of the horizon. Existing lines can be entered as a general trend line (Figure 2.10).

Due to the similarity of adjacent horizons, the smoothed trace of the previous horizon is often used as the general trend line. A window centered on the general trend line is used to select the maximum voltage return value for each column. The vertical height of the search window can be adjusted to account for varying horizon thicknesses. However, adjusting the vertical window size may introduce a bias in the amplitude of a traced horizon. A small window (2 rows wide) restricts the trace to the range of the general trend, whereas a large window (9 rows) allows the trace to jump to maximum values of nearby horizons. After extensive trial and error, a window of 6 rows proved optimal and other window sizes were used only in extreme cases (wide dark horizons or closely space faint horizons). The returned data structure contains the position of the traced horizon in raw radar dimensions (row/column). The vertical row values must be converted to actual depths using known relationships about the speed of electromagnetic energy in snow and ice.

2.5 Ice Core Records

Ice cores contain multiple parameters related to climate history, particle deposition, and snow accumulation. Some of these parameters may also be represented in the radar record. The PRISM radar data collected between the GISP2 and GRIP deep ice cores fits Eisen et al. [2006] call for radar studies that connect deep-drilling locations. The ice cores can impose sound geophysical constraints on the age-depth scales of the radar imagery. These

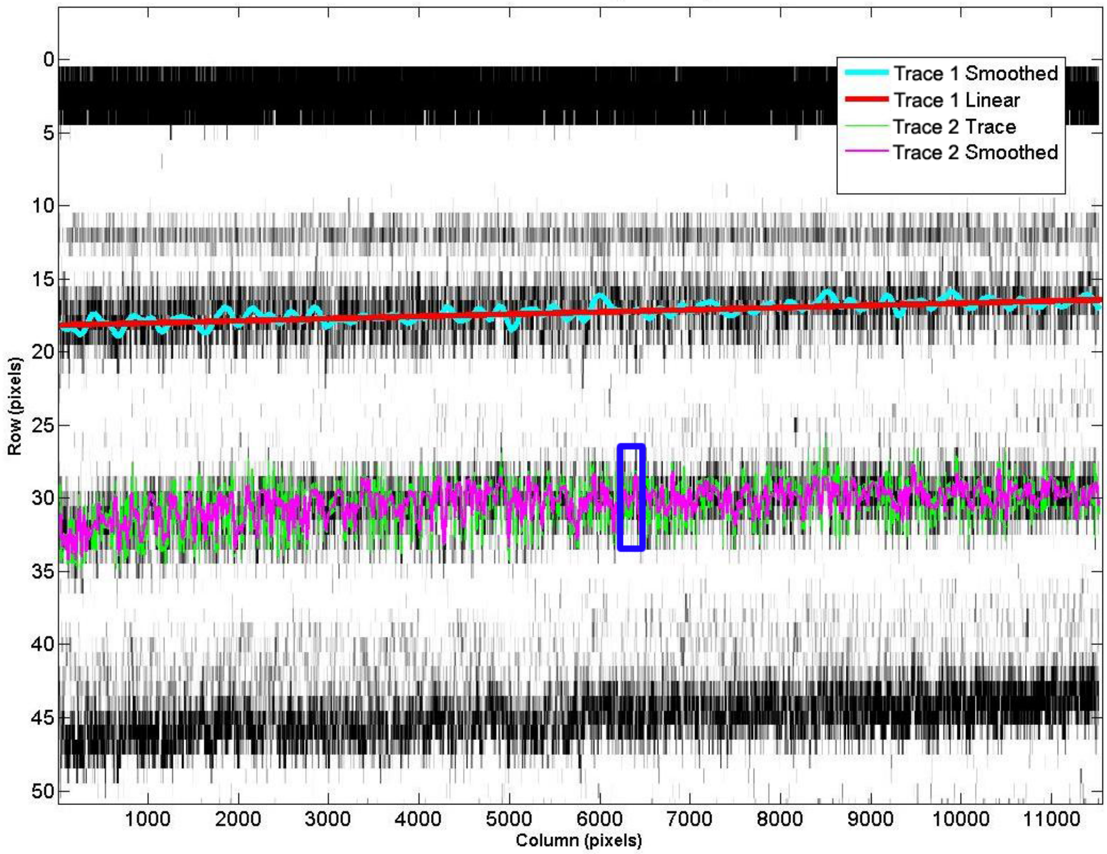

Figure 2.10: Traced horizon example
Traced horizons represent peak radar reflection values traced across the entire radar transect. Trace 1 Smoothed (cyan) is the mathematically smoothed trace of Trace 1. Trace 1 Linear (red), the linear fit of Trace 1 Smoothed, serves as a guide for tracing the next underlying horizon. Trace 1 Linear is shifted to overlay the next horizon and a 1 x 6 window (blue box) is vertically centered on the shifted Trace 1 Linear. Trace 2 Trace (green) results from selecting the maximum reflection values within the window. In this figure, the width of the window is exaggerated for visual clarity. The final trace for Trace 2 is represented by Trace 2 Smoothed (magenta).

constraints are independent of other dating methods, which are usually based on ice-sheet modeling or ice-core records like gas and isotope profiles [Eisen et al., 2006]. Indeed, if layers have been dated from their observed depths in an ice core, knowledge on the depth-age relationship can be invoked at locations far from the drill site by following the internal layers.

Two deep cores (GISP2 and GRIP) and several shallow cores (OSU and DRI Shallow cores) collected in the Summit region will serve as comparison records to the radar data (Table 2.1). The time span of the ice cores and the radar data do not match. The radar data begins in 2005, while the ice core records have starting dates of 2002, 1999, 1989, and 1987. The offset in time/depth of the ice core records are adjusted to 2005 values by use of a snow compaction model and known accumulation rates [Vinther, 2008a].

Table 2.1: The location, timespan, and mean accumulation rate of the fifteen ice cores used in this study (mapped in Figures 2.1 and 2.2).

Ice Core	Lat (N)	Lon (W)	Elev(m)	Time Span	Mean Annual Accum (cm/yr)	Source
GRIP	72.5873	37.6325	3230	1500–1989*	22.6	a
GISP2	72.5760	38.4649	3211	1500–1987*	24.2	b
Sandy	72.5500	38.3200	3208	1753–2003	22.4	c
Katie	72.5820	38.4765	3208	1934–2003	22.4	c
D4	71.4000	43.9000	2730	1738–2003	41.4	c
Summit99	72.5500	38.3250	3208	1538–1999	22.1	c
# 13	72.8864	39.1567	3167	1959–1987	21.1	d
# 15	72.9814	37.7042	3188	1959–1987	16.3	d
# 31	72.3486	40.2139	3115	1959–1987	26.2	d
# 37	72.6408	35.9444	3160	1959–1987	18.5	d
# 44	72.2939	37.9214	3215	1959–1987	22.7	d
# 51	71.9267	39.8353	3112	1959–1987	27.4	d
# 57	71.9206	35.9592	3090	1959–1987	21.4	d
# 73	71.6022	38.1414	3168	1959–1987	24.9	d
# 571	72.2119	35.6675	3087	1959–1987	18.5	d

*Span used for this study. Data source:

[a] GRIP, 1997a [b] GISP2, 1997a

[c] Banta *et al.* 2007 [d] Van der Veen *et al.* 2001

2.5.1 GISP2 and GRIP Deep Ice Cores

The accumulation radar data connects the GISP2 and GRIP deep ice cores. These cores were dated by identifying and counting annual layers using a number of physical and chemical parameters that included measurements based on visual stratigraphy, electrical conductivity method (ECM), laser-light scattering from dust (LLS), oxygen isotopic ratios of the ice ($\delta^{18}O$), major ion chemistry and the analysis of glass shards and ash from volcanic eruptions [Hammer, 1986; Johnsen et al., 1992; Meese et al., 1997]. Each of these parameters (with the exception of volcanics) exhibits a distinct seasonal signal (see Section 2.6). The definitive summer stratigraphic signal at both core sites occurs in the form of coarse-grained depth-hoar layers formed by summer insolation [Alley and Koci, 1990]. The relief of the snow in the region surrounding the GRIP and GISP2 sites is remarkably flat. Sastrugi (ridges formed on the snow surface by wind erosion and deposition) several centimeters in height may be produced by storms, but subsequent deposition, sublimation, and densification tend to level the surface [Meese et al., 1997].

Three separate accumulation records, GISP2 Visual (GISP2 V) and GISP2 Model (GISP2 M), and GISP2 b-core [GISP2, 1997b,g,a] will be used for comparison with the radar-derived accumulation rate. The upper 300 meters of the GISP2 V record was dated using stratigraphy, isotopes, ECM, volcanics, and some laser light scattering, with an estimated error of 1% for 1133 years [Meese et al., 1997]. The GISP2 M accumulation rate results from an ice-flow model constrained by temperature estimated from the GISP2 borehole, the GISP2 $\delta^{18}O$ record, and the Meese/Sowers depth-age scale [Cuffey and Clow, 1997]. The GISP2 M accumulation record assumes a 200 kilometer retreat of the ice sheet margin during deglaciation, which is cited as the most accurate of the model runs [Cuffey and Clow, 1997]. The GISP2 b-core accumulation rate is determined by applying the GISP2 b-core's depth vs. density profile to the GISP2 b-core age-depth scale [GISP2, 1997b]. The GISP2 V, GISP2 M, and GISP2 b accumulation records use the mid-point of the summer stratigraphic horizon as their definitive annual layer marker. Annual layers for the GRIP core were dated using visual stratigraphy, ECM, dust, nitrate and ammonium, which all give excellent annual layers. Annual accumulation values for the GRIP core represent winter to winter stratigraphic horizons [Vinther et al., 2006].

2.5.2 Ohio State University Summit Cluster Cores

Nine dated shallow cores (Figure 2.2) drilled in 1987 by Ohio State University [Van der Veen et al., 2001] are also compared to the radar data. The cores extend to a depth of 17 meters and span 41 years at their longest. The benefit of these shallow cores is their high degree of sampling. Density and delta oxygen-isotope-18 ($\delta^{18}O$) measurements were recorded every 10 centimeters for the first two meters and every five centimeters below two meters depth. The high resolution density data are used to create reflectivity coefficients for input into a synthetic radar model. The $\delta^{18}O$ profile and gross Beta-radioactivity profiles are used to establish accumulation rates which were then compared to ice cores [Bolzan and Strobel, 1994]. The high sampling interval and well preserved oxygen isotope ratio allow for the identification of both winter-to-winter and summer-to-summer layers. From these markers, winter to winter and summer to summer accumulation rates were determined. The accumulation rates provide a specific seasonal comparison to the temporally continuous radar data.

2.5.3 Desert Research Institute Cores (DRI)

The Desert Research Institute drilled four shallow cores in 2003 and 2004 near Summit, Greenland. Annual layer counting based on multiple glaciochemical parameters (primarily hydrogen peroxide, sea salt, and dust proxies) was used to date the ice cores [Banta and McConnell, 2007]. Three cores are located near the radar data and mean annual accumulation from these cores will be compared to radar-derived accumulation estimates. The DRI cores, spanning 1934 to 2002, fill the majority of the gap between the GRIP, GISP2, and OSU cores collected in the late 1980s and the radar data collected in 2005. In addition to comparing accumulation, peak values of black carbon, vanillic acid, and non-sea-salt sulfur, will be compared to layers with peak radar reflections in order to determine if these properties impact permittivity/conductivity, and therefore radar reflection.

2.6 Ice Core Properties relating to Radar

Ice cores provide a variety of variables that could possibly be represented in the radar data. To determine how well the radar data relates to various variables in ice cores, the radar data will be correlated with the following ice core variables:

2.6.1 Oxygen Isotope Ratios

The relationship between oxygen isotopes found in ocean water and water vapor can be used to track annual cycles. Evaporation and condensation are the two processes that most influence the ratio of heavy oxygen to light oxygen in the oceans. A NASA instructional website explains as follows:

> Water molecules containing light oxygen (Oxygen-16 isotope, ^{16}O) evaporate slightly more readily than water molecules containing heavy oxygen (Oxygen-18 isotope, ^{18}O). At the same time, water vapor molecules containing the heavy variety of oxygen condense more readily. The slightly greater mass of ^{18}O than ^{16}O results in differentiation of the isotopes in the Earth's atmosphere and hydrosphere. As air cools by rising into the atmosphere or moving toward the poles, moisture begins to condense and fall as precipitation. At first, the precipitation contains a higher ratio of water made of heavy oxygen, since those molecules condense more easily than water vapor containing light oxygen. The remaining moisture in the air becomes depleted of heavy oxygen as the air continues to move poleward into colder regions. As the moisture reaches the

> upper latitudes, the falling rain or snow is made up of more and more water molecules containing light oxygen [NASA, 2009].

In cold regions, such as Greenland and Antarctica, the primary factor that determines the ratio of $^{18}O/^{16}O$ is the difference between the condensation temperature at a given location, and the condensation temperature at the first stage of the precipitation process, that is, when water evaporated from the ocean. Thus, the ratio of $^{18}O/^{16}O$ will vary by the temperature when the snow was formed, allowing snow from winter and summer periods to be distinguished [Bamber and Payne, 2004].

The ratio between the concentrations of heavy and light oxygen isotopes is commonly expressed using the δ (delta) scale, which represents the relative difference between the ratio in the sample and that ratio in Stand Mean Ocean Water (SMOW) [Craig, 1961; Dansgaard, 1964; Dansgaard et al., 1973].

$$\delta^{18}O = \frac{\frac{^{18}O}{^{16}O}sample - \frac{^{18}O}{^{16}O}SMOW}{\frac{^{18}O}{^{16}O}SMOW} \tag{2.4}$$

Throughout the year, $\delta^{18}O$ varies with peaks (least negative values) identifying summer layers, and troughs (most negative values) representing snow deposited during the winter. This seasonal cycle is preserved in glacier firn and thus provides annual markers that distinguish individual accumulation years [Dansgaard et al., 1973; Bolzan and Strobel, 1994]. A five-year section of the seasonal $\delta^{18}O$ cycle from the OSU Summit Cluster shallow cores [Bolzan and Strobel, 1994] is presented in Figure 2.11. Using these individual accumulation years, an accumulation rate is derived from the ($\delta^{18}O$) record and can be compared to the radar layers.

2.6.2 Visual Stratigraphy

The visual stratigraphy is based on the simple observation that summer snow and winter snow look different. This difference in appearance arises from the physical reality that the properties of near-surface snow are affected by atmospheric conditions and radiative fluxes, which change seasonally. Summer layers are characterized by coarse-grained, low-density depth hoar, often alternating with higher-density, finer-grained accumulation including wind slabs [Alley et al., 1997]. An accumulation rate derived from this seasonal tracking of visual layers can be compared to the radar-derived accumulation rate.

2.6.3 Annual Layer Thickness

Annual layer thickness is the vertical distance measure between visual differences in summer and winter snow accumulation. Layer thickness data reveals compaction of snow to firn and eventually firn to ice. Annual layer thicknesses observed in ice cores decrease as a function of depth. Assuming the radar layers represent annual accumulation, it should be expected

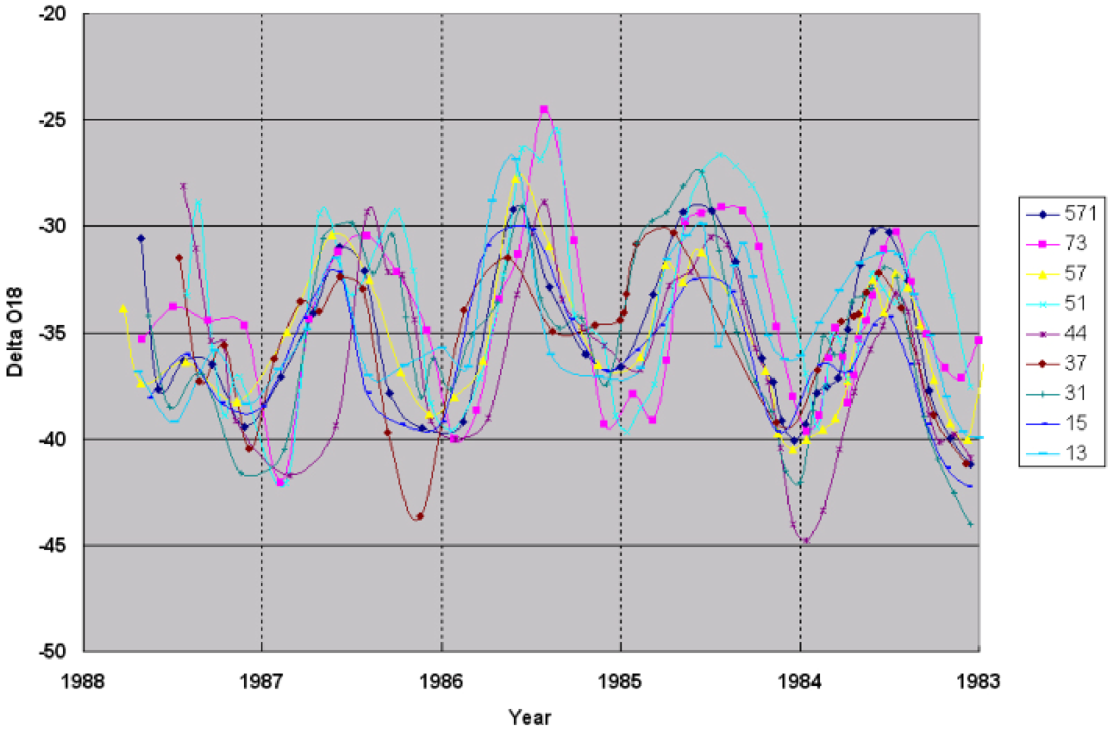

Figure 2.11: Seasonal variations of Delta ^{18}O from the OSU shallow cores Plotted delta $\delta^{18}O$ values from the 9 OSU shallow cores [Bolzan and Strobel, 1994] provide an example of a seasonally varying ice core property used to accurately date ice cores. Note the summer maxima peak in the middle of the year and winter minimum trough near the start of the calendar year, similar to the radar reflection returns in Figure 2.5.

that radar layer thickness decreases at a similar rate as observed in the ice cores. This record, combined with snow/ice density values, is used to compute annual accumulation rate in Section 3.3.

2.6.4 Electrical Conductivity Measurement (ECM)

Electrical Conductivity Measurement (ECM) is considered to be a measure of the acidity of the ice. ECM is ideally suited for investigation of short-duration phenomena (volcanic eruptions) that influence the acid/base balance of the ice [Taylor et al., 1992]. The direct-current electrical conductivity of glacial ice depends on its acidity, and can also indicate changes in climate, as ice formed in cold, dusty periods has a high concentration of alkaline dust, which significantly reduces the conductivity compared to warmer, less dusty periods [Taylor et al., 1993]. Comparison of the dated ECM peaks to strong reflecting radar layers and comparison of the depths of major volcanic horizons visible in the ECM data layers to depth of peak radar reflections will help accurately date and constrain the radar layer data.

2.6.5 Gross Beta-Radioactivity

Atmospheric testing of thermonuclear weapons in the 1950s and early 1960s resulted in increased atmospheric levels of ^{90}Sr and ^{137}Cs and corresponding elevated β-radioactivity levels in the snow deposited at that time. Dated minima and maxima from active testing periods and testing moratoriums constrain annual layers by providing an absolute time horizons used for determining accumulation rates [Bolzan and Strobel, 1994; Van der Veen et al., 2001]. Excellent radar layer clarity down through depths containing elevated β-radioactivity levels allows for the examination of radioactivity's impact on radar reflection intensity.

2.7 Radar Surveys and Ice Cores

The radar data map the upper 150m of the ice sheet along transects between the GISP2 and GRIP ice cores. Within the 150 meter depth, ice cores have been dated confidently with estimated time error of 1% [Meese et al., 1997]. The cores serve as benchmarks at each end of the radar transects, providing detailed records of annual accumulation. Variations in snow accumulation, snow deposition patterns, and local ice flow conditions may cause the depth of a layer in the GISP2 core to differ from the layer's depth in the GRIP core. However, good dating allows comparison of the depth of an annual accumulation layer found at GRIP to be directly compared to the depth that this same layer is found at in the GISP2 core. A layer's depth in one core is not expected to predict the depth that same layer may be found in another core. Local variations in accumulation rate, wind scouring, and snow compaction are several factors that can influence layer depth between the GRIP and GISP2 cores. Assuming similar trends in snow compaction over time, the difference between the depth of one layer in the GRIP core compared to that same layer in the GISP2 core should be relative. This comparison, called depth-difference, can then be compared to the radar depths of layers at GRIP and GISP2. A radar depth-difference is assembled by comparing the depth of the radar layers at GRIP to the depth of these same radar layers at GISP2. Because the radar data was collected in 2005 and the ice cores were collected in the early 1990s, the actual depths of the radar and the ice cores will be different. If the radar layers do indeed represent accumulation layers, the depth-difference profile of these layers should resemble the depth-difference of the GRIP/GISP2 cores.

Previous radar studies with more limited vertical resolution were only able to detect prominent volcanic layers reflecting the radar's signal [Fujita and Mae, 1994; Fujita et al., 1999; Hempel et al., 2000]. Major volcanic layers found in ice cores represent known dates and depth horizons. The depth of these horizons in ice cores, identified with Electrical Conductivity Measurements (ECM), can be compared to the depth of peak reflections in the radar data [Kanagaratnam et al., 2004]. Because the cores were collected years prior to the radar data, the ice core depths must be adjusted to account for accumulation and compaction of snow between the time the core was drilled and the time the radar data was collected. Combining a snow compaction model provided by Vinther (2008) and local accumulation rates at the site of each ice core, the adjusted depth of a known volcanic horizon can be compared to the depth of peak reflection horizons in the radar.

Comparing peak radar reflection horizons and volcanic horizons in the ice cores is not the only option for dating the layers. The high vertical resolution of the radar used in this study allows layers to be counted from the surface down to depths of suspected volcanic horizons. For example, a signal from the 1912 Katmai volcanic eruption appears in accumulation years 1912–1913 at a depth of 35 meters in the GRIP ice core. Therefore, in addition to finding a peak reflection value around a depth of 35 meters in the radar profile, one would also expect to count ∼93 layers, representing 93 years of accumulation, between the 1912–1913 volcanic layers and the 2005 surface. This approach of counting layers and comparing ice core depths will be implemented on other properties with peak values (black carbon, vanillic acid, non-sea-salt sulfur, and gross-beta radioactivity). Comparing ice core and radar data in this manner begins to address the question whether radar layers represent annual accumulation and also links peak radar reflections to extremes in physical properties.

If the radar data does represent annual accumulation, it would be expected that the signal of the radar compares favorably to ice core properties that exhibit an annual signal (oxygen isotopes, density, dust, hydrogen peroxide, sea salt). Unfortunately, the ice core data with an annual signal used in this thesis often do not have sufficient resolution to compare radar and ice core properties on an annual basis. For example, ECM data represent the annual average, thus seasonal fluctuations in acidity are not visible. Instead, the depth/position/age of minima and maxima in ice core properties such as ECM are compared to the depth/position/age of peak radar reflections, as described above. But, assuming that the radar horizons result from an annually occurring physical property, thus marking annual boundaries, these horizons can be used to calculate an annual thickness of snow accumulation and an accumulation rate that can be compared to an ice core derived accumulation rate.

Pearson's product-moment correlation coefficient (Pearson's r) is applied to annual ice core accumulation rates and the radar accumulation rate determined from reflection horizons. (Pearson's r) is the most commonly used measure of correlation for interval or ratio variables [Burt and Barber, 1996]. Pearson's r expresses the relative strength of the linear relationship between two variables. Using Pearson's r to compare the accumulation rate derived from radar horizons and the ice core accumulation rates provides a general starting point for investigating what physical properties may cause layer reflections. Each ice core record will be correlated with the radar data to determine which, if any, of the ice cores best matches the radar data. Composite ice core signals will be compared to the mean radar signals, as well as moving correlations over different spatial scales of the radar data. The correlations only provide an indication of a linear relationship, and thus primarily serve to constrain which ice cores merit a more detailed similarity assessment.

Visually identifying similar features by comparing the relative position of high and low values may be possible for identifying peaks in radar reflection and acidity peaks in the ice core data. However, if the patterns are not perfectly sequenced, high values may be compared with low values, and similar patterns based on relative location will not be apparent in an assessment of similarity. A sub-annual layer mistakenly identified as an annual layer, or an annual layer not counted as such, may appear as only a minor temporal offset at that location, but may result in the entire rest of the records no longer being in phase and resulting in erroneous correlations.

Ice core and radar derived accumulation rates are compared using Pearson's r to assess their similarity. Accumulation rate sequences are intentionally shifted/offset when applying Pearson's r to identify missing or miscounted accumulation years. The various individual physical parameters used to compute ice core accumulation rates will be compared to the traced radar layers to determine if these layers represent annual horizons. These comparisons seek to reinforce the finding that annual accumulation can be derived from radar layers. Ice core accumulation rates that match well with radar accumulation rates can then be used for direct comparison of the physical properties used to define the ice core accumulation rate.

Chapter 3

Results

3.1 Traced Radar Horizons

Using the tracing algorithm described in Section 2.4, 352 consecutive radar horizons are counted and traced to a depth of 110 meters below the ice sheet surface. Figure 3.1 depicts the upper 10 meters of radar data and the resulting trace of alternating horizons (every second horizon is displayed for visual clarity). The radar data are displayed relative to the July 2005 surface. The actual surface elevation changes along the transect (see Figure 2.3), but for the sake of viewing the horizons as a stratified medium, the varying surface elevation is treated as "depth = 0" and all horizons are described relative to this zero surface. Near-surface horizons mimic the topography and accumulation pattern of the surface location. The long-term (previous 9,000 years) accumulation rate in the Summit region is slightly higher at GISP2 (0.245 m/yr) than GRIP (0.230 m/yr) [Dahl-Jensen et al., 1993; Meese et al., 1994].This slight accumulation difference along the GISP2/GRIP radar transect is evident even within the first 10 meters of the surface (Figure 3.1).

GISP2's slightly higher accumulation rate compared to GRIP results in more snow and thicker, more deeply buried horizons. Because horizons are displayed relative to a zero-depth surface (meaning the surface is treated as 0 m depth), thinner layers slope down from the right (east) side of Figure 3.1 near GRIP to slightly thicker layers on left (west) side of the figure near GISP2. The slope in accumulation becomes increasingly evident with depth. Sloping horizons at a depth of 100 to 110 meters display this difference in accumulation rate (Figure 3.2). At 100 meters depth, layers have thinned to more than half their thickness at the surface and reflection voltage values have weakened. Figure 3.2 depicts the deepest horizon traced for this thesis. Subsequent horizons are visible to a depth of 150 meters, but increased noise and fading reflection values prevent horizons at depths of 110 to 150 meters from being confidently traced.

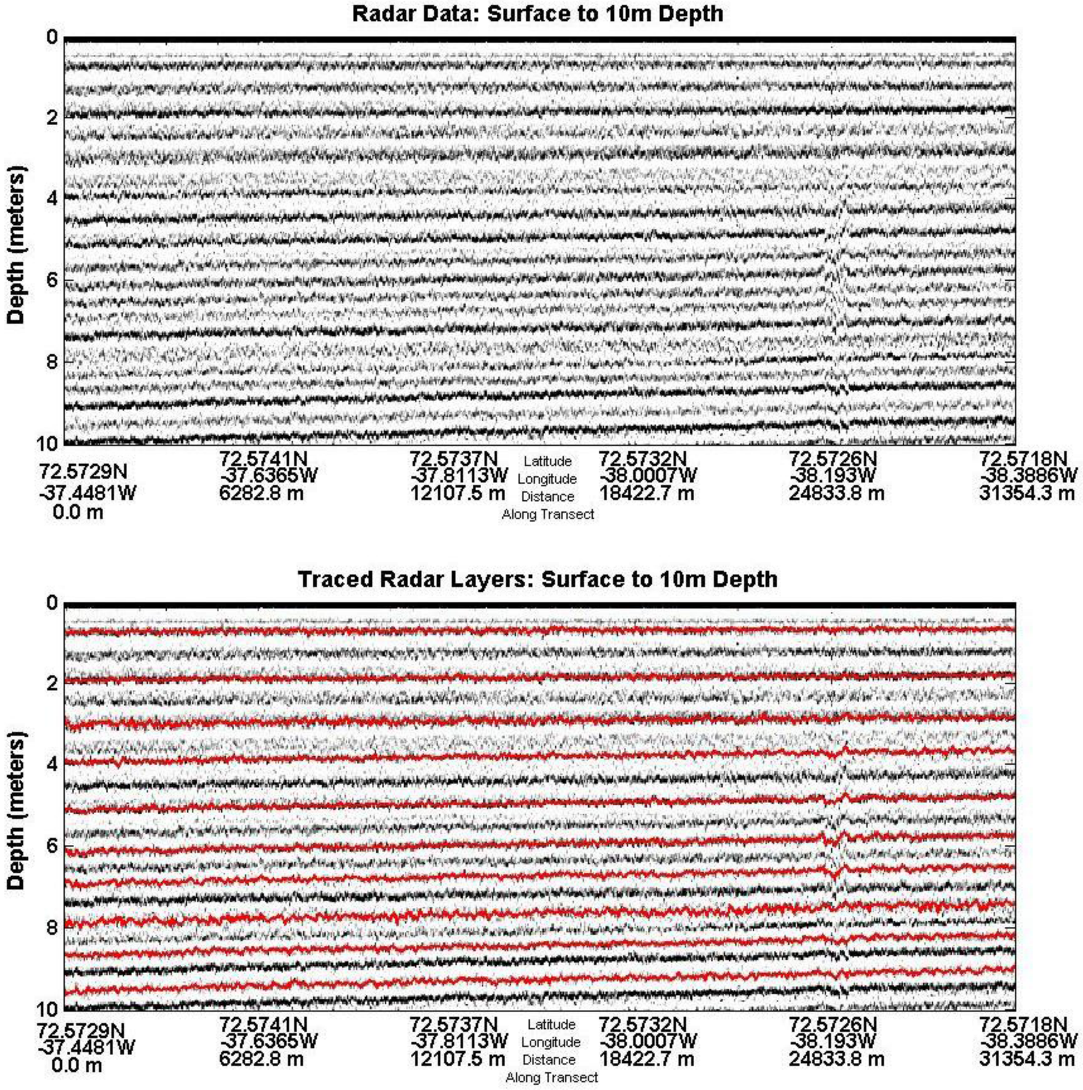

Figure 3.1: Radar data and traced layers, surface to 10m depth
Radar data connecting GISP2/GRIP, from surface down to 10m depth is shown in the upper plot. The ice sheet surface is treated as 0 meters depth; all radar horizons are plotted relative to this zero-depth surface. Note a slight negative (downward) slope of layers from GRIP to GISP2 (right to left). Small differences in accumulation rates between the cores, GISP2 0.245 m/yr, GRIP 0.230 m/yr [Dahl-Jensen et al., 1993; Meese et al., 1994], account for the sloping layers. The lower plot displays an example of traced horizons; every second traced horizon is shown for visual clarity.

3.2 Do Radar Layers Represent Accumulation?

3.2.1 Comparison using Depth Difference

Differences in depth of annual accumulation layers result from slightly different accumulation rates, deposition patterns, and ice flow conditions at the site of the core. The more

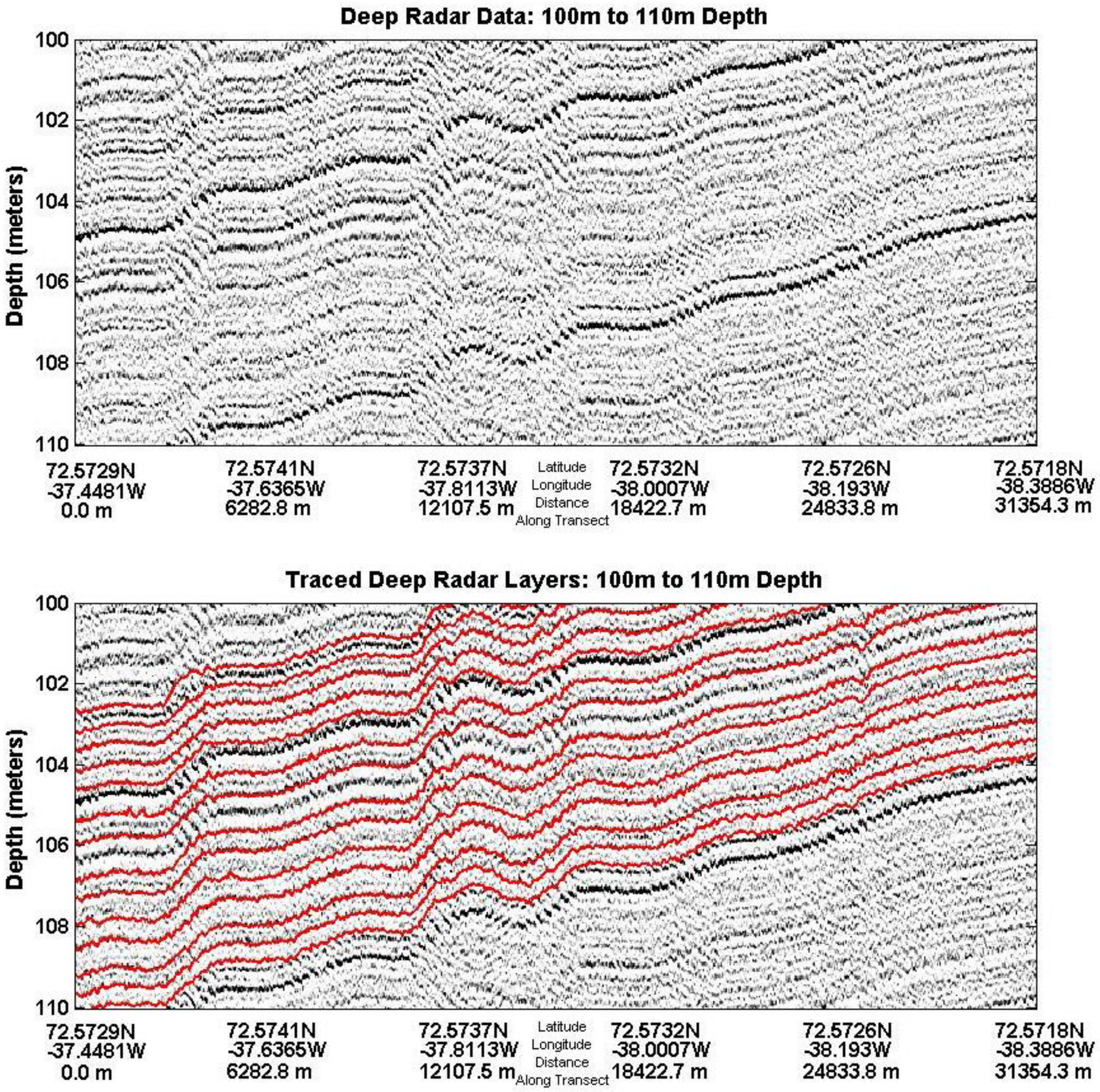

Figure 3.2: Radar data and traced horizons, 100 to 110 m depth
Radar horizons at 100 to 110 meters below the surface are shown in the upper plot. Note the accumulation gradient along the transect illustrating the increase in accumulation along from GRIP to GISP2 (right to left). Plotting the depth of radar layers relative to a zero-depth surface helps to visualize areas with high accumulation rates, as layers are buried deeper. At this depth, layers have thinned to more than half their thickness at the surface (see Figure 3.4 for changes in layer thickness vs. depth). The lower plot displays alternating traced horizons from 100 to 110 meters depth; every second horizon is displayed for visual clarity. The dark, intensely reflecting horizon below the deepest red traced horizon at 110 meters represents the last horizon traced for this thesis.

accumulation or deposition an area receives, the faster and deeper a layer is buried. Known depths of accumulation layers in the GRIP and GISP2 ice cores were compared. The long-term accumulation rate is slightly higher at GISP2 (0.245 m/yr) than GRIP (0.230 m/yr)

[Dahl-Jensen et al., 1993; Meese et al., 1994] and this accumulation gradient can be seen in the previously discussed Figure 3.2. These differences gradually accumulate over time and this "depth-difference", defined as the difference between the depth of an annual layer in the GISP2 core and that same layer's depth in the GRIP core, increases linearly with depth (Figure 3.3). Figure 3.3 shows the difference between a layer's GISP2 depth and that same layer's GRIP depth, relative to the GRIP depth of the layer.

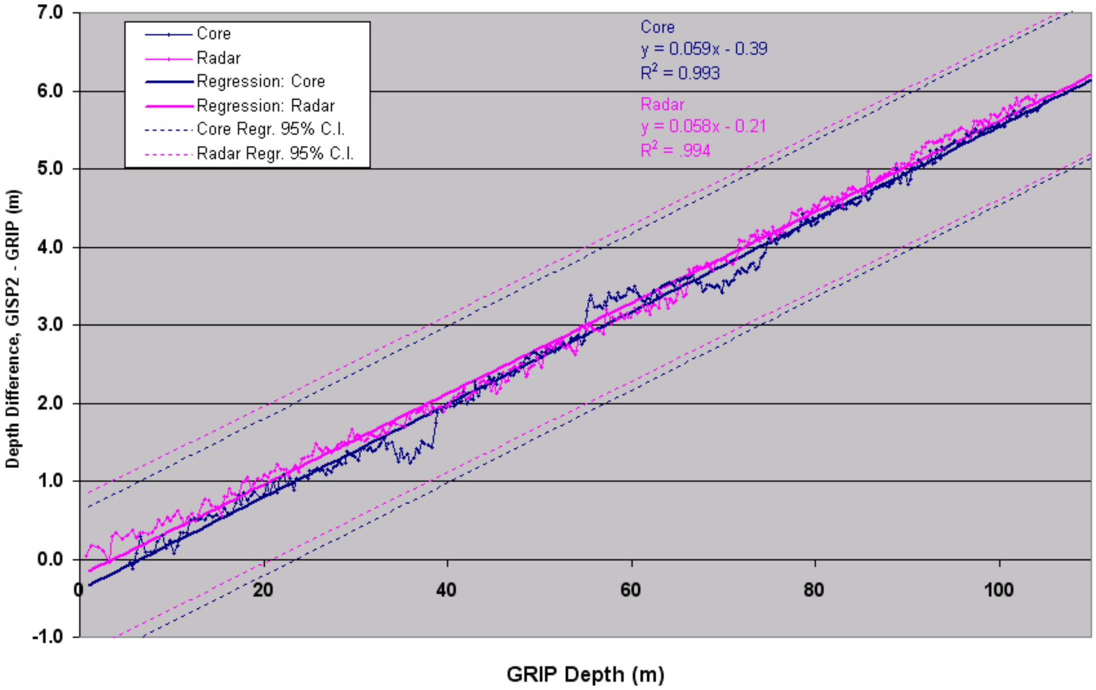

Figure 3.3: Depth-difference of layers in GISP2 and GRIP
The depth-difference recorded from the ice cores is plotted alongside the depth-difference from the radar horizons. The linear fits for the ice core and radar data are discussed in the text. The dashed lines illustrate 95% confidence intervals for a depth-difference value at a given depth. The two linear regression lines do not differ statistically, indicating that the radar horizons may represent annual accumulation.

The ice core depth-difference values and the radar depth-difference values are very similar. For example, the ice core depth-difference is ∼2.7 meters for the 150th layer from the surface, while the radar's 150th horizon from the surface has a depth-difference of ∼2.5 m. The depth-differences remain similar down through the ice column, where the ice core depth-difference for the 300th layer equals ∼5 m and the radar's 300th horizon depth-difference equaling ∼5.1 m. The ice core depth-difference is fit by the line $y = 0.059x - 0.39$, with $R^2 = 0.993$. The radar horizon's depth-difference between the GISP2 and GRIP sites are fit by the line $y = 0.058x - 0.21$, with $R^2 = 0.994$. Measured depths for both the GRIP and GISP2 ice cores do not begin until 5.5 meters depth, which explains the negative y-intercept of the linear fits. The difference in slope between the linear fits of the radar and ice cores is statistically insignificant with a 95% confidence interval. This suggests that the radar layers are closely correlated to events that create a reflective surface at some stage of accumulation and that are then buried. It is highly likely that such regular events are associated with accumulation layer properties, but it could also be caused by other potential surface deposition events.

3.2.2 Layer Thickness

Annual layer thickness is the vertical distance measured between successive winter-to-winter or summer-to-summer accumulation horizons. The radar horizon's darkest reflections were traced across the radar transect, thus the radar layer thickness represents a winter-to-winter accumulation layer (the thickness from one dark horizon extending through a white "summer" band of accumulation down to the next dark "winter" horizon). Layer thickness data reveals compaction of snow to firn and eventually firn to ice. Annual layer thicknesses observed in ice cores decrease as a function of depth. Assuming the radar layers represent annual accumulation, it should be expected that radar layer thickness decreases at a similar rate as observed in the ice cores. Layer thicknesses from the GISP2 and GRIP ice cores are compared to the radar layer thicknesses near the GISP2 and GRIP sites (Figure 3.4). Radar and ice core layer thicknesses decrease with depth, as near-surface snow accumulation compacts and gradually becomes ice. Variations in density and accumulation rates result in "thickness vs. depth" profiles that are not identical, but do follow a general trend similar to what is observed in the depth vs. density profile of Figure 2.7. The general trend of gradually decreasing layer thickness is observed in both the ice core and radar layers (Figure 3.4).

A logarithmic fit is used to assess ice core and radar thicknesses. Logarithmic fit lines plotted in Figure 3.4 have similar equations:

$$\begin{aligned}
\text{GISP2 Ice Core: } y &= -0.074Ln(x) + 0.60 \qquad (3.1)\\
\text{GISP2 Radar: } y &= -0.073Ln(x) + 0.59 \qquad (3.2)\\
\text{GRIP Core: } y &= -0.072Ln(x) + 0.57 \qquad (3.3)\\
\text{GRIP Radar: } y &= -0.070Ln(x) + 0.56 \qquad (3.4)
\end{aligned}$$

This similarity between radar layer thickness and ice core annual layer thickness supports the hypothesis that the radar layers represent annual accumulation. Layer thickness, combined with snow/ice density values, is used to compute annual accumulation rate in Section 3.3.

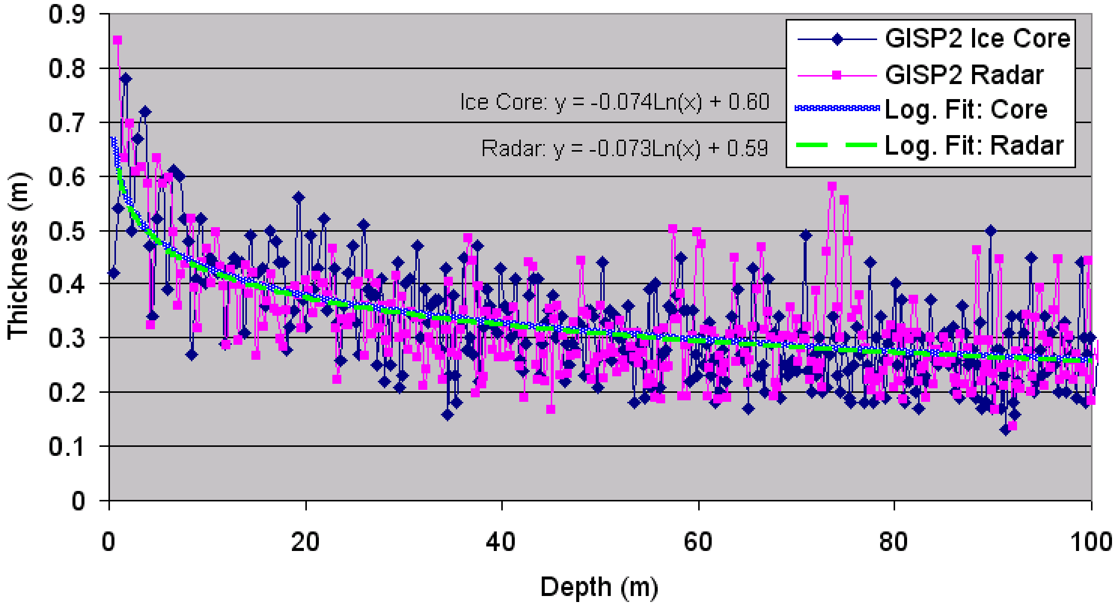

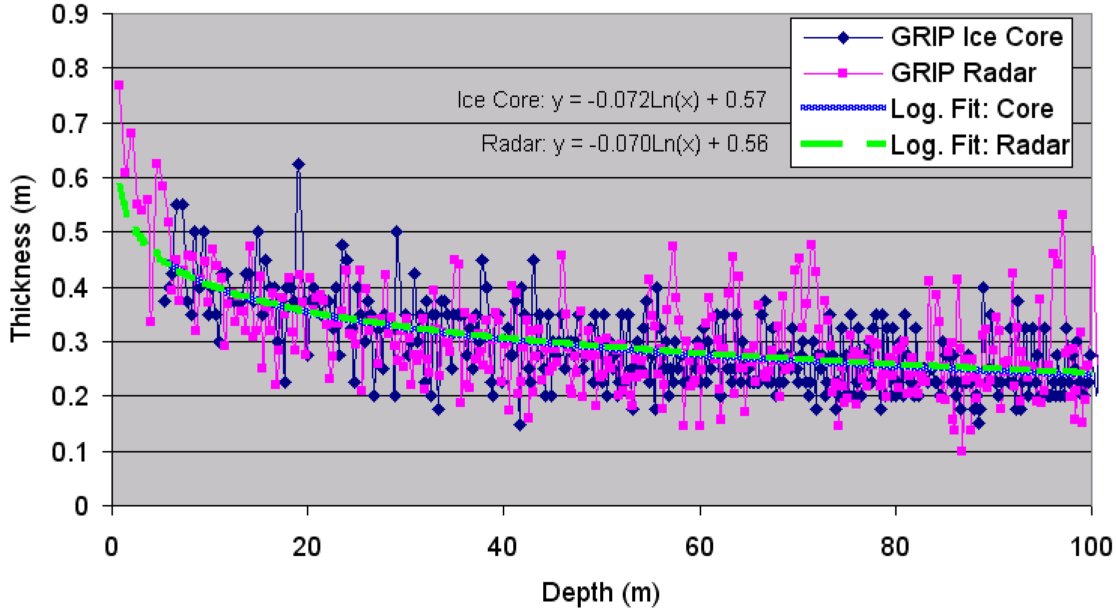

Figure 3.4: Ice core and radar layer thicknesses
GISP2 ice core layer thickness is compared to radar layer thickness near GISP2 (upper plot). The same comparison is made for GRIP ice core layer thickness and radar layer thickness near the GRIP (lower plot). Aside from the first ten meters, where changing thickness and a lack of data impact the fit, logarithmic fits of the radar and ice core data are nearly identical (see Equations 3.1 3.2 3.3 3.4)

3.2.3 Volcanic horizons and Intense Radar Reflections

Major volcanic events aid in the dating of ice cores and have also been proven as a source of internal reflections in ice sheets [Taylor et al., 1992; Hempel et al., 2000]. Prominent, intensely reflected radar horizons were investigated to see if they correlated with any major volcanic events found in the GISP2 and GRIP ice cores. The high resolution of the radar data allows for layers to be clearly counted from the ice sheet surface down to 110 meters depth. A suspected volcanic horizon in the radar data is cross-checked with the position of the volcanic event in the deep ice cores (Table 3.1).

The 1912 Katmai, Alaska, eruption is evident in both the GISP2 and GRIP cores for the accumulations years of 1912 and 1913. The ice core depth of this volcanic event at the time of extraction was 32.8 meters and 30.5 meters respectively, for GISP2 and GRIP [Taylor et al., 1992, 1997; Vinther, 2008b]. Adjusting for accumulation and snow compaction between the time of ice core extraction and radar data collection, the 1912 Katmai eruption would be expected to occur at 37.8 meters depth in the GISP2 core and 35.9 meters in the GRIP core [Vinther, 2008a]. Indeed, a strikingly prominent radar layer appears at 36.6 meters depth and 35.2 meters depth near GISP2 and GRIP respectively. The radar surface represents summer 2005, which means that 93 layers should be observed between the surface and the 1912 Katmai eruption event. The prominent layer in the radar data is the 96th layer counted from the surface. If the prominent layer does represent the 1912 Katmai eruption, then somewhere between this layer and the surface three sub-annual layers were traced and counted as accumulation layers.

Table 3.1: Comparing ice core volcanic layers and intense radar reflections For ice cores, "Depth" represents the depth of the volcanic layer at the time of extraction (1989) shifted to 2005 depths using known accumulation values and a firn compaction calculation [Vinther, 2008a]. The "Layer" column is the numbered/counted visible layers starting with the year 2005 equaling the zero surface (thus 2004 = Layer 1, 2003 = Layer 2, etc.). "OFFSET" Layers represents extra (+) or missing (-) layers counted between suspected volcanic horizons. "OFFSET" depth is the difference in depth between the intense reflection layers observed visually in the radar data and the major volcanic layers observed in the ice cores. Note that the "YEAR" column refers to the year the layer is identified within the GRIP ice core. Three volcanic layers are identified at different years within the GISP2 ECM record. Differing years are denoted with * and include Katmai, 1913; Laki, 1783; Jan Mayen, 1730. These offsets between the two cores may partially explain the offset between the radar and ice cores.

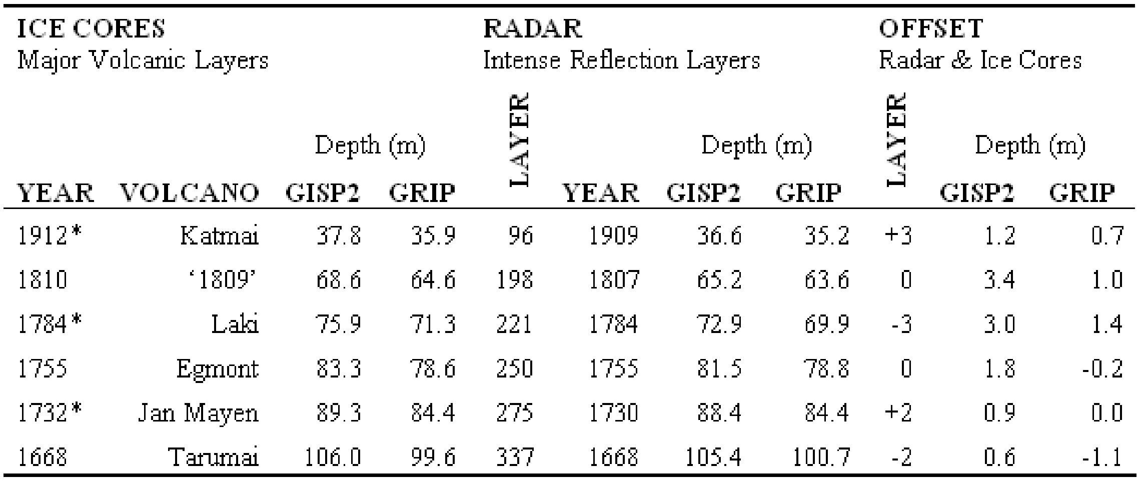

ICE CORES Major Volcanic Layers				**RADAR** Intense Reflection Layers				**OFFSET** Radar & Ice Cores		
		Depth (m)				Depth (m)			Depth (m)	
YEAR	**VOLCANO**	**GISP2**	**GRIP**	**LAYER**	**YEAR**	**GISP2**	**GRIP**	**LAYER**	**GISP2**	**GRIP**
1912*	Katmai	37.8	35.9	96	1909	36.6	35.2	+3	1.2	0.7
1810	'1809'	68.6	64.6	198	1807	65.2	63.6	0	3.4	1.0
1784*	Laki	75.9	71.3	221	1784	72.9	69.9	-3	3.0	1.4
1755	Egmont	83.3	78.6	250	1755	81.5	78.8	0	1.8	-0.2
1732*	Jan Mayen	89.3	84.4	275	1730	88.4	84.4	+2	0.9	0.0
1668	Tarumai	106.0	99.6	337	1668	105.4	100.7	-2	0.6	-1.1

An eruption titled "1809 Eruption" appears in the GISP2 and GRIP ice core record the following year of 1810 [Zielinski, 1995; Clausen et al., 1997]. The depth of this eruption, adjusted to 2005 based on accumulation and compaction, is 68.6 meters in the GISP2 core and 64.6 meters in the GRIP core. A corresponding prominent layer is present in the radar record at a depth of 65.2 and 63.6 meters. The strong reflection at this depth is the 198th layer counted, corresponding to the year 1807, a difference of 3 years compared to the 1809 Eruption that is visible in the year 1810. Hence, at this depth, three layers have been counted as annual that may instead represent sub-annual layers.

The 1783 Laki, Iceland, volcanic eruption is visible in both deep ice cores during the year 1784 [Zielinski, 1995; Clausen et al., 1997]. Laki is found at a 2005 adjusted depth of 75.9 in the GISP2 core and 71.3 meters in the GRIP core. The 221st layer traced from the surface, representing the year 1784, has a dark/prominent reflection and appears in the radar data at a depth of 72.9 meters near GISP2 and 69.9 near GRIP. Thus, at this depth, the layers that were previous excluded and/or miscounted a previous depths are now synchronized, with a dark layer representing the 1784 year and occurring at a depth near this volcanic layer's location in the ice cores.

A spike in acidity (possibly the Egmont volcanic eruption in New Zealand) occurs in year 1755 at a 2005 adjusted depth of 83.3 meters and 78.6 meters depth in the GISP2 and GRIP electrical conductivity measurements (ECM) [GISP2, 1997e; GRIP, 1997b; Price et al., 1999; Vinther, 2008a,b]. Observed radar layer 250, representing the year 1755, is a strong/dark reflecting layer and occurs at 81.5 meters depth near GISP2 and 78.2 meters near GRIP (Figure 3.5).

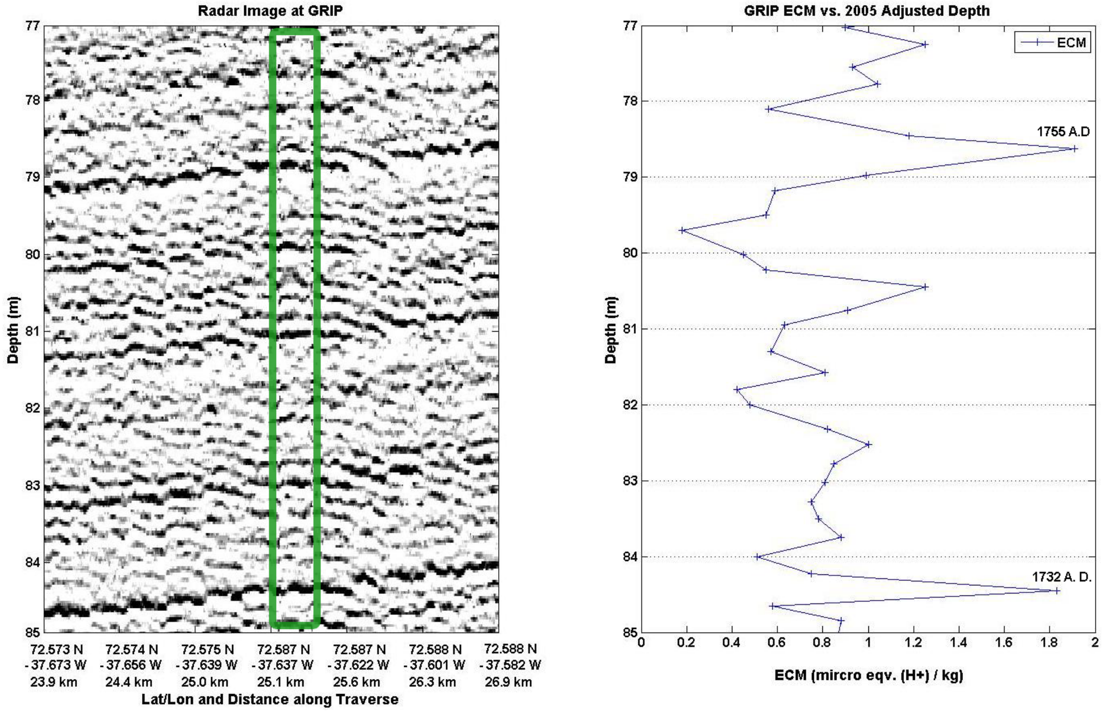

Figure 3.5: GRIP ECM and radar depth of volcanic layers 1755 and 1732 A.D. The depth of GRIP electrical conductivity measurements (ECM) are compared to radar depths of strong reflection horizons. The box in the left plot represents the approximate location of the GRIP core. The right plot displays peak ECM values representing volcanic layers dated 1755 A.D. and 1732 A.D. are compared to prominent radar layers at similar depths. The dark layer at ~78.5 meters depth is the 250th layer counted from the surface and matches the ECM date of 1755 A.D. The dark layer at ~84.5 meters depth is the 275th layer counted from the surface, representing 1730 A.D compared to the 1732 A.D. peak from the ECM data. Table 3.1 summarizes prominent layers found in radar data and peaks in GRIP ECM.

Another prominent spike in ECM data, possibly connected to the Jan Mayen eruption (Norway) occurs in year 1732 in both the GRIP and GISP2 ice cores [Zielinski, 1995; GISP2, 1997c; GRIP, 1997b]. A dark layer in the radar data appears 275 layers from the surface, representing the radar year 1730. If this dark radar layer does represent the 1732 volcanic event, and assuming the 1755 marker is correct, then two extra radar layers were counted as annual between 1755 and 1732. The 2005 adjusted depth of the 1732 year is at 89.3 and 84.4 meters in GISP2 and GRIP [Vinther, 2008b]. A dark prominent layer appears at a depth of 88.4 meters near GISP2 and 84.4 near GRIP (layer near GRIP visible in Figure 3.5).

The GISP2/GRIP ice core records reveal a 1668 volcanic layer likely connected to the Tarumai Eruption in Japan [Zielinski, 1995; Vinther, 2008a,b]. The adjusted 2005 depths for the 1668 volcanic horizon occur at 106.0 meters near GISP2 and 99.6 meters near GRIP. An intense reflection horizon 337 layers below the surface, corresponding to a radar year of 1668, is evident in the radar data at a depth of 105.4 meters near GISP2 and 100.7 meters near GRIP.

Six major volcanic horizons found in the upper 110 meters of the ice sheet compare favorably, in both time and depth, with intense reflecting layers in the radar data (Table 3.1). From the surface down to what appears to be the 1912 Katmai eruption, three extra layers are counted (or three sub-annual layers were counted as annual). Excluding the three extra layers counted and assuming the prominent reflection is the 1912 Katmai eruption, exactly 102 layers are counted between this 1912 layer and the next dark reflection horizon, named “1809 Eruption” (preserved in the ice core record in 1810). Thus between dark horizons at 1912 and 1810, no extra layers are counted. The overall offset between horizons traced and dated volcanic horizons remains at three extra layers, found between the 2005 surface and the 1912 Katmai horizon. Between the assumed “1809 Eruption” horizon and the assumed 1784 Laki eruption horizon, only 23 layers are counted over the 26 year time span (recall ‘1809 Eruption’ is found in the core at year 1810). Thus between 1810 horizon and 1784 Laki horizon, three layers are missing and/or too weak to be deemed reflection horizons. Exactly twenty-nine layers are counted between 1784 Laki horizon and the next prominent reflection horizon, believed to be the 1755 Egmont eruption. Two extra layers are counted between the 1755 Egmont horizon and the 1732 Jan Mayen eruption. Between the dark 1732 Jan Mayen horizon to the 1668 Tarumai eruption, two fewer layers are counted.

The overall offset between the layers counted and the dated horizons in the ice cores can be misleading. From the 2005 surface to the suspected 1784 Laki horizon, exactly 221 horizons are counted for the 221 year time span. 377 horizons are counted from the suspected 1668 Tarumai to the 2005 surface. Thus for both the 1784 Laki and 1668 Tarumai horizons, the “offset” for both horizons is zero in Table 3.1. Despite this appearance of a one-to-one radar horizon to dated ice core layer, the position of missing and extra layers is roughly known by using prominent volcanic markers, as discussed above. The three missing layers between 1810 and 1784 is offset the three extra layers counted between the 2005 surface and 1912. Specific depths of the radar profile (2005–1912 and 1810–1784) can be more closely examined to identify extra (possibly sub-annual) layers counted or faint horizons missed.

“Missing” and “extra” layers are observed in other detailed studies of near-surface accumulation. Possible explanations for “missing” or “extra” layers include large storm events, unseasonably warm periods, and, though less likely, also variations in the chemical or physical properties that cause radar reflections [Hawley et al., 2008]. Hawley et al. [2008], count four extra annual layers in the upper 30 m of firn near Summit, similar to the three extra layers observed in the upper 35 m of this thesis. “Extra” layers resulting from large storm events may disappear (from compaction) at deeper depths, thus explaining the improvement in agreement between counted radar layers and years for the 1912-1810 period. Hawley et al. [2008], also observe improved agreement between various accumulation rates at greater depths.

The agreement between dated volcanic horizons and counted radar layers, and similar depths of these dated ice core layers and radar layers, enforce the argument that the radar layers are annual. Additionally, this comparison strengthens the argument proposed in previous radar studies [Fujita et al., 1999; Hempel et al., 2000; Matsuoka et al., 2002] that changes in acidity related to volcanic activity can impact the intensity of a layer’s reflection.

In addition to visually inspecting radar layers for dark/intense layers, the radar’s reflection intensity can be plotted versus time (Figure 3.6). Plotting radar reflection intensity helps pinpoint maxima in reflection power that may otherwise be obscured when viewing layers with a grey-scale color range. As shown in Figure 3.5, peaks in ECM result in darker layers, but often these darker layers are not proportionally “intense” when viewed as radar reflections. A large peak in ECM may only result in a moderate peak in radar reflection intensity. Peak radar reflections match inconsistently with ECM and acidity peaks. A 1909 radar reflection peak and the 1912 Katmai volcanic eruption, and an intense radar reflection of a layer corresponding to 1668 A.D. and a 1668 Tarumi volcanic eruption, are examples of ECM and radar reflection peaks coinciding. Alternatively, large peaks in ECM in 1810 and 1783 do not result in proportional spikes in radar reflection intensity.

The absence of a major reflection peak at the site of a major ECM peak does not mean that ECM is insignificant in radar reflections, but rather that changes in dielectric constant are complicated and may result from a variety of factors such as ECM, dust, microparticle concentration, vanillic acid, and black carbon (e.g. Figure 3.6, where the strong peak in radar reflection around 1863 appears tied to peaks in black carbon and vanillic acid rather than fluctuations in ECM).

Available GRIP and GISP2 ice core data for dust and microparticles is not continuous for the entire length of the core, with data only spanning particularly dusty periods, and no possibility for examining annual fluctuations in dust. Figure 3.6 plots peaks in radar reflection intensity alongside peaks in dust and microparticles. Two separate measurements for dust in GISP2 were examined: microparticles and laser-light scattering. Periods of high dust and microparticle concentrations correspond inconsistently with peaks in radar reflection intensity. An 1863 radar reflection peak matches peaks in both the LLS dust and microparticle/dust record, whereas dust peaks around 1810, 1745, and 1690 do not result in proportionally intense radar reflections (Figure 3.6).

Volcanic layers linked to intense radar reflections raise the question of what other ice

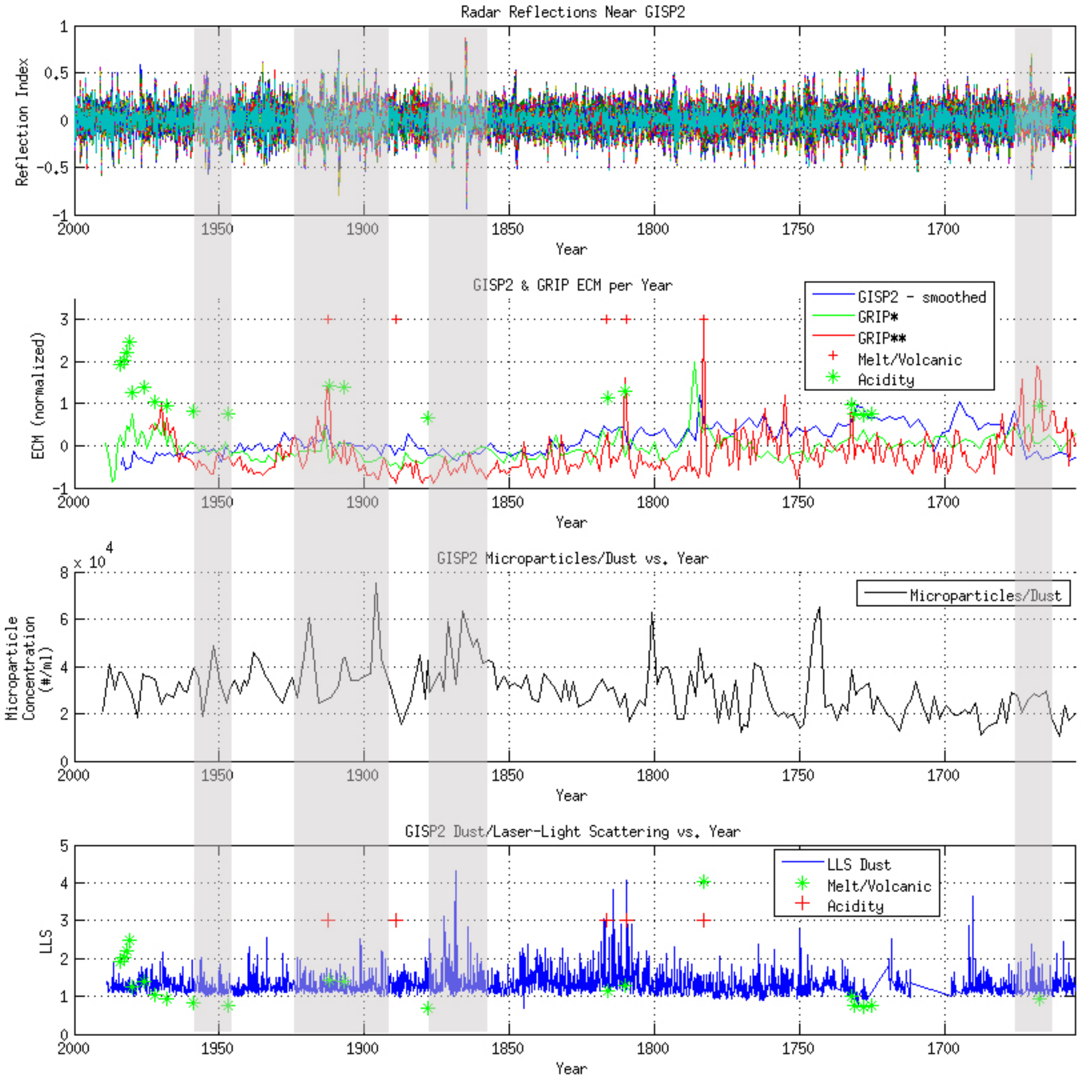

Figure 3.6: Radar reflections compared to ice core physical properties
Radar reflection intensity near GISP2 is compared on a common time scale to physical properties found in ice cores. Electrical Conductivity Measurements (ECM) from GISP2 and GRIP, major melt layers, volcanic horizons, peaks above background levels in acidity, and two separate measurements for dust (microparticles and laser-light scattering) are plotted [GISP2, 1997e,b,d; GRIP, 1997b; Vinther, 2008b]. Vertical bars mark peaks in radar reflection and physical properties.

core properties might cause changes in ice's dielectric constant and therefore impact radar reflections. The Desert Research Institute's D4 shallow core (Figure 2.1) was analyzed for non-typical physical properties. Using shallow core data provided by Banta and McConnell [2007], the physical properties of black carbon, vanillic acid, and non-sea-salt sulfur were compared to peak radar reflections (Figure 3.7). The provided shallow core data contained peak markers but sampling resolution did not allow for comparison of annual layers. Intense reflections in the radar profile occasionally match with peaks in black carbon and vanillic acid (in particular, peaks near 1909, 1868, 1863, and 1794), but overall agreement between peak radar reflections and the physical property peaks of black carbon, vanillic acid, and non-sea-salt sulfur are inconsistent and inconclusive.

Physical properties of materials in ice cores often coincide with intense reflecting radar horizons, but this correspondence is not one-to-one. This is not surprising given the multitude of factors that can influence permittivity of snow and ice (density, acidity, crystal orientation) [Robin et al., 1969; Harrison, 1973; Paren and Robin, 1975]. Overall, depth-difference and known volcanic horizons provide the strongest argument for the radar layers representing annual accumulation boundaries, with rare cases where annual boundaries are missed or specific sub-annual events represented as separate layers in rare occasions. Based on the counted layers, the depth/position of intensely reflecting layers where volcanic layers would be expected, and based on the comparisons of accumulation rates of ice cores and radar data, support the argument that the radar layers represent annual accumulation.

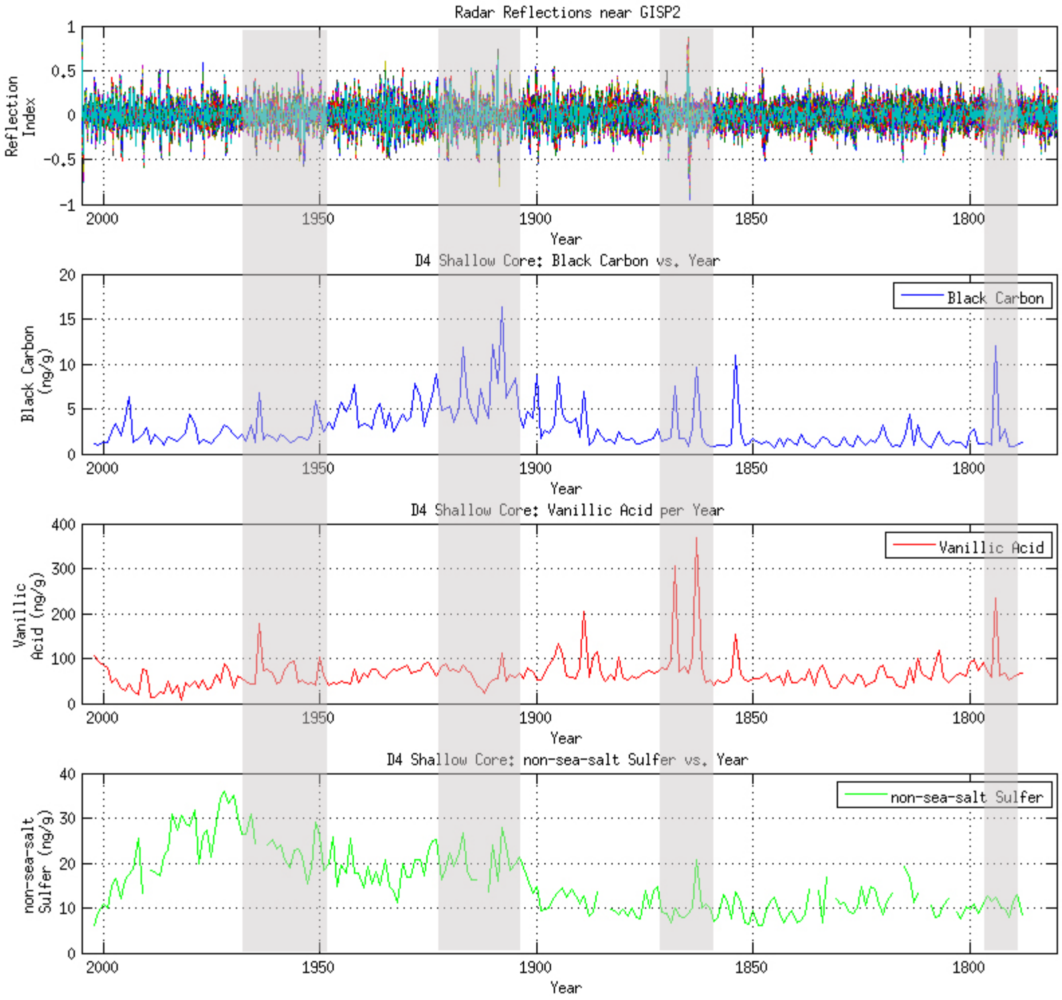

Figure 3.7: Black carbon, vanillic acid, and non-sea-salt sulfer and radar reflections Radar reflection intensity is plotted versus age for 150 radar traces (top). The traces cover ~405 meters near the GISP2 core site and were selected for their relative proximity to Desert Research Institute's D4 core (Figure 2.1). Black carbon and radar reflections both exhibits peaks in 1909, 1868, 1863, and 1794. Coinciding vanillic acid and radar reflection peaks occur at 1868, 1883, and 1794. Vertical bars mark peaks in radar reflection and physical properties.

3.2.4 Temperature and Reflection Horizons

Despite seasonal mean temperatures well below freezing (see Section 2.1), strong variations in autumn and winter temperatures may produce secondary maxima in temperature proxy data from snow and ice stable isotope profiles in the summit area [Shuman et al., 2001]. The vapor flux accompanying these secondary warming periods may cause depth-hoar formation and crystal densification [Alley et al., 1997]. Assuming that a secondary warming period will impact snow density and depth-hoar formation, then it is possible that warming may cause faint multiple reflection horizons within a single annual accumulation layer, thus resulting in extra layers counted (see "Offset", Table 3.1). Hawley et al. [2008] cite warm periods as a potential cause of additional horizons appearing between successive annual layers.

3.3 Accumulation Rate from Radar Layers

An accumulation rate can be obtained from two consecutive layer boundaries and this accumulation value can be tracked spatially and temporally. Tracked layer thickness and density data are used to compute water equivalent accumulation of the snow/ice layers, which can then be directly compared to ice core accumulation values (Figure 3.8 documents the following described steps in calculating the radar-derived accumulation rate).

The traced position of a layer, measured in rows (radar time) is converted to a physical depth using the radar's speed through snow and ice (determined by permittivity, which is based on density). Using the traced radar layers, the vertical distance between two consecutive layers give the layer's thickness. This layer thickness represents snow/ice thickness and must be converted to a water equivalent thickness for comparison to ice core accumulation rates. Using the layer's midpoint depth, an average density for the layer is determined. The water equivalent accumulations rate is obtained from Equation 3.5 using density and thickness estimates from the radar. This process is applied to all 352 layers traced and for every radar pixel column along the transect, resulting in an average accumulation rate across the entire radar transect from AD 2004 to AD 1653 (Figure 3.9) which will be compared to ice core accumulation rates in Section 4.1. The radar-derived accumulation rate (A) is described by modifying Kanagaratnam's (2002) equation:

$$A = \Delta r \frac{\rho_{layer}}{\rho_{water}} \tag{3.5}$$

where Δr is the thickness/distance between two traced layers ($r_{layer2} - r_{layer1}$), ρ_{layer} is the average density between the two layers and ρ_{water} is the density of water [Kanagaratnam, 2002]. Errors in this accumulation rate, or measurement uncertainty ϵ, arise from uncertainty in the radar's travel time to a target (target's depth) and the uncertainty in specifying the timing (age) of summer horizons used to construct accumulation rates [Spikes et al., 2004].

The travel time to a target relates to determining the depth of a reflection horizon. As discussed in Section 2.4.1, and displayed in Figure 3.8, the travel-time, or wave speed, of the signal is dependent on snow's dielectric constant, or permittivity ϵ_r, which is dependent on density. Because density values were compiled from various ice core profiles, and thus spatially extrapolated along the entire radar transect, small errors may arise. Eisen et al. [2008] describe the density-depth and therefore wave speed as very homogeneous for large undisturbed regions of the Antarctic plateau, which is similar to the Summit region of the

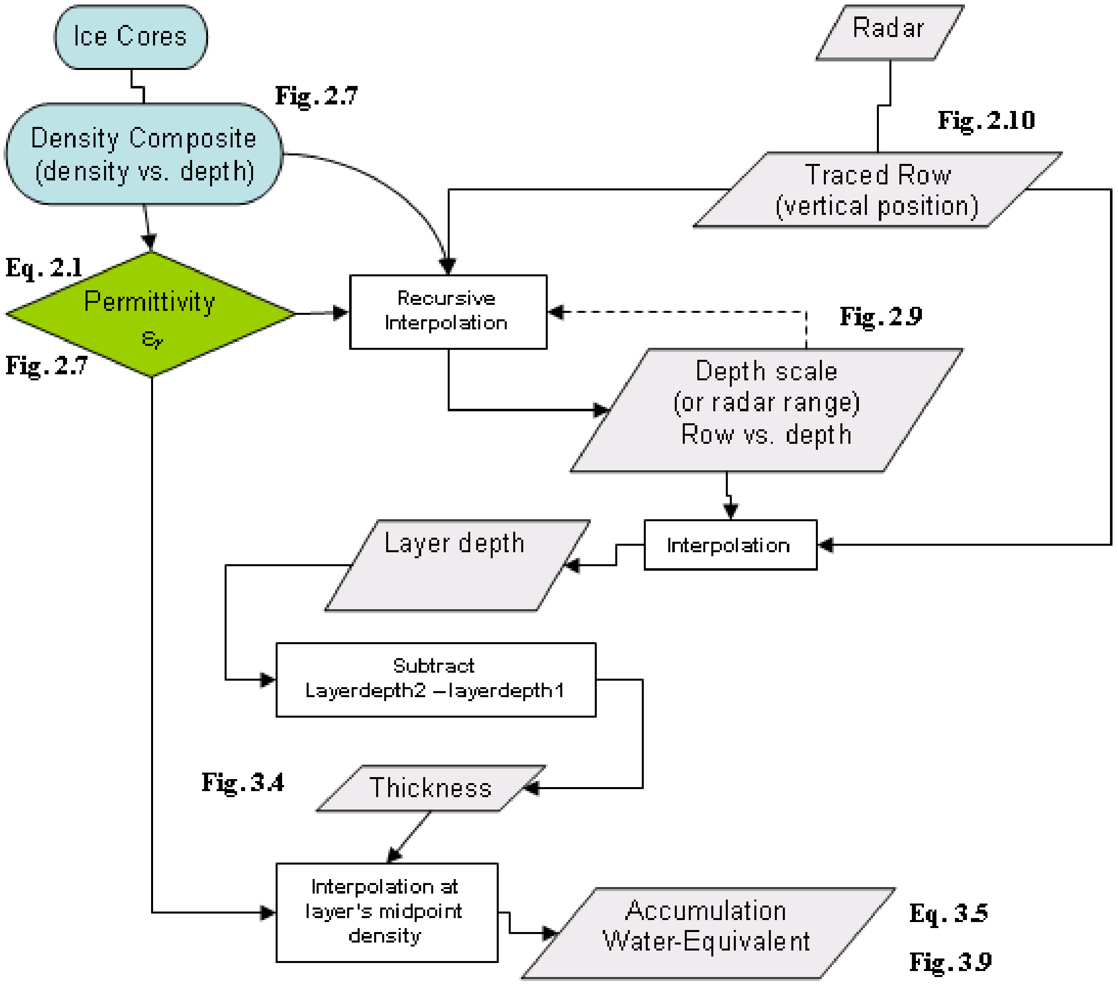

Figure 3.8: Calculating radar-derived accumulation rate flowchart
Previous figures and equations, presented as a flowchart, depict the steps necessary in calculating a radar-derived accumulation rate. Note permittivity's role at multiple stages of the radar accumulation rate calculation. The known row position of a traced layer is converted to a depth using the composite density profile from the ice cores and the calculated permittivity profile. The depth of consecutive layers is then used to determine the thickness of a layer. This snow/ice thickness is then converted to a water equivalent thickness using Equation 3.5.

Greenland Ice Sheet. By using the composite density profile described in Section 2.4.1., Figure 2.7, small-scale variations in density (from ice lenses or wind crusts) are averaged out. Thus large errors due to changes in density are not expected when calculating depth or wave speed. For this thesis, uncertainty of the radar travel time relates to radar-range, r (Equation 2.3). Kanagaratnam (2002) computes the uncertainty in the range, σ_r, which is related to the uncertainty in dielectric contant, σ_ϵ. The uncertainty in the dielectric constant is related to the uncertainty in the density, σ_ρ, and is given by Kanagaratnam [2002] as 5% resulting in an uncertainty of 0.01 m/yr water equivalent.

The other error in accumulation rate stems from uncertainty in specifying the timing of summer horizons used to construct accumulation rates. Eisen et al. [2008] state

> Uncertainties in the age estimate of a reflector are caused by the initial uncertainty of the original age-depth scale (snow pit, firn, or ice core) and the transfer of the age information for, e.g., a core to the reflector.

As discussed in Section 2.5.1, the uncertainty in age of deep ice cores is 1% [Meese et al., 1997]. For the interior of the Greenland Ice Sheet, Van der Veen and Bolzan [1999] find the standard deviation of the timing between two consecutive years to be 1.4 months [Van der Veen and Bolzan, 1999]. Van der Veen and Bolzan [1999] calculate the standard deviation from measurement error as 0.03 m water equivalent per year. Thus the total uncertainty in accumulation rate σ_A is ± 0.04 m/yr water equivalent and applies to the accumulation rates calculated by the radar (Figure 3.9).

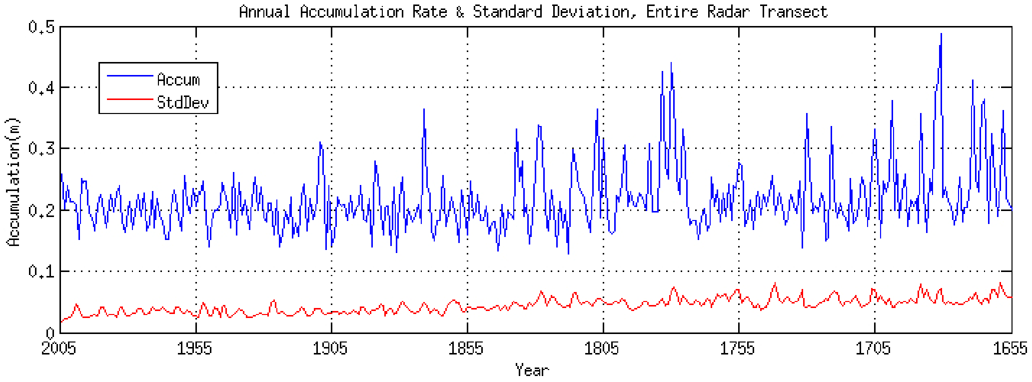

Figure 3.9: Radar derived accumulation rate and standard deviation
Radar derived accumulation rate and standard deviation of accumulation, averaged across the entire radar transect, spanning 2004 to 1653. Accumulation increases further back in time and average accumulation over this time period is 0.217 m/yr. Standard deviation of accumulation rate averages 0.044 m/yr from 2004 to 1653.

Chapter 4

Analysis and Interpretation

4.1 Comparing Accumulation Rates: Ice Core and Radar

Comparing radar reflection layers to ice cores helped confirm the hypothesis that the radar layers represent annual accumulation (Section 3.2). This hypothesis can be further tested by directly comparing accumulation rates from the ice cores to accumulation rates derived from the radar. An outcome of similarity, combined with previously discussed depth/acidity comparisons and Pearson's r correlations, would provide strong evidence that the radar layers represent annual horizons.

Ice core accumulation rates represent accumulation at a single point on the ice sheet. It is therefore not surprising that ice core accumulation rates vary even amongst cores drilled within close proximity to each other. Fluctuations in accumulation are seen in all ice core records. The physical and chemical properties that cause radar reflection horizons may varying in their timing from one year to the next [Anklin et al., 1998; Hawley et al., 2008]. Short-term fluctuations in snowfall due to climate variability and small-scale spatial differences in the amount of snow deposited are two sources of noise in records of ice core accumulation rate [Van der Veen and Bolzan, 1999]. Variability in accumulation is seen in the range of ice core accumulation rates from the Summit region cores (Figure 4.1).

Additionally, the radar-derived accumulation rate falls within the range of ice core accumulation rates and appears to coincide with the year to year trends seen in the ice core accumulation rates from 2000 to 1940 (Figure 4.1).

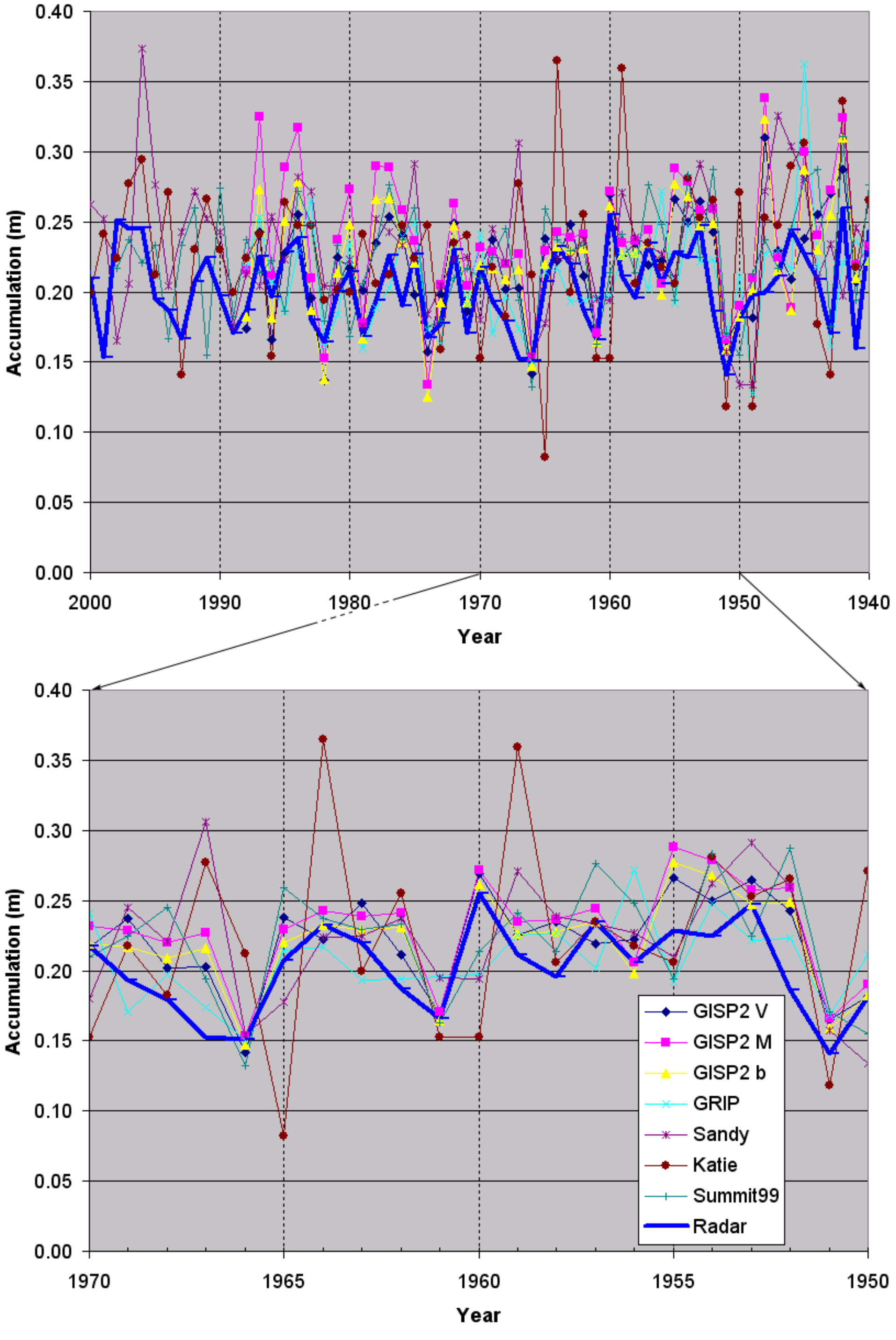

Figure 4.1: Ice core and radar accumulation records
Upper graph: radar and ice core accumulation records from 2000–1940. The lower graph: accumulation rates from 1970–1950. Radar derived accumulation falls within the range of the Summit ice cores.

The visual similarity is tested using Pearson's r correlation; ice core and the radar accumulation rate across the entire transect (Figure 3.9) are compared over their common time periods (Table 4.1). Ice core to ice core correlations values are relatively low. Aside from correlations between the GISP2 records ($r = 0.85$, $r = 0.89$, $r = 0.98$), core-to-core correlations range from $r = 0.17$ to $r = 0.47$. Radar-to-core accumulation rates generally have stronger correlations values, ranging from $r = 0.24$ to 0.63.

Table 4.1: Pearsons r Correlation Matrix: Ice core and radar accumulation rates Accumulation rates of the different ice core records are correlated against each other and the radar accumulation rate. Even ice cores within close spatial proximity exhibit fairly low correlation rates. The radar derived accumulation rates have higher correlation values than core-to-core comparisons, except for the three GISP2 accumulation records (see 2.5 for description of ice core records). The 'Radar' accumulation rate is plotted in Figure 3.9. (*Sandy, Katie: 2002–1934 *Summit99: 1999–1934 *GRIP & GISP2: 1988–1934)

Pearson Correlation Coefficient: Accumulation, Present* to 1934							
Core	Radar	Sandy	Katie	Summit 99	GRIP	GISP2 M	GISP2 V
Radar	1	-	-	-	-	-	-
Sandy	0.24	1	-	-	-	-	-
Katie	0.35	0.41	1	-	-	-	-
GRIP	0.38	0.41	0.30	0.28	1	-	-
GISP2 M	0.61	0.32	0.23	0.17	0.36	1	-
GISP2 V	0.60	0.30	0.20	0.45	0.30	0.85	1
GISP2 b	0.63	0.33	0.25	0.47	0.35	0.98	0.89

Correlation between the radar and ice core accumulation rates supports the hypothesis that the traced radar horizons represent annual accumulation. The relatively low correlation between ice cores indicates that further examination of the ice core accumulation rates is necessary to determine their suitability for comparison to the radar accumulation rate. The two records with the strongest correlation for the 2005–1934 period, GISP2 V and GISP2 M ($r = 0.98$), are examined over a longer period (1988 to 1850) to determine the reliability of correlating ice core accumulation rates over longer periods of time.

Plotted together, the GISP2 V and GISP2 M accumulation rates are similar in trend and magnitude, as expected (Figure 4.2). Despite this similarity in actual accumulation, a moderate difference in accumulation between the two records being correlated can disrupt the correlation comparison. Thus, low correlation values may not necessarily indicate that two accumulation records tell similar accumulation histories, but instead may indicate that the two records fall out of phase. Examining moving correlations of accumulation rate helps determine the time periods that two records correlate and the periods in which records are out of phase.

Five and thirty year moving correlations of accumulation from the two records are plotted in Figure 4.2.

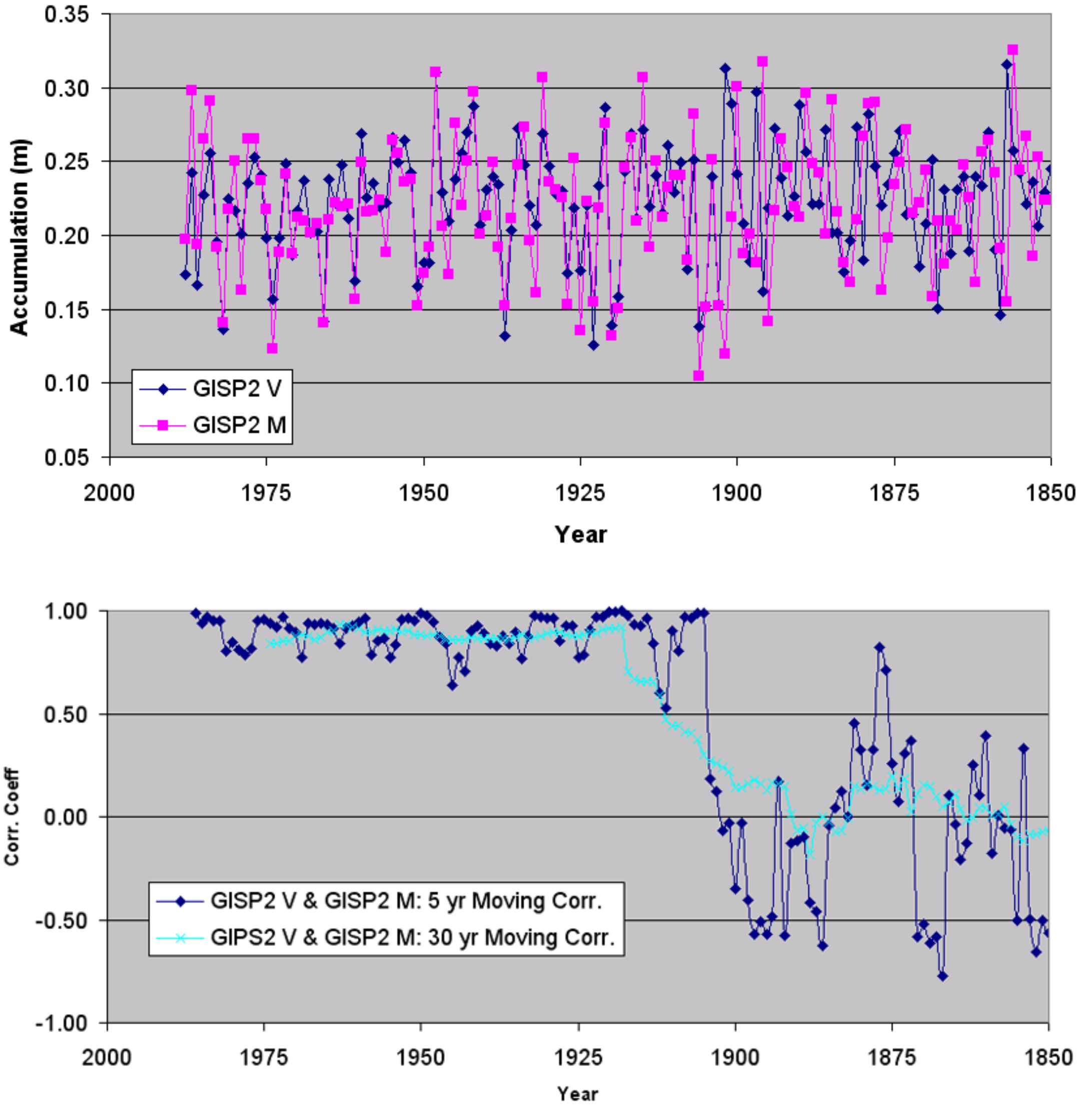

Figure 4.2: GISP2 V and GISP2 M: Accumulation rate and moving correlations Two individual accumulation records (GISP2 V and GISP2 M) derived from GISP2 are plotted on the upper chart. The lower chart presents moving Pearson's r correlations of the GISP2 V and GISP2 M accumulation records. Five and thirty year moving correlations of accumulation from the two records are plotted.

The five year moving correlation value for the year 1950 compares the GISP2 V and GISP M accumulation rates over a five year window spanning 1952 to 1948. The thirty year moving correlation for 1950 represents the GISP2 V and GISP M accumulation rates over a thirty year window spanning 1964 to 1935. The two records exhibit strong correlation until around 1910 when the accumulation records begin to become uncorrelated (lower). Despite the drop in correlation after 1910, the actual accumulation rates (upper) remain remarkably similar extending back to 1850. This inconsistency must be kept in mind when considering correlations between ice core and radar accumulation rates. The two GISP2 records appear to fall out of phase around 1900 A.D. This possible shift is examined by comparing accumulation rates over averaging intervals of five and thirty years (Figure 4.2). For example, the five year moving correlation value for the year 1950 represents the correlation between the GISP2 V and GISP M accumulation rates from 1952 to 1948. The thirty year moving correlation for 1950 represents the GISP2 V and GISP M accumulation rates over a thirty year window spanning 1964 to 1935. The records fall out of phase around 1904 and drift in and out of phase until after 1850. Year to year inspection of accumulation values show the records remain out of phase by only one year, with the overall trend of the two records nearly identical. Five year and thirty year sections of poorly correlating accumulation rates do not necessarily indicate that two accumulation rates are dissimilar. This apparent discrepancy will be considered when correlating ice core and radar accumulation rates. The GISP2 records' increasing offset in correlation extending beyond 1850 A.D., combined with unusually high radar-derived accumulation rates further back in time (Figure 3.9), indicate that correlations between ice core and radar accumulation rates may not be reliable prior to 1850 A.D.

The high correlation between the radar and ice core accumulation rates (Table 4.1) is further explored by extending the time interval compared. Previous correlations from Table 4.1 are extended back to 1900 and 1850 (Figure 4.3).

As indicated by the GISP2 comparisons, correlation values decrease as the length of the compared records increases. When the time span compared increases by 35 years (from present–1934 to present–1900), correlation between radar and cores decreases by an average of ∼22% (about 0.65%/year) for the Summit99 and GISP2 cores. The Desert Research Institute's (DRI) Summit99 core also decreases by 22% for the 1934 to 1900 increase. From 2002 to 1850, correlation decreases by an average of ∼53% for the GISP2 cores (about 0.35%/year) and 47% for the Summit99 core (about 0.31%/year) (Figure 4.3). Despite this decrease, the correlation between these five cores and the radar accumulation back to 1850 averages $r = 0.28$, which is close to or better than the core-to-core correlations over a shorter time period (Table 4.1). The DRI's Sandy core is the exception, as correlation improves when the length of comparison is extended from 2002–1934 to 2002–1900. The Sandy core exhibits the poorest correlation with radar accumulation of all seven cores, thus the improvement in correlation from 0.24 to 0.29 is considered insignificant. The DRI's Katie core only extends back to 1934 and is excluded from extended timescale correlations.

The Ohio State Summit Cluster shallow cores have shorter temporal coverage than the DRI cores, but are valuable for comparison of recent accumulation rates. The nine Summit Cluster cores have both winter-to-winter and summer-to-summer accumulation rates, ranging from twenty-three to forty-one years of accumulation available for comparison to the radar accumulation rates. The winter-to-winter and summer-to-summer accumulation

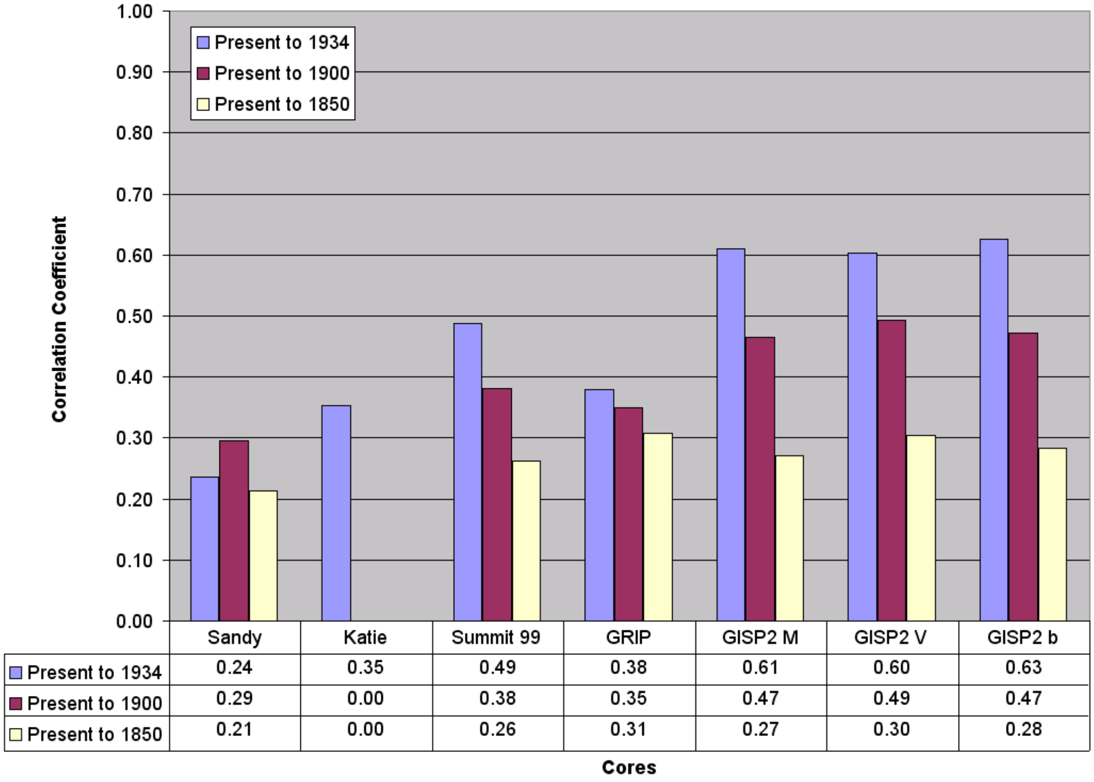

	Sandy	Katie	Summit 99	GRIP	GISP2 M	GISP2 V	GISP2 b
Present to 1934	0.24	0.35	0.49	0.38	0.61	0.60	0.63
Present to 1900	0.29	0.00	0.38	0.35	0.47	0.49	0.47
Present to 1850	0.21	0.00	0.26	0.31	0.27	0.30	0.28

Figure 4.3: Ice core and radar accumulation correlations, varying timescales Radar accumulation is correlated with the various ice core accumulation rates for three time frames. Correlation is strongest for shorter, recent, comparisons. Correlation values decrease as the time of comparison increases. Actual correlation values are presented in Table 4.1. "Present" represents 2002 for the Sandy and Katie core and 1999 for the Summit99 core. "Present" represents 1988 for the deep ice core records ([GRIP, 1997a; GISP2, 1997f], [GISP2, 1997a,b])

rates, which differ by an average of 0.04 m/yr, can vary by as much as 0.16 m/yr with eight years varying by more than 0.12 m/yr. This difference in winter-to-winter and summer-to-summer accumulation rates can be important when attempting to correlate these accumulation values with the radar-derived accumulation rate. Results of the comparisons are mixed (Figure 4.4). The highest correlation, $r = 0.69$, occurs with the winter accumulation rate from the #51 core. The second highest correlation, $r = 0.64$, occurs with core #44's summer accumulation rate. In general, no apparent trend appears when correlating the radar accumulation rate with the shallow core's winter-to-winter or summer-to-summer records. The average common time compared is thirty-two years, which appears too brief to determine any meaningful relationship between radar-derived accumulation and winter-to-winter or summer-to-summer accumulation.

Based on the Summit region map (Figure 2.2), the radar-derived accumulation rate should fall in the middle of the accumulation gradient for the nine shallow cores. When

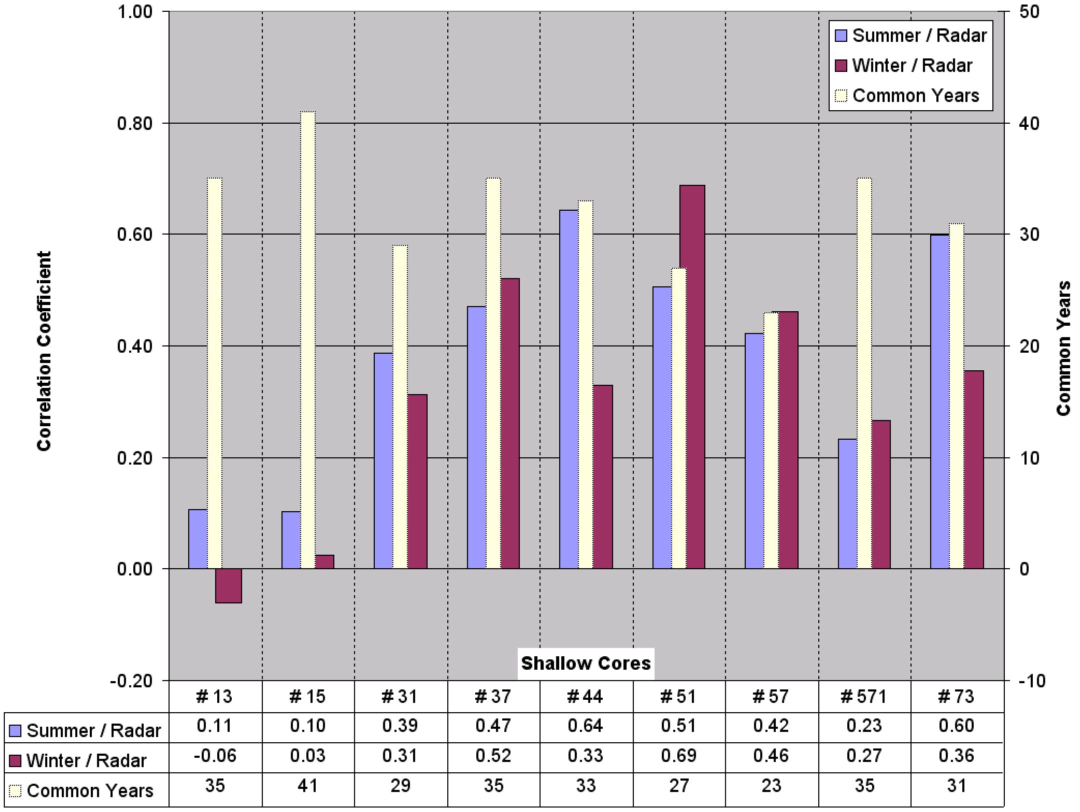

	# 13	# 15	# 31	# 37	# 44	# 51	# 57	# 571	# 73
Summer / Radar	0.11	0.10	0.39	0.47	0.64	0.51	0.42	0.23	0.60
Winter / Radar	-0.06	0.03	0.31	0.52	0.33	0.69	0.46	0.27	0.36
Common Years	35	41	29	35	33	27	23	35	31

Figure 4.4: Winter/summer shallow core and radar accumulation correlations
Shallow core accumulation rates derived using summer-to-summer and winter-to-winter layer thicknesses are compared to the radar derived accumulation rate over common time spans. The radar accumulation rate correlates with four of the nine cores for the winter accumulation rate and five of the nine cores for the summer accumulation rates. The time span compared is indicated by the middle bar (scale on the right). The average common time is thirty-two years, which appears too short to observe any difference when comparing the radar to summer or winter accumulation rates.

plotted, the radar-derived accumulation rate indeed falls within the range of the nine summer accumulation rates (Figure 4.5, upper chart).

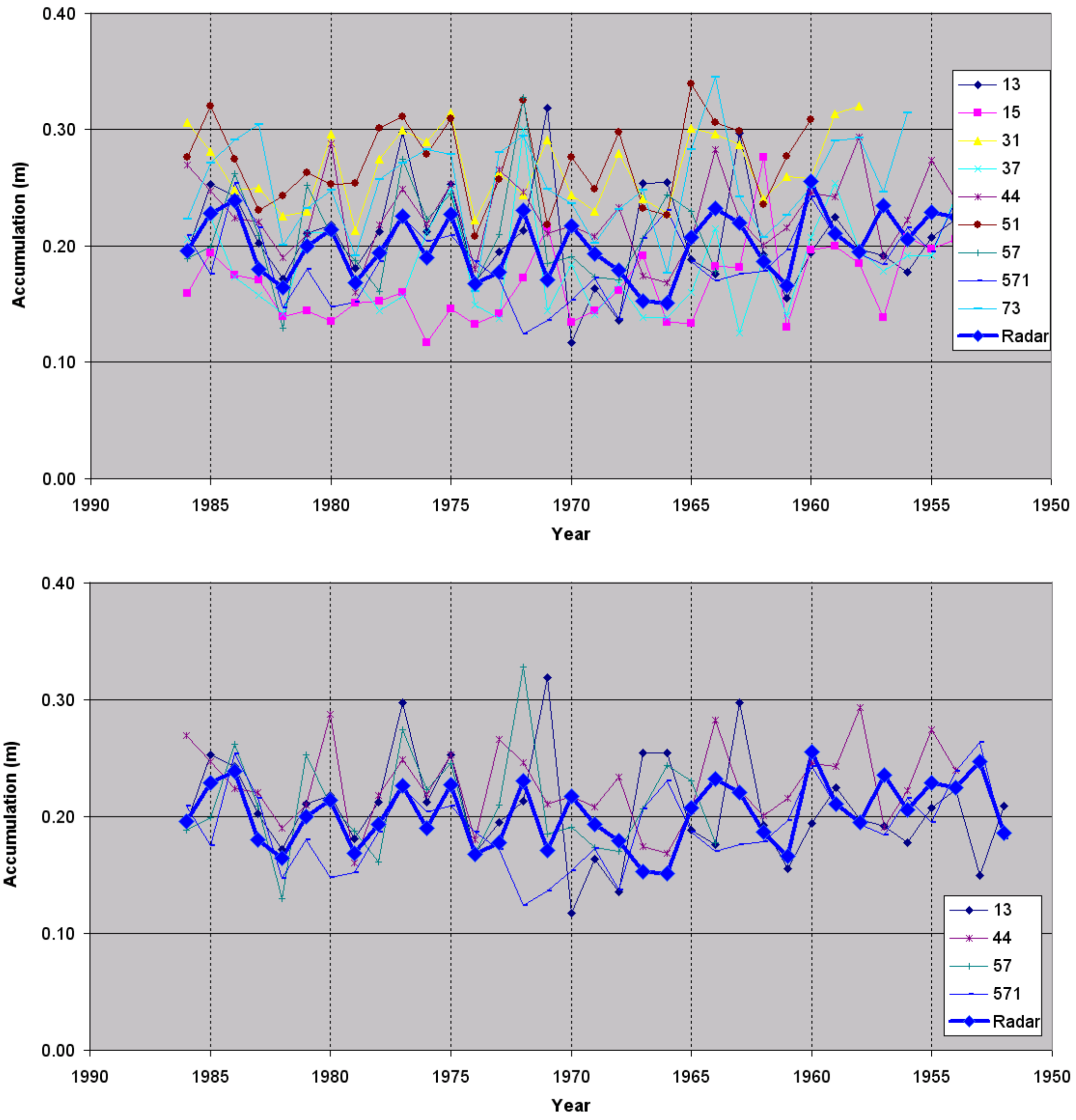

Figure 4.5: OSU Summit Cluster cores and radar accumulation rate
The upper chart displays the nine Summit Cluster cores summer accumulation rate and the radar-derived accumulation rate. The radar transect is surrounded by the nine shallow cores (Figure 2.2) and the radar-derived accumulation rate falls within the range of the nine summer accumulation rates. The lower figure focuses on the four shallow cores (#13, #44, #57, and #571) with accumulation rates similar to the radar transect [Van der Veen and Bolzan, 1999]. Despite correlations ranging from $r = 0.11$ to $r = 0.61$, the actual radar accumulation values closely resemble the four ice core accumulation rates.

This serves as yet another argument supporting the hypothesis that the traced radar layers represent accumulation horizons. Five shallow cores (#15, #31,#37, #51, #73) have average accumulation rates that differ from accumulation along the radar transect by more than 2 cm/yr 2.2. According to Van der Veen and Bolzan [1999], shallow cores #15 and #37 receive less accumulation than the radar transect. Examining the accumulation rates in Figure 4.5 (upper chart), cores #15 and #37 indeed fall below the radar-derived accumulation rate. Additionally, as indicated in Figure 2.2, the accumulation rates of cores #31, #51, and #73, exceed the radar-derived accumulation rate (Figure 4.5, upper chart).

Shallow cores #13, #44, #57, #571, have similar mean annual accumulation rates to those observed along the radar transect (Figure 2.2). The radar accumulation rate and the shallow cores #13, #44, #57, #571 have Pearson r values of 0.11, 0.64, 0.51, and 0.23, respectively. Though the correlations between these cores and the radar data range from $r = 0.11$ to $r = 0.64$, the actual radar accumulation values closely resemble the accumulation rates of the four cores (Figure 4.5, lower chart). The similarity of ice core and radar accumulation rates further supports the idea that the radar layers represent annual horizons.

Year to year correlations between radar and ice core accumulation rates are surprisingly strong given the range of ice core accumulation rates in the Summit region (Figures 4.1, 4.3, 4.5). The relationship between ice core and radar accumulation rates can be further examined by looking at long-term temporal trends in accumulation. Studies by Banta and McConnell [2007] and Hawley et al. [2008] saw increased correlation when accumulation rates were averaged over longer time periods.Using the GISP2 core to calculate a 30 yr moving average of accumulation smoothes out interannual fluctuations and provides a trend of Summit region accumulation for which to compare the radar-derived accumulation rate. Inspection of accumulation over longer time periods addresses the problem of missing or extra accumulation layers that result in an offset of counted layers down to established volcanic horizons (Table 3.1). An extra layer from a secondary temperature maxima or a weak reflecting radar layer that leads to an offset will be smoothed out when looking at the long-term thirty-year moving accumulation. Visually examining the thirty-year moving average of accumulation records for ice cores and radars, two observations stand out (Figure 4.6). First, the radar thirty-year moving accumulation record follows quite closely the general rise and fall of the ice core accumulation records. Pearson's r correlation confirms visual observations; r values nearly double from the correlation of annual accumulation rates presented in Figure 4.3. For the period from 1974 to 1850, GISP2 V improves from 0.30 to 0.68, GISP2 b improves from 0.28 to 0.59, GISP2 M improves from 0.27 to 0.48, and GRIP

improves from 0.31 to 0.62. These strong correlations in long-term accumulation reinforce the hypothesis that the radar layers represent annual horizons. The second observation is that the radar data underestimates accumulation by approximately ten percent compared to the ice cores. The underestimate may result from using a composite density profile, and therefore a permittivity ϵ_r curve (Figure 4.6), which is applied to the entire radar transect. Limitations in tracing layers along the maximum reflection values (in the midst of winter but not necessarily the winter maxima, which is often used to determine ice

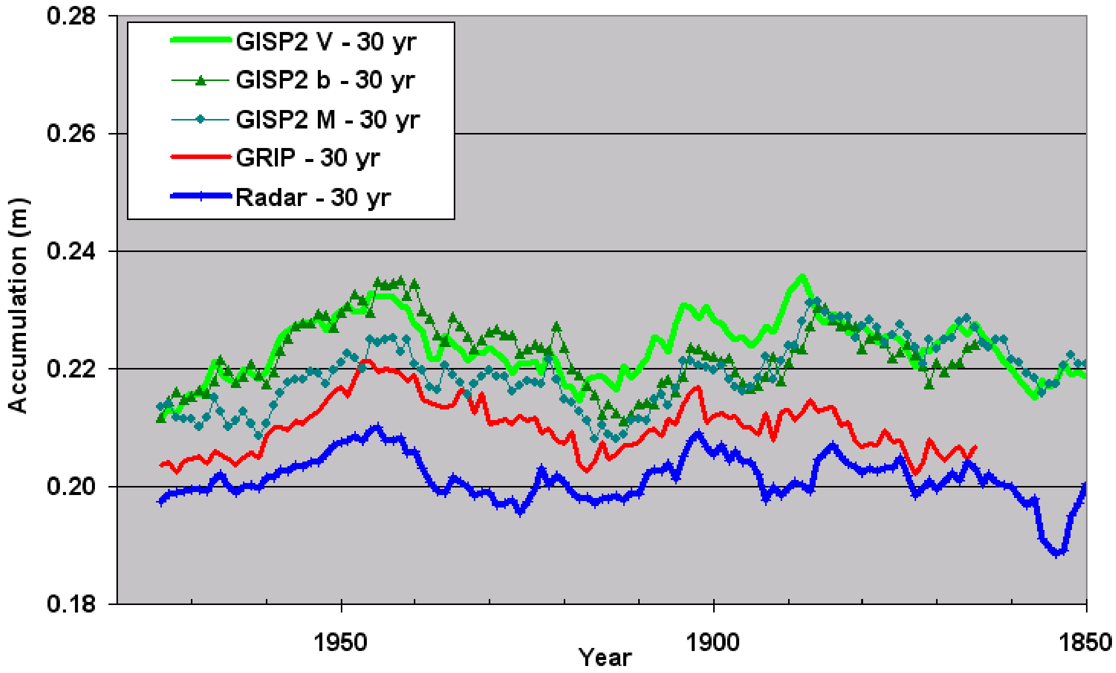

Figure 4.6: Thirty year moving average of ice core and radar accumulation Thirty year centered moving average of four ice core accumulation records (GISP2 V, GISP2 b, GISP2 M, and GRIP) are compared to the thirty year centered moving average radar accumulation. Radar accumulation correlates strongly with the ice core records. Pearson's r = 0.68 for GISP2 V, 0.59 for GISP2b, 0.48 for GISP2 M, and 0.62 for GRIP

core accumulation rates) may also contribute to or explain the radar's underestimate of accumulation compared to the ice cores. Hawley et al. [2008] found that choice of annual-layer location (where to trace accumulation horizons) had a greater impact on accumulation rate than the density conversion used. Thus the radar's accumulation underestimate may primarily be due to the choice of tracing the radar horizons through the maximum reflection intensity, with choice of density profile being a less significant contributor to the underestimate. The radar accumulation underestimate is not unique for near-surface studies. The Borehole Optical Stratigraphy (BOS) method underestimated accumulation over the past 30 years in comparison to other accumulation records [Hawley et al., 2008].

Selecting the ice cores accumulation records with either the strongest correlation to the radar-derived accumulation record and the cores with similar annual accumulation rates (Figure 2.2), a mean ice core accumulation record is compiled for comparison to the radar-derived accumulation rate (Figure 4.7). The mean ice core accumulation rate is created from seven ice core records: GISP2 V, GISP2 M, GISP2 b, Summit99, #13, #57*, #44, #571. The composite ice core record and the radar accumulation share a common time span of 1986 to 1959 (*#57 timespan is 1986 to 1965), and have a remarkably strong correlation of r =0.75. Though the time span compared is brief, the agreement in both accumulation amount and year-to-year trend, support the hypothesis that the radar layers represent isochronal accumulation horizons. The underestimate in radar accumulation observed in Figure 4.6 is not as pronounced in Figure 4.7 because of the short time span of the comparison and the fact that the accumulation rates are annual rather than a 30yr moving average.

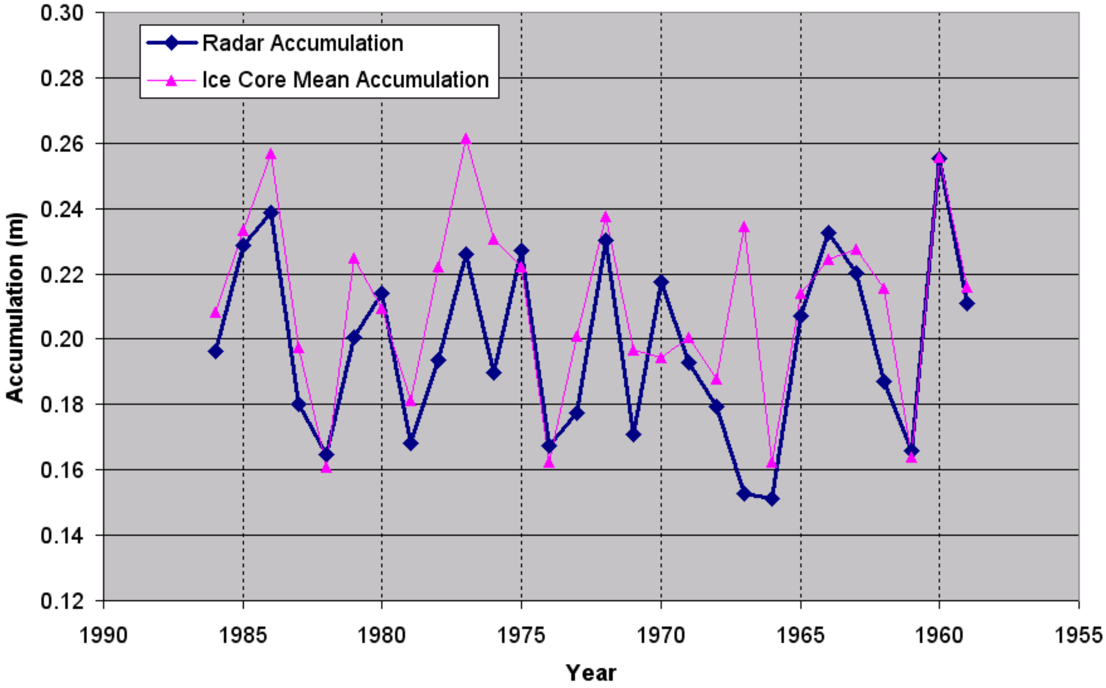

Figure 4.7: Radar accumulation vs. mean accumulation of ice cores
The mean annual accumulation of seven ice core records are compared with the mean radar annual accumulation across the entire radar transect. The two accumulation records have a Pearson's correlation coefficients of $r = 0.75$

4.2 Accumulation Characteristics

The variations in ice core accumulation records presented in Section 4.1 (Figures 4.1 and Figure 4.5) may be due to topographic effects, snow redistribution by wind action, and synoptic-scale fluctuations in precipitation [Van der Veen and Bolzan, 1999]. In contrast to the individual ice core records, accumulation radar data presented in this thesis expands the view of accumulation from ice core point locations to two-dimensional accumulation horizons connecting ice core records. The accumulation rates computed in 4.1 Section 3.3 represent the average annual accumulation for the entire transect of radar data connecting the GISP2 and GRIP cores. In addition to this overall average accumulation of the radar transect, the radar derived accumulation rates can also be analyzed both spatially and temporally. Accumulation spanning a spatial area may be used to examine regional trends in variation in accumulation and climate variability. Van der Veen and Bolzan [1999] characteristics of net accumulation in central Greenland are used to describe the radar-derived accumulation record.

Three processes contribute to the interannual fluctuations in net accumulation: spatial noise, climate variability, and random measurement errors [Van der Veen and Bolzan, 1999]. Thus, the annual net accumulation rate, A(x,t), at horizontal position x and time t can be written as:

$$A(x,t) = A_o(x,t) + A_s(x,t) + A_c(x,t) + \epsilon \tag{4.1}$$

where A_o is the long-term average accumulation, including slowly varying climate trends and effects from large-scale surface undulations; A_s is the spatial noise associated with small scale (∼1 km or less) microrelief, such as wind-blown sastrugi, of the snow surface; A_c is the contribution from fluctuations associated with the synoptic-scale climate variability which are assumed to be uniform over large areas; and ϵ is the measurement error, calculated in 3.3 as ±0.04 m/yr [Van der Veen and Bolzan, 1999].

The radar transect has 11,530 horizontal positions with a calculated annual accumulation rate (recall Figure 2.8, thus an accumulation rate at approximately every 2.7 meters). The accumulation rate at each position, x, averaged over the period 2004 to 1653, represents the accumulation gradient along the radar transect (Figure 4.8).

Figure 4.8 depicts the temporal mean for every accumulation point along the transect, or the mean of 352 years of accumulation, at each of the 11,530 points along the transect. The temporally averaged accumulation for each position along the transect is then averaged to give the radar's mean annual accumulation of 0.217 meter/year. This compares favorably with the GISP2 and GRIP mean annual accumulation rate for that period, 0.224 and 0.210 m/year respectively [Dahl-Jensen et al., 1993; Meese et al., 1994; GRIP, 1997a; GISP2, 1997a]. The difference between the GISP2 and GRIP accumulation rates is reflected in the accumulation rate along the radar transect. The radar-derived accumulation rate decreases from GISP2 to GRIP (left to right, east to west) as the radar approaches the ice divide. The decrease in accumulation along the transect is inverse to the elevation along the transect (Figure 2.3), as expected from the high-elevation blocking effect on cyclonic activity over the central ice sheet [Dethloff et al., 2002].

The spatial mean, or average accumulation of the 11,530 accumulation points for a given year, t, is represented by taking the spatial average of Equation 4.1, (spatial average along the entire transect is denoted by <>),

$$< A(x,t) >=< A_o(x,t) > + < A_s(x,t) > + < A_c(x,t) > + < \epsilon > \tag{4.2}$$

The radar-derived accumulations rate presented in Figure 4.9 (upper plot) is the spatially averaged accumulation across the entire transect, $< A(x,t) >$. Based on

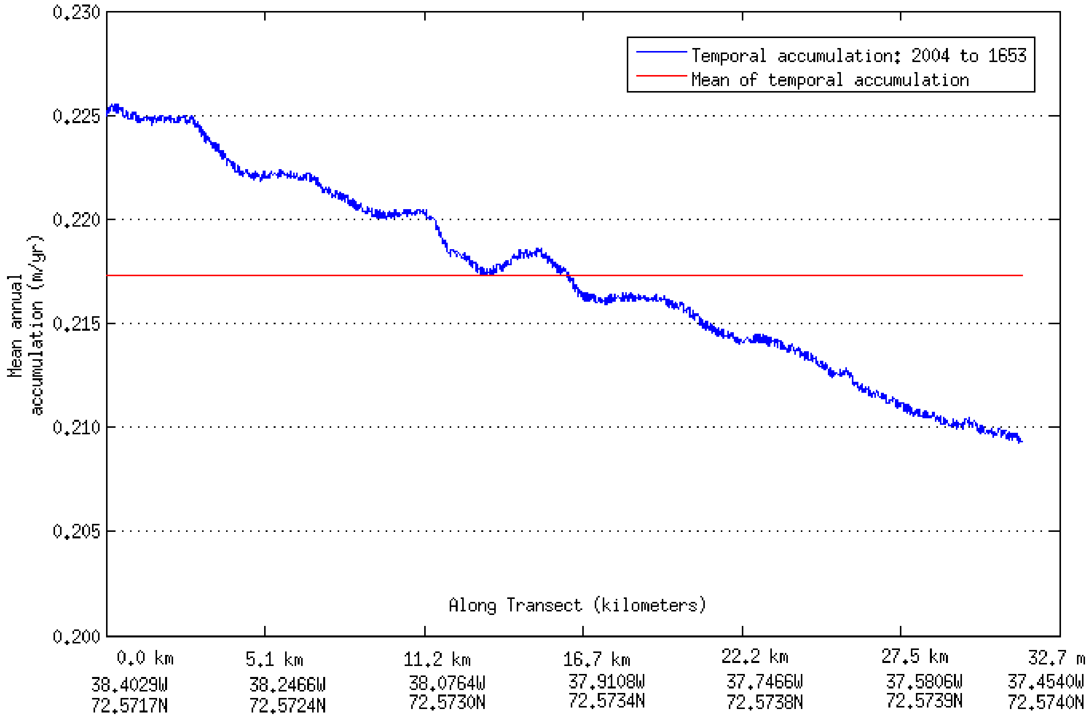

Figure 4.8: Accumulation gradient along the radar transect
The temporal accumulation rate along the transect, A'(x), represents the mean accumulation rate over the period 2004 to 1653 at each of the 11,530 positions along the radar transect. The accumulation rate decreases from GISP2 to GRIP (left to right, east to west) as the radar approaches the ice divide. The mean annual accumulation across the transect is 0.217 meters/year.

assumptions made by Van der Veen (1998; 2009), averaging accumulation for each layer across the entire thirty kilometer radar transect (with 11,530 accumulation values per layer) cancels spatial noise and measurement error (this is different from the Van der Veen and Bolzan [1999] Summit study which only had nine ice core records). Recall from above that systematic micro-climate influences and long term effects are included in the long-term average accumulation, A_o. Thus average spatial noise and measurement error are considered negligible for these average layer values:

$$< A_s(x,t) > \approx < \epsilon > \approx 0 \tag{4.3}$$

Then,

$$< A(x,t) > = < A_o(x,t) > + < A_c(x,t) > \tag{4.4}$$

(Figure 4.9)

The relatively small area (30 km transect) covered by the radar data justifies the assumption that synoptic-scale variability is constant over the region from year-to-year. For example, if it snows more at one point along the transect, it snows more at other points along the transect[Van der Veen, 2009a]. Therefore,

$$< A_c(x,t) >= A_c(t) \tag{4.5}$$

(Figure 4.9)

This term represents fluctuations in accumulation associated with synoptic scale interannual climate variability. The slowly-varying climate trend, $< Ao(x,t) >$, is computed from the running thirty-year mean of the spatially-averaged annual accumulation along the transect, $< A(x,t) >$. Subtracting the long-term annual accumulation $< A_o(x,t) >$ from $< A(x,t) >$ gives a record of climate variability, $A_c(t)$ (Figure 4.9), which is used to evaluate changes in climate variability [Van der Veen, 2009b].

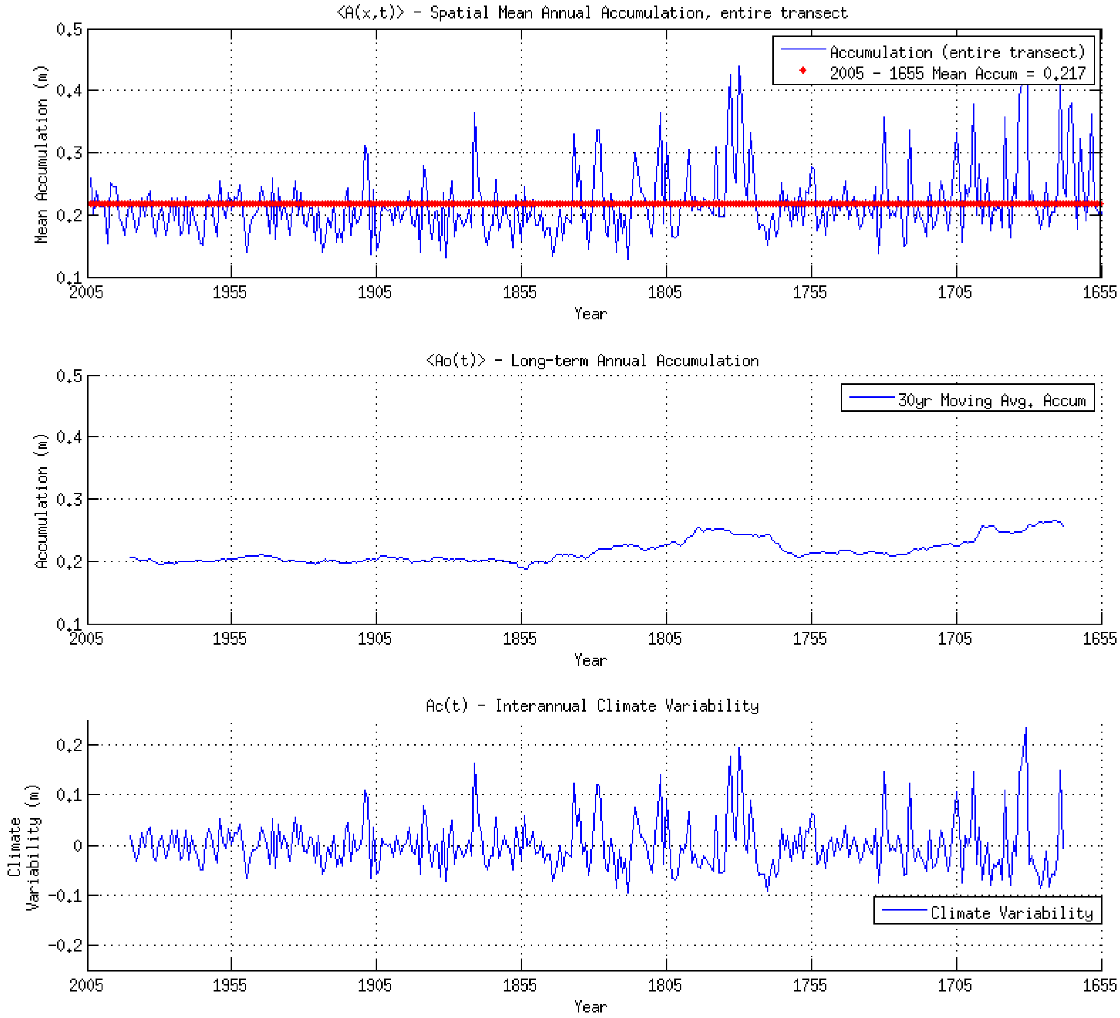

Figure 4.9: Accumulation characteristics
The radar-derived accumulation rate, spatially averaged across the entire transect ($< A(x,t) >$) is plotted alongside the thirty-year moving average of $< A(x,t) >$. Interannual climate variability, $A_c(t)$, is determined by subtracting the long-term annual accumulation, $< A_o(t) >$, from $< A(x,t) >$.

4.2.1 Interpretation of radar-derived Accumulation Record

Layers are analyzed both temporally (successive layers of accumulation over increasing depth in the ice sheet) and spatially (thickness and variation of an annual layer across the entire radar transect). In order to obtain accurate estimates of accumulation, spatial and temporal noise in the record must be accounted for and removed. Interannual climate variation of accumulation may lead to apparent trends in ice thickness that could be erroneously interpreted as climatically significant [Van der Veen, 1993]. Van der Veen et al. [1998] examined how surface irregularities lead to spatial noise that affects the thickness of annual accumulation layers. Methods used by Van der Veen et al. [1998] to determine surface roughness at Summit, Greenland, are applied to the radar layers.

4.2.2 Spatial Variability of Accumulation

Spatial Noise

Spatial noise associated with small-scale surface micro-relief, is assumed to average out when discussing accumulation in terms of an average amount over the spatial area covered by the radar transect (Equation 4.3). When considering the 11,530 individual accumulation values along the transect, spatial noise can be examined. Spatial noise, $A_s(x,t)$, can be described by rearranging Equation 4.1 and including temporal mean accumulation rate $A'(x)$, from Figure 4.8:

$$As(x,t) = A(x,t) - A'(x) - A_o(t) - A_c(t) - \epsilon \tag{4.6}$$

(Figure 4.9)

Spatial noise at each point along the transect is calculated by starting with the measured accumulation rate at position x, time t, A(x,t), then subtracting out the long-term accumulation rate at position x, A'(x), subtracting out the long-term average accumulation rate across the entire transect, Ao(t), subtracting out the synoptic-scale climatic variability for year t, Ac(t), and subtracting out the measurement error. An example of spatial noise across an accumulation layer is plotted in Figure 4.10 (layer 1905 A.D. chosen at random). The assumption (from Van der Veen 1998 and 2009) that spatial noise averages to 0 over large spatial areas are confirmed by the radar-derived spatial noise, which averages to 0 m across the entire transect. Spatial noise may be as much as ±0.1 m at any given horizontal position, but averages to 0 m across the entire radar accumulation layer (Figure 4.10).

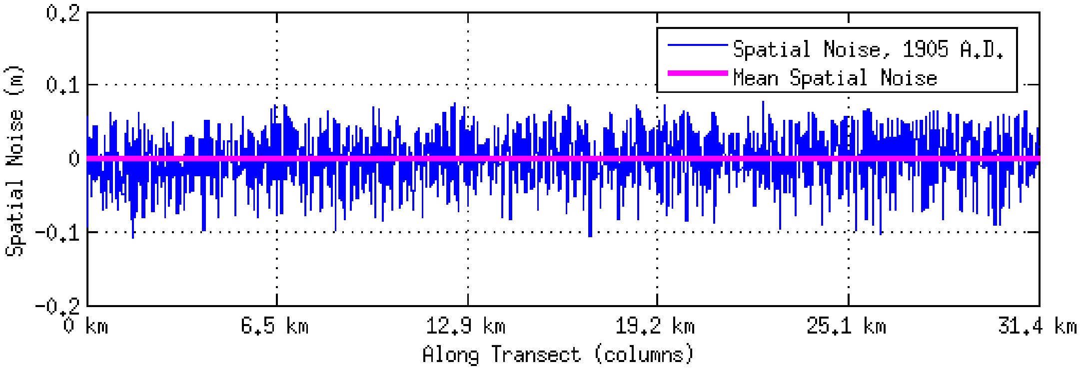

Figure 4.10: Spatial noise across the radar transect
The spatial noise, As(x,t), calculated from Equation 4.6, is plotted at each of the 11,530 horizontal positions (or radar columns) for the 1905 A.D. accumulation layer. As described in Section 4.2, the spatial noise is 0 when averaged over the entire transect. The spatial noise estimate includes noise from measurement error.

Though mean spatial noise is negligible, the standard deviation of spatial noise is useful for describing how spatial noise varies temporally (Section 4.2.3). Though the radar-derived spatial noise results are encouraging, a key factor when computing the record must be considered when discussing the validity or use of the spatial noise data beyond this thesis. Similar to previous ice core and near-surface radar studies (*e.g.*, GISP2 [1997g]; Banta and McConnell [2007]; Hawley et al. [2008]), radar-derived accumulation rates are constructed from year-to-year summer maxima or winter minima of various physical or chemical properties. Thus the accumulation rate is constructed from two former deposition surfaces and therefore contains spatial noise from two consecutive years. This limitation in discussing spatial noise is avoided by treating the horizons as former deposition surfaces and looking only at the traced horizon itself rather than the entire accumulation layer.

Surface Roughness

Assuming traced layers represent former deposition surfaces, they can then be compared to surface perturbations described in Van der Veen et al. [1998]. The assumption is reasonable considering that all previous radar surveys listed in Section 1.2 consider radar reflections to be isochrones (layers of equal age). Comparing small-scale topographic features will provide an improved understanding of how accumulation varies spatially.

For the comparison, the radar-derived surface perturbations are prepared in the same manner as the surface perturbation values in Van der Veen et al. [1998]: local relief of each radar layer is obtained by dividing the ∼30km radar transect into 0.5km sections. For each section, the large-scale slope is considered constant and the average surface represented by a straight line is determined using least-squares fitting [Van der Veen et al., 1998]. The difference between the traced radar layer and this best-fit line represents the small-scale perturbations. Similar to Van der Veen et al. [1998], the typical shape of sastrugi can be inferred from plotting surface perturbations over the length of the transect (Figure 4.11)

A layer's surface roughness (how the surface varies spatially) can be determined by taking the standard deviation of the fluctuations of the layer's position from the slowly-varying mean position of the layer over the 0.5km section. Surface roughness is then calculated for each of the 350 radar layers, providing both a history of roughness over time (moving down through the ice) and space (with a surface roughness measurement for every 0.5km section). Fisher et al. [1985] assume that changes in surface over distances less than a few kilometers can be described by a stationary Gaussian distribution. The frequency distributions of the radar-derived accumulation surfaces show only minor deviation from the Gaussian distribution. Similar to Van der Veen et al. [1998], more frequently occurring perturbation are negative with a slightly asymmetric tail on the positive side. Figure 4.12 plots the distributions of surface irregularities for the 1988 surface. Overall, the distribution of surface perturbations for the 350 radar-derived surfaces compares favorably to the frequency distributions of surface perturbations from Van der Veen et al. [1998].

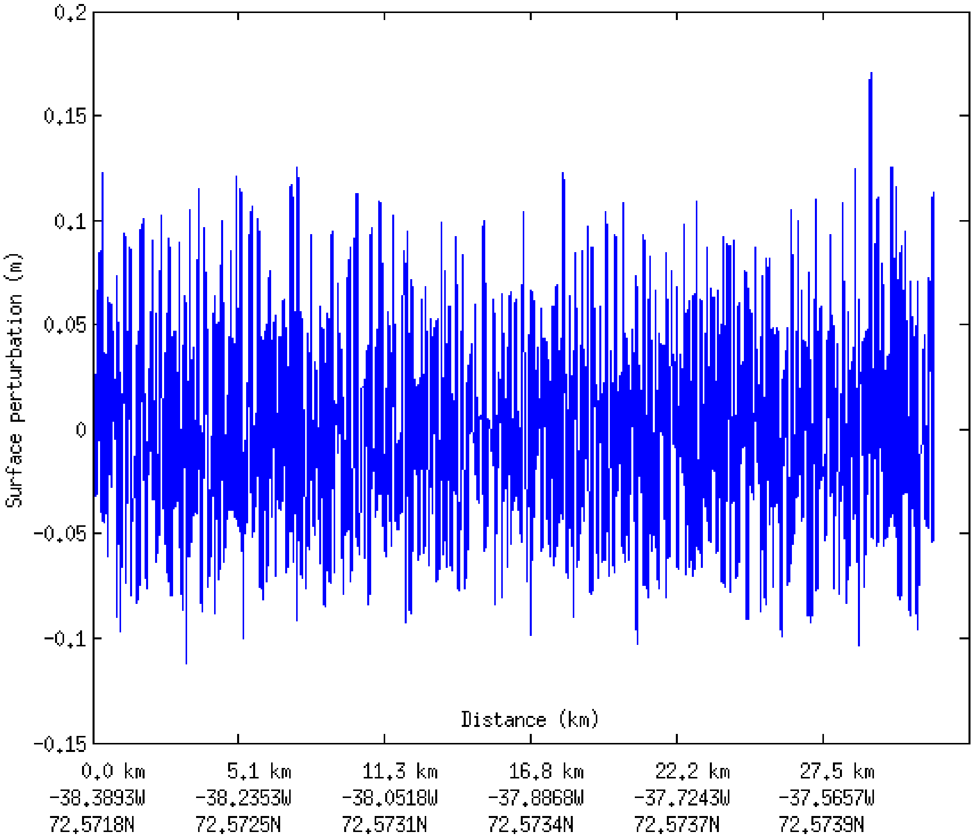

Figure 4.11: Surface perturbations across the radar transect
The surface perturbations for the 1988 accumulation layer. Perturbations fall within range of surface irregularities observed by Van der Veen et al. [1998].

Computing surface roughness, and analyzing the distribution and standard deviation of this roughness, answers the question of how accumulation varies spatially (by looking at values across a layer) and temporally (by comparing values at increasing depths). These radar derived spatial patterns compare favorably to the findings of [Van der Veen et al., 1998] and [Van der Veen et al., 2009].

Examining the standard deviation of surface roughness over the 0.5 km segments give an estimate of the fluctuations in elevation from the slowly-varying mean. The standard deviation of small-scale surface roughness across the 0.5 km segments for each of the upper and lower 10 layers (layers 1–10 and layers 340–350) are plotted in Figure 4.13. The standard deviations for the upper and lower 10 layers are slightly higher than those determined by Van der Veen et al. [1998]. The average standard deviation of surface roughness for the East-West line used by Van der Veen et al. [1998]) is 0.045 m, while the East-West radar transect has an average standard deviation of surface roughness of 0.065 m (Figure 4.13). The fact that the upper and lower 10 radar layers have similar

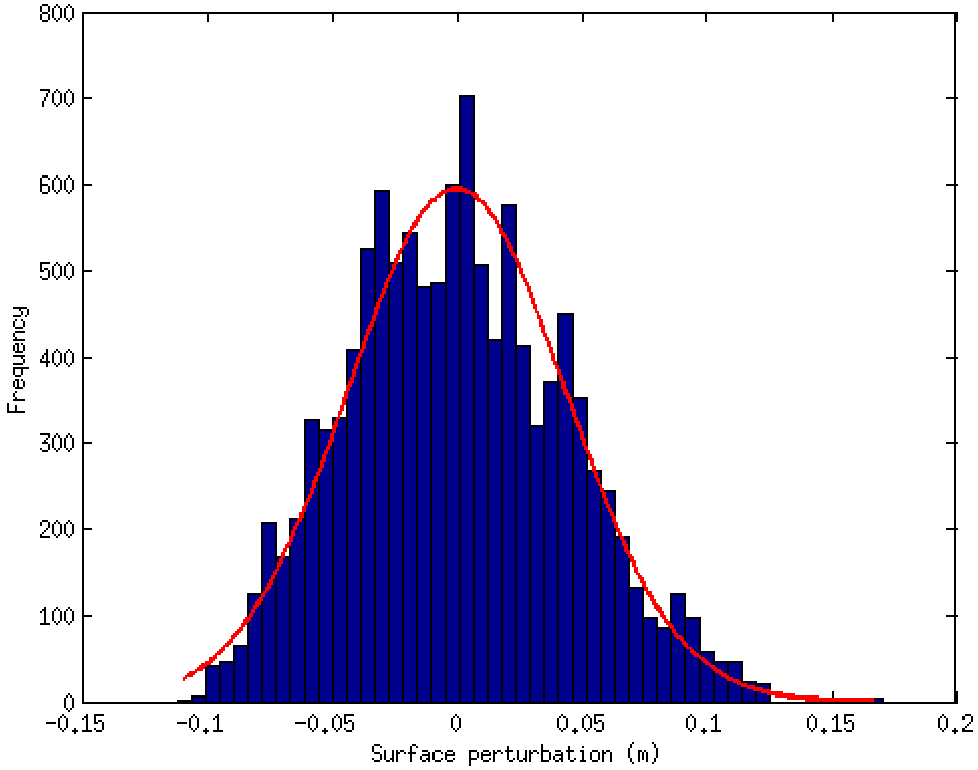

Figure 4.12: Frequency distribution of surface perturbations for 1988 accumulation surface

standard deviations of surface roughness is encouraging. Based on the original assumption that the radar horizons are former deposition surfaces, a similar standard deviation of surface roughness of both shallow and deep radar horizons indicates that the deeper layers remain useful for examining surface roughness despite compaction. Examining the shallow and deeper layers in this manner assumes that the conditions leading to the formation of surface perturbations have remained constant in the Summit region over the 350 yr period separating the upper and lower 10 layers. Since small-scale surface irregularities are associated with sastrugi and other wind-formed features [Van der Veen et al., 1998], the assumption about conditions for formation extend to wind patterns. This assumption is fair given Van der Veen et al. [1998] statement that

> other than forming in the prevailing wind direction, there is no evidence suggesting that the formation of Sastrugi is anything but a random process.

Accumulation at different spatial scales

Another approach to examining how accumulation rates vary is to average these rates over various spatial distances (Figure 4.14. For example, each point in the "10 m" averaging

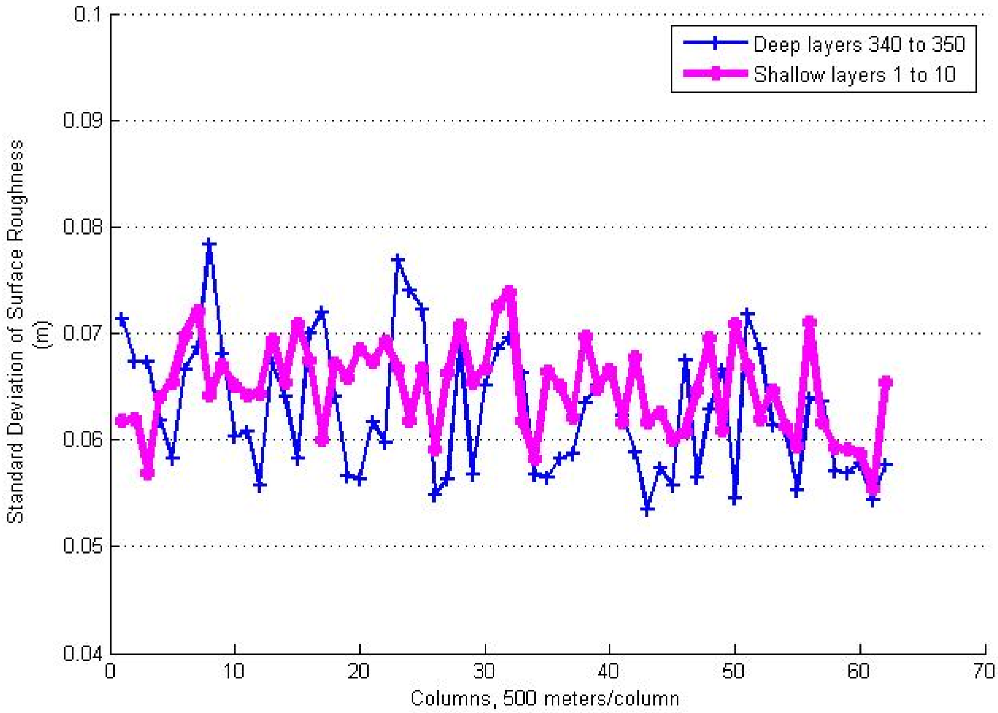

Figure 4.13: Standard deviation of surface roughness
The standard deviation of surface roughness is compared at different depths. The average surface roughness of ten near surface layers 1 through 10 and the average of deeper layers, 340 through 350 are compared. These values compare favorably with Van der Veen et. al. 1998.

distance line in Figure 4.14 represents the average of approximately four radar accumulation rates spanning approximately 10 horizontal meters. The “100 m” averaging distance represent the average accumulation of 37 radar accumulation rates at approximately every 100 horizontal meters (37 radar columns $\times 2.7$ m/column $= 99.9m$).

For the 1995 accumulation year depicted in Figure 4.14, large variations exist when averaging accumulation over short distances (10m up to 100m). Accumulation values averaged over shorter distances are more susceptible to small-scale surface irregularities associated with sastrugi and other wind-formed surface relief. The range of accumulation variability narrows at the 100m averaging distance. A regional accumulation trend begins to emerge at 500 meters averaging distance, and is further smoothed at the 1000m and 2000m averaging distances (Figure 4.14). Figure 4.14 depicts how accumulation varies spatially along the radar transect for one year (1995). All 352 annual accumulation layers were examined in this manner to gain an understanding of how accumulation varies at different spatial scales, over the past 352 years. Figure 4.15 depicts the standard deviation of accumulation both spatially and temporally. Accumulation is averaged over different horizontal distances, for the 352 accumulation years. The x-axis represents averaging

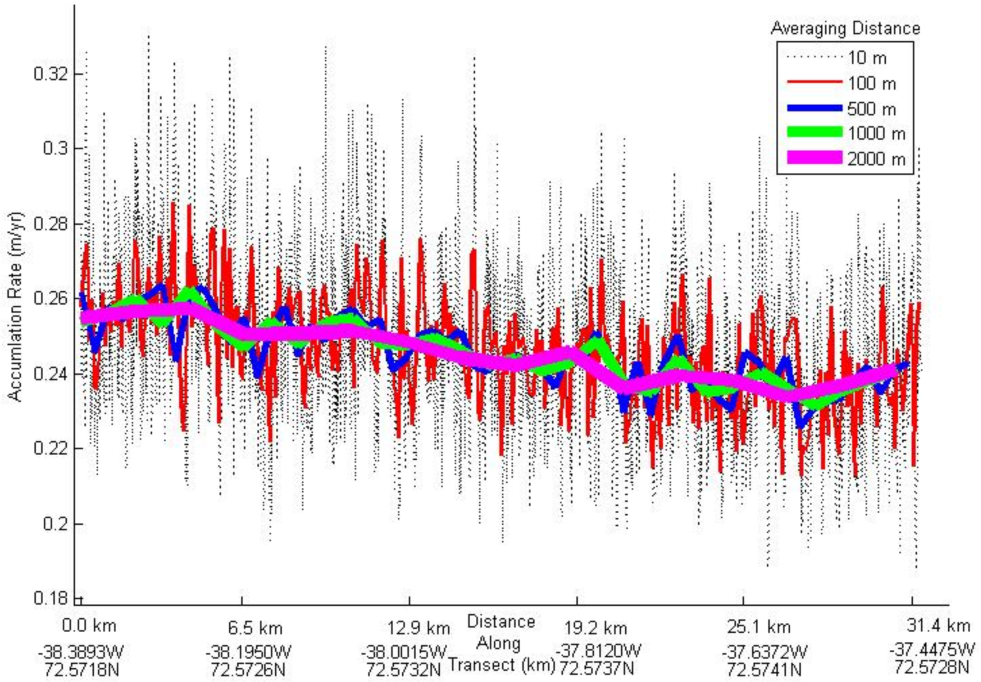

Figure 4.14: Accumulation rate over different averaging distances
The accumulation rate across the radar transect, averaged over distances of 10, 100, 500, 1000, and 2000 meters, for a single accumulation year (1995, chosen arbitrarily). The accumulation rate variability decreases as averaging distance increases. The increasing accumulation gradient found from GRIP to GISP2 is reflected in the 1995 radar accumulation rate.

intervals that the transect was divided into, thus with 100, the 31.2 km transect was sectioned into 312 sections, 100 meters in length, whereas with 1000 the transect was divided into 31 sections of 1000 meters in length.

4.2.3 Temporal variability of accumulation

The spatially averaged accumulation rate, $< A(x,t) >$, averages ~0.20 meters/year until around 1908. The further back in time, the more frequent the occurrence of accumulation rates greater than 0.30 m/yr. Several outliers with accumulation exceeding 0.40 m/yr occur in 1783, 1780, 1682, and 1681. These large accumulation years should be viewed with caution as they may possibly indicate missed layers in the radar record. The ice core accumulation rates for these years are above average, but do not approach 0.40 m/yr. Actual layer thicknesses exceeding 0.40 m are observed in the GISP2 ice core (Figure 3.4), but theses thicknesses do not correspond temporally to observed outliers in the radar record. Additionally, the Laki volcanic eruption is recorded in the ice core record in 1783. Volcanic debris deposited over the course of the year may have impacted the reflection of the 1783 accumulation layer, causing a thicker reflection horizon to appear. Yet another possible

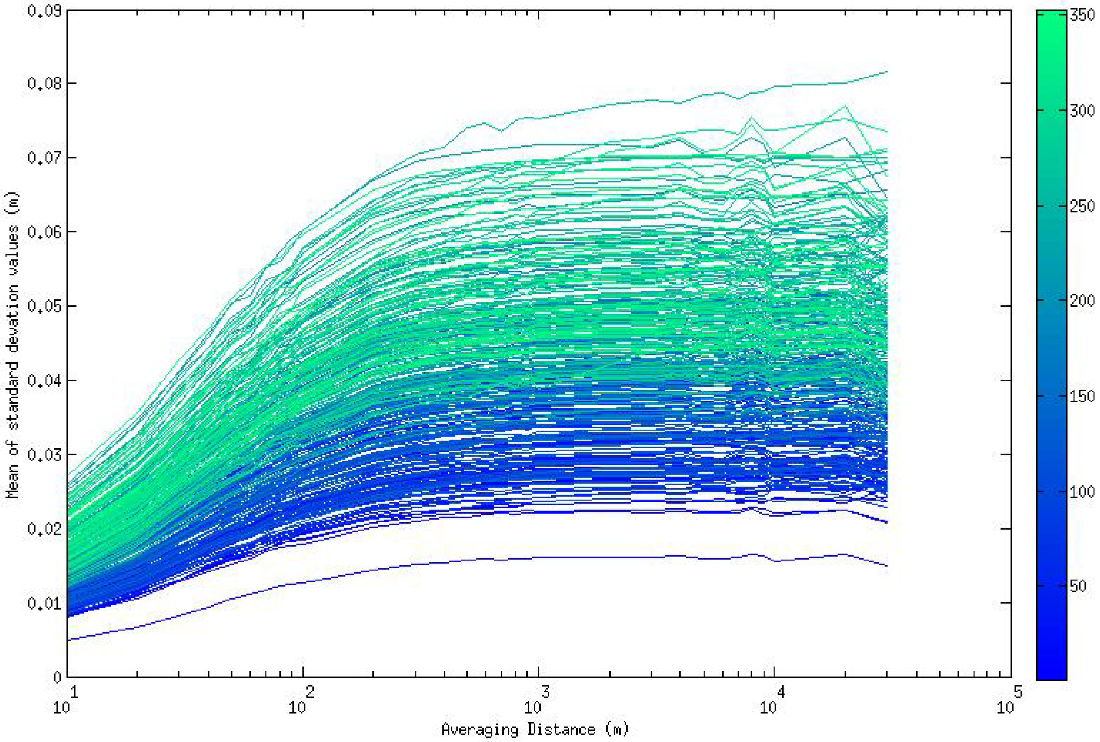

Figure 4.15: Mean standard deviation at different averaging distances
The accumulation rate is examined at different spatial scales over the entire radar transect. The standard deviation of accumulation over different scales is presented for each of the 352 radar accumulation layers traced. Temporally, standard deviation of accumulation increases with depth, which is represented by the blue-to-green color bar, ranging from layer 1 (near-surface) to layer 352 (deepest layer). At all depths, standard deviation values of accumulation begin to level off around 500m and flatten between 1000-2000m. This is interpreted to mean that a regional accumulation rate can be determined by averaging accumulation over 1000m spatial distance. Note the 'Average Distance' axis uses a logarithmic scale.

explanation for the abnormally large radar-derived accumulation rates may be the use of the same composite density profile (Figure 2.7) across the entire transect when converting from layer thickness to water-equivalent thickness (though Eisen et al. [2008] expect errors from extrapolating density values to be small). An anomaly in density near the depths of 1783, 1780, 1682, or 1681 layers would not be reflected in the calculation of the radar-derived accumulation's water equivalent thickness. For example, using the composite density profile (Figure 2.7) to convert the anomalous 0.58 m/yr thick layer at 75 m depth in the GISP2 record (Figure 3.4), density at 75 m depth is $\approx 0.820 g/cm^3$, resulting in a water equivalent thickness of 0.47 m/yr. An anomaly in density of $\approx 0.70 g/cm^3$ (which is not observed in any of the ice core records) would result in a water equivalent thickness of 0.40 m/yr, which would still be an extremely thick accumulation layer.

Examining the accumulation rate from Figure 3.9 over the periods of "missed" and “extra” layers may provide a reasonable explanation of anomalously thick and thin accumulation layers observed (see Table 3.1), “missed” and “extra” layers are described as “Offset” and determined by counting layers between intensely reflecting dated volcanic horizons). Two consecutive “thin” accumulation layers could actually represent a single accumulation year that had a secondary warming period (Section 3.2.4) or a large storm event [Hawley et al., 2008] that resulted in a thin reflection horizon that was traced as annual accumulation horizon. Thus for a period with “extra” layers, it would be expected to find several consecutive low or “thin” accumulation rates. Layers may be “missed” when one particularly “thick” accumulation layer could instead represent two layers separated by a faint horizon that was “missed”. Splitting these “thick”layers into two layers would account for the missed layer, and balance out the count between the known horizons.

From the 2005 surface to the 1912 Katmai eruption horizon, three “extra” layers are counted. The accumulation rates during this period are fairly stable, but there are several accumulation layers with consecutively low accumulation years (Figure 3.9). From 1912 to 1810, a layer is counted for each year, thus no “extra” or “missed” layers are suspected (though there are a few thick and thins layers, which may offset each other). From 1810 to 1784, three fewer layers are counted than the number of years expected, thus “missed”. During this relatively short time span (26 years), several thick layers appear. If one of these “thick” layers actually represents two separate accumulation horizons, then the layer-to-year count would be close to being balanced. From 1784 to 1755, no anomalous “thick” or “thin” layers are observed and the layer-to-year count is exact. From 1755 to 1732, two extra layers are counted with a few thinner layers and no thick layers observed. From 1732 to 1668, where both thin and thick layers are observed, two layers are “missed”. Overall, “missed” layers generally coincide with periods in which “thick” high accumulation years are observed and “extra” layers are counted during periods in which “thin” low accumulation rates occur. Additionally, as mentioned in Section 3.2.3, “extra” layers due to large storm events may gradually compact with depth, thus explaining improved year-to-layer counts with increasing depth [Hawley et al., 2008]. Despite “missing” or “extra” layers, the radar still provides a reliable estimate of accumulation, as presented in Section 4.1.

Recall that “extra” or “missing” layers in the accumulation record are overcome by examining the accumulation rate over longer time intervals (Section 4.1, Figure 4.6). Viewing accumulation rates over longer time intervals not only smooth out annual accumulation anomalies, but also provide a historical, or temporal, record of accumulation and accumulation characteristics. Starting with Figure 4.9, the mean accumulation rate from 2005-1653, 0.217 m/yr, is subtracted from the spatially averaged long-term 30-yr moving accumulation rate, ¡Ao(t)¿, to give the mean adjusted long-term annual accumulation rate (Figure 4.16). The mean adjusted long-term accumulation record is presented alongside climate variability, Ac(t), and the standard deviation of spatial noise for 2005–1655. As show by the layers’ color-scale in Figure 4.15 above, and the spatially averaged accumulation rate in Figure 4.9 (upper plot), the standard deviation of accumulation increases with depth (time/age). It is therefore not surprising that the standard deviation of spatial noise of accumulation also increases with depth (time/age) (Figure 4.16, lower plot). But, it is unclear if the variability of spatial noise was actually increased during earlier time periods, or if the variability is a function of depositional factors. Deeper layers exhibit undulations, partly caused by compaction from overlying layers (recall Figures 3.1 and 3.2). Thus it is difficult to separate the variability in spatial noise at the time the layer accumulated and the variability in spatial noise resulting from depositional processes. Additionally, as discussed in Section 4.2.2, radar-derived accumulation rates are constructed from two accumulation horizons (winter-to-winter annual markers), and therefore contain noise from two former deposition surfaces. Combining this uncertainty with the poor distinction between actual spatial noise at the time of deposition and noise caused from the deposition/compaction process, the temporal (or year-to-year) description of variability of spatial noise (Figure 4.16, bottom plot) is unreliable. This uncertainty only applies to year-to-year variability of spatial noise and does not impact confidence in the spatially averaged radar accumulation rate, as the random component associated with spatial noise cancels out when averaged over the entire radar transect (Figure 4.10) [Van der Veen and Bolzan, 1999].

The spatial noise uncertainty also does not impact the surface roughness estimates (Figures 4.11–4.13), as those calculations were based on individual radar horizons and thus do not contain noise from two former deposition surfaces.

Despite the year-to-year flaws regarding spatial noise, a general representation of temporal variability of accumulation is useful. The mean adjusted long-term accumulation rate (Figure 4.16, upper plot) shows the 30 yr moving average accumulation rate, adjusted by the mean accumulation rate over 2005–1655. The variability of this record over the period 2005–1850 (a period with good accumulation agreement in the ice cores, *e.g.* Figure 4.2) is examined and compared with long-term ice core records (Figure 4.17). The standard deviation of the 30yr moving average accumulation rate for the radar is lower than the standard deviation of the ice cores' 30 yr moving average accumulation. Van der Veen and Bolzan [1999] estimated that spatial noise and temporal variability have about the same standard deviation. Van der Veen et al. [1998]; Van der Veen and Bolzan [1999], also found that the stratigraphic noise in an accumulation rate has a standard deviation $\sqrt{2}$ times greater than the standard deviation of the surface perturbations from the large-scale trend. This relationship applies to stratigraphic layers bounded by two random surfaces, as is the case with the radar-derived accumulation rate [Van der Veen and Bolzan, 1999]. These two findings on the variability of spatial noise can compared to the temporal radar-derived accumulation record. Recall from Section 4.2, Equation 4.3, and [Van der Veen and Bolzan, 1999] that averaging accumulation over the spatial coverage of the radar filters out the spatial noise and measurement errors. Yet, the ice core accumulation signal contains

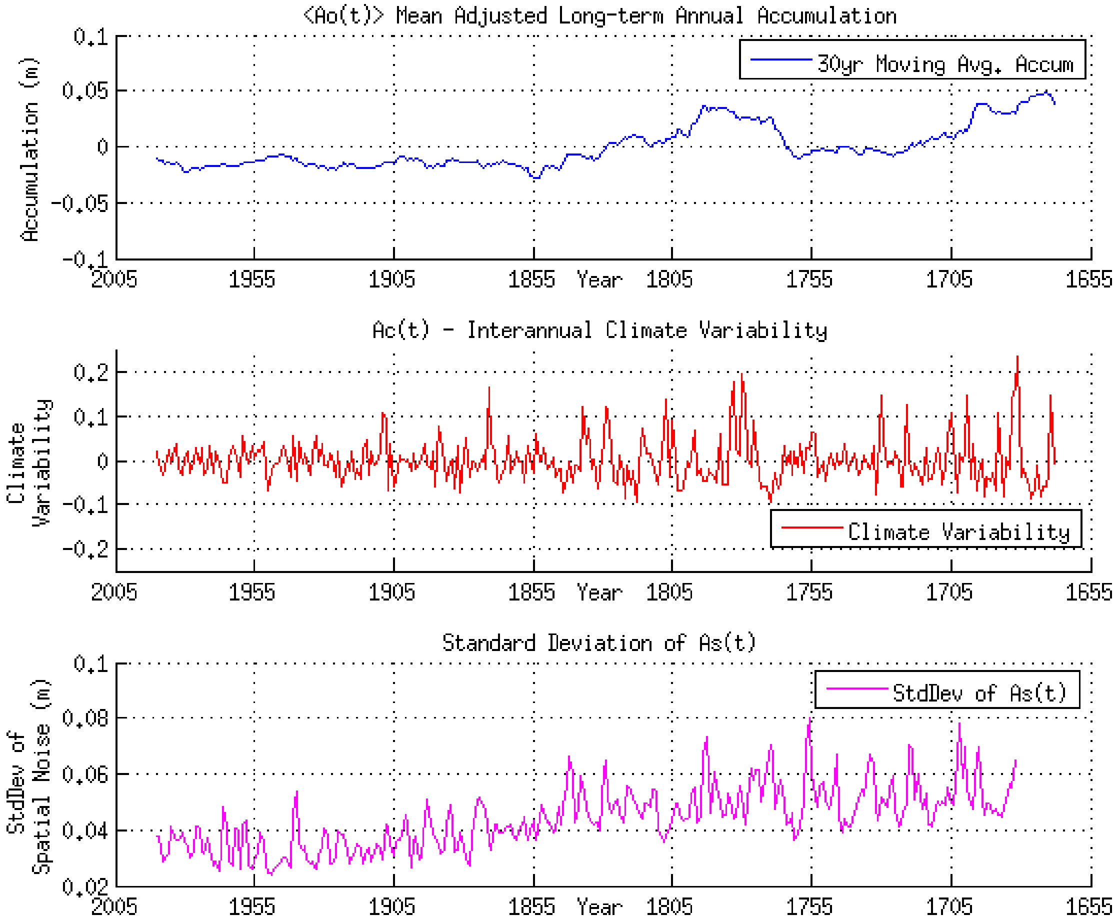

Figure 4.16: Temporal accumulation characteristics
The mean adjusted long-term annual accumulation (upper plot), interannual climate variability (middle plot), and the standard deviation of spatial noise (lower plot) are plotted on a common time span. The mean adjusted accumulation (upper plot) is the 30 yr moving average accumulation, Ao(t), with the mean accumulation rate from 2005–1655, 0.217 m/yr, subtracted out. Interannual variability and variability of spatial noise increase further back in the record.

the contribution from spatial noise (which is filtered out of the radar record). Thus, the standard deviation of the core record should be about $\sqrt{2}$ times that of the radar record. Comparing the standard deviation of the 30 yr moving average accumulation rate for the deep ice core records and the radar accumulation rate, the ice core records have a standard deviation $\sim \sqrt{2}$ times greater than the radar-derived accumulation rate (Figure 4.17). This agrees with the findings of Van der Veen and Bolzan [1999] and lends additional support to the hypothesis that the radar layers are annual.

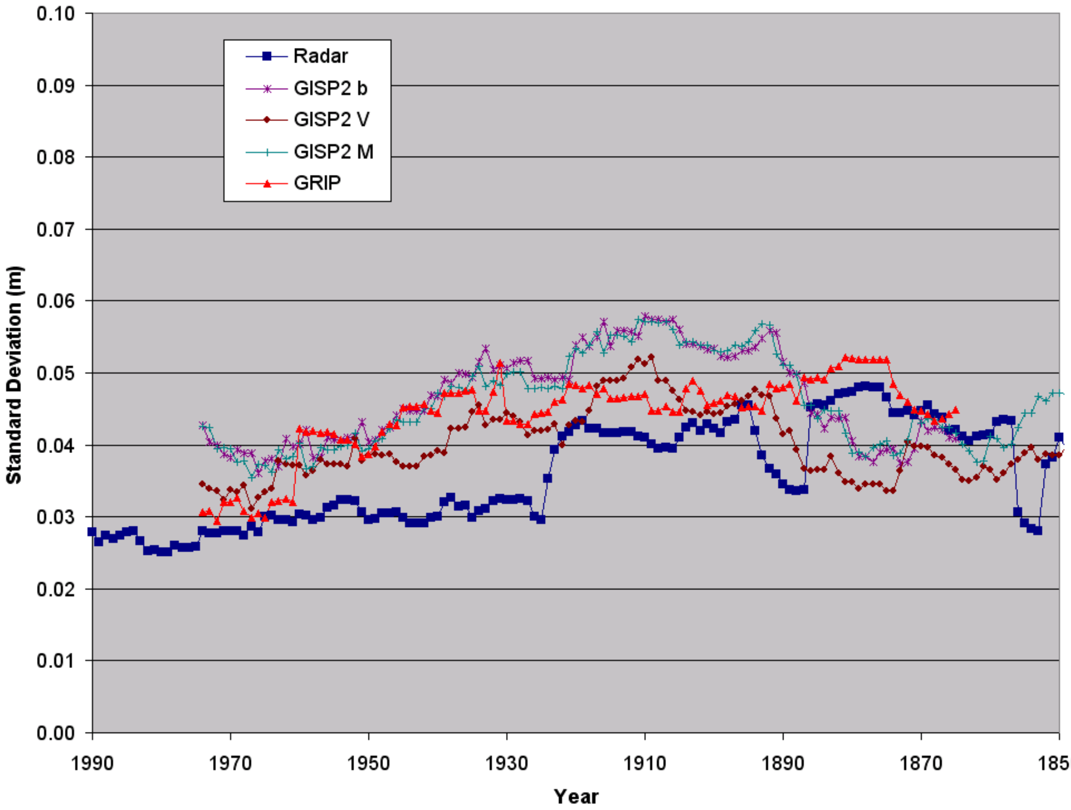

Figure 4.17: Standard deviation of 30-yr moving accumulation
The plot depicts the standard deviation of the accumulation over the running mean window used to calculate the long-term average accumulation $< Ao(x,t) >$. The value at 1975 equals the standard deviation of the accumulation values from 1990–1961.

4.3 Accumulation and Climatic Records

Several climate models and accumulation reconstructions correlate accumulation and temperature [Gregory et al., 2004; Huybrechts et al., 2004; Gregory and Huybrechts, 2006; Huybrechts et al., 2009]. This relationship can be tested by correlating the radar-derived long-term accumulation rate, Ao(t), with coastal Greenland temperature records from the Danish Metrological Institute [Cappelen, 2006]. In-situ temperature records from the Summit region of the ice sheet are too short for a long-term comparison. Coastal temperature data extend back to the late 19th century, allowing for comparisons with the long-term radar accumulation rate from 2005 to 1870 A.D.

Interannual climate variability, Ac(t), is compared with the North Atlantic Oscillation (NAO), the primary mode of interannual climate variability for the North Atlantic Ocean Basin. Though the NAO's influence on accumulation in Greenland is spatially and temporally variable [Mosley-Thompson et al., 2005], the comparison may be useful in assessing the radar-derived climate variability with a known measure of climate variability.

The long-term moving average accumulation, Ao(t), the climate variability, Ac(t), four coastal temperature records available nearest Summit (Upernavik, Ilulissat, Nuuk, and Tasiilaq), and the winter NAO, all plotted on a common timescale, 2005 to 1870 (Figure 4.18).

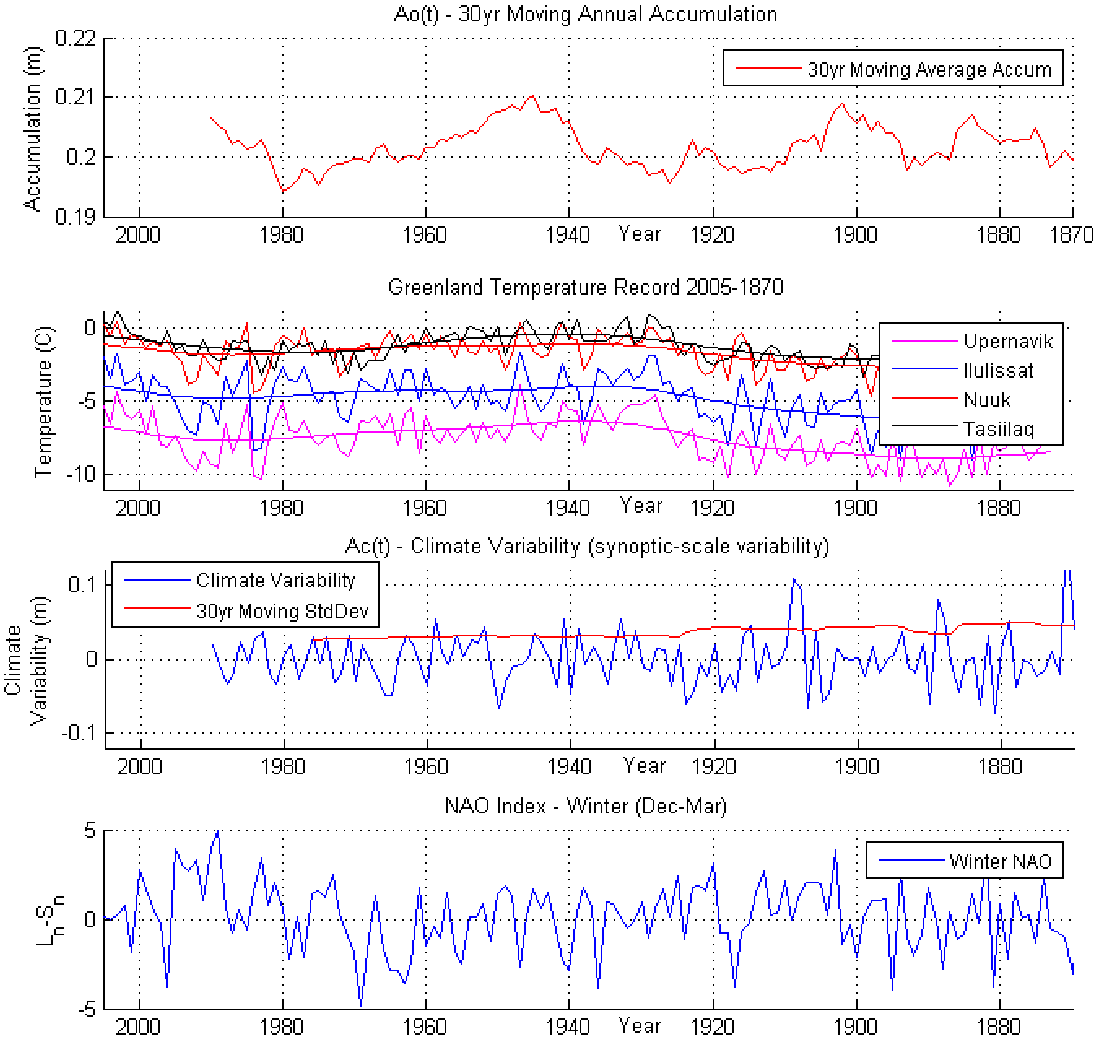

Figure 4.18: Accumulation, temperature, and climate variability
The long-term moving average accumulation Ao(t), Greenland coastal temperature record [Cappelen, 2006], climate variability Ac(t), and the winter North Atlantic Oscilation (NAO) Index [Hurrell, 2009]

The climate variability Ac(t) and the winter NAO have a correlation of r= 0.01, or no linear relation. The poor correlation is not surprising as Mosley-Thompson et al. [2005] found that NAO is not a good predictor of accumulation in central Greenland [Mosley-Thompson et al., 2005]. Moving beyond annual assessments of temperature and climate variability, the relationship between long-term accumulation, Ao(t) is compared with a 30yr moving average of temperature from the four weather stations (Figure 4.19).

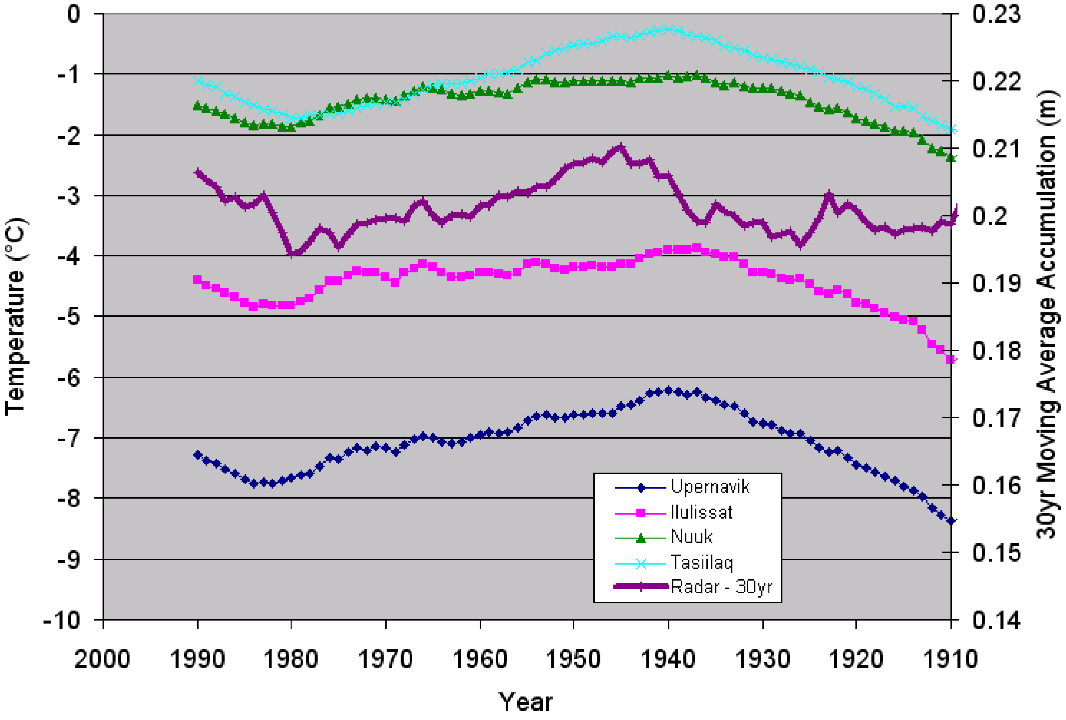

Figure 4.19: Temperature and radar-derived 30yr moving average accumulation Temperature data from four coastal weather stations in Greenland [Cappelen, 2006] are plotted with the 30 yr Moving Average Accumulation derived from the radar data. Note: the left y-axis applies to the four weather stations, the right y-axis applies only to the radar-derived 30 yr Moving Accumulation.

The regional temperature over longer periods and the long-term accumulation rate, Ao(t), correlate better than interannual temperature and climate variability (Table 4.2). This relationship agrees with that of models that correlate large-scale accumulation and temperature [Gregory et al., 2004; Huybrechts et al., 2004; Gregory and Huybrechts, 2006; Huybrechts et al., 2009]. The correlations in Table 4.2 are encouraging but additional accumulation records from the other radar transects, as well as additional temperature records, should be examined to determine the relationship between long-term climate records and radar-derived long-term accumulation, Ao(t).

Table 4.2: Correlation of Radar-derived 30 yr Moving Average Accumulation and coastal temperature data from Figure 4.19

	Upernavik	Ilulissat	Nuuk	Tasiilaq
30yr Radar	0.52	0.45	0.52	0.63

Chapter 5

Conclusions and Future Work

5.1 Overview of significant findings of the thesis

The horizons detected by PRISM's high-frequency FM-CW ground-based radar represent annual markers. The dark and light horizons constitute an annual layer of snow accumulation. Accumulation rates along the radar transect are derived by tracing dark horizons, measuring the thickness between the stratified horizons, and converting this thickness to a water-equivalent accumulation value. Extensive comparison to ice core accumulation rates helps to establish that the radar layers are annual accumulation layers. The accumulation layers are continuous horizontally across the ∼31 km distance of the radar transect. Where ice cores (documenting a 7 cm cylinder of the ice sheet) may have missing years due to wind-scouring, the expansive geographic area covered by the radar eliminates the possibility of "missing" or "extra" layers due to localized drifting or wind conditions.

The radar's resolution allows for the detection of annual layers to an unprecedented depth of 200 m. For this thesis, consecutive annual layers were traced down to a depth of 110 m. Previous research studies calculate accumulation rates based on snow/ice thickness from a few accurately dated prominent layers. The existing studies end up with averaged accumulation rates spanning decades. The year by year accumulation rates produced from this thesis provide a detailed account of accumulation, which is then analyzed to produce climate variability and fluctuations from long-term averages.

The radar layers are established as annual accumulation markers via layer thickness comparison, depth-difference comparison, and connection to volcanic horizons. Using these comparisons to make the assumption that the layers represent annual markers, accumulation rates are derived from the radar layers. The radar derived accumulation rate is then compared to accumulation rates from shallow and deep ice cores in the Summit region of Greenland. If the depth-difference, layer thickness, and volcanic/physical properties comparisons seemed circumstantial, then the ice core and radar accumulation rate comparisons best reinforce the assumption that the layers represent annual markers. Actual amounts of accumulation from ice core and radar records are similar over the 2005–

1653 time period of comparison. The accumulation rates determined from the radar data compare well with ice core accumulation rates (Figure 4.5). Correlations between radar and ice cores are excellent in light of correlation values from similar near-surface studies. Hawley et al. [2008] described a "significant correlation" between chemistry-based and density-based accumulation records concurrently collected (Pearson's $r = 0.38$, for a period of 68 years). If the radar-derived accumulation rate is considered a density-based record and ice core accumulation rates are considered a combination of chemical/physical property based record, the accumulation correlations ranging from 0.24–0.63 are an impressive, if not convincing indication that the radar layers represent annual markers. Considering that the ice core and radar data were not collected concurrently and that these correlations represent single cores compared to the radar, the correlation values become all the more impressive. Since the radar-derived accumulation rate is spatially averaged across the entire radar transect, it makes sense to compare this record to an average of several ice core accumulation rates. Correlations are highest when an average ice core accumulation rate is compared over a 30 year period with the radar-derived accumulation rate (Pearson's r correlation coefficients equal 0.70, Figure 4.7). Correlations decrease as outlier accumulation amounts increase further back (deeper) in the accumulation record. But correlation coefficients remain in the range of core-to-core correlation amounts back to 1850 ($\sim$155 years).

Extending the comparison of annual accumulation rates to longer time periods further depicts radar's strength at determining accumulation rates. The 30yr moving average of radar-derived accumulation correlates well with 30yr moving average ice core accumulation rates (ranging from Pearson's r = 0.48–0.68 for four deep ice core accumulation rates compared over a 138 year period, Figure 4.6). Viewing accumulation over this longer time span reveals that radar-derived accumulation underestimates accumulation compared to the ice cores. Explanations for this underestimate are not entirely clear, but preliminary tests on both annual-layer choice (where the radar horizon is traced) and density-profile choice indicate that annual-layer choice has the more direct influence on radar derived accumulation rates. A detailed investigation of annual-layer tracing location and density-profile choice is beyond the scope of this thesis, but should be conducted prior to future studies involving PRISM accumulation radar data.

The radar-derived accumulation not only provided a regional overview of long-term accumulation, but also gave insight on the spatial variations of accumulation in the Summit region. The radar horizons, continuously traced between the GRIP and GISP2 cores, confirmed the suspected accumulation gradient based on the ice core accumulation rates. This accumulation gradient, analyzed both spatially and temporally, provides a detailed look at accumulation across the radar transect from 2005–1653 A.D. Spatial analysis of the accumulation rates over this period show that an accurate representation of accumulation across the approximately 31km transect can be obtained by averaging accumulation over a horizontal distance of approximately 1000–2000 m (Figure 4.15). Knowing this distance could be useful for future accumulation radar studies conducted around the Summit region. Radar, operated in conjunction with future shallow core drilling or near-surface firn studies, would need to cover at least 1000 m but not more than 2000 m horizontal distance in order to get a regionally representative accumulation rate. From 10 m line in Figure 4.14, it appears that a 10 cm diameter ice core could contain a range of accumulation rates that are not necessarily representative of the actual accumulation rate across the region. Yet, correlations between spatially averaged radar accumulation rates and various ice core accumulation rates indicate that the ice cores are providing a reliable glimpse of accumulation at a specific site (Figures 4.3 4.4 4.5 4.6 4.7). Thus, radar operated within a 1000 m radius of ice cores could help determine how representative the ice core accumulation rate is of the actual regional accumulation rate.

Radar-derived accumulation characteristics such as spatial noise (Figure 4.10) and surface roughness (the amount, variability, and distribution of surface perturbations, Figures 4.11 4.12 4.13) are similar to altimetry derived estimates of surface roughness and spatial noise estimated by Van der Veen et al. [1998, 2009]. The similarity between the results in this thesis and those in Van der Veen et al. [1998, 2009] lend credit to the hypothesis that the layers represent annual accumulation. The further strengthening of the idea that the layers represent accumulation also increases confidence in the spatial and temporal information derived from the accumulation layers.

Examining the radar-derived accumulation rate temporally in relation to climate measurements such as NAO and temperature gives expected results. Temperature correlates reasonably well with accumulation (Table 4.2, Figure 4.19), a relationship supported by several climate models [Gregory et al., 2004; Huybrechts et al., 2004; Gregory and Huybrechts, 2006; Huybrechts et al., 2009]. Accumulation in the Summit region is not expected to correlate well with NAO Mosley-Thompson et al. [2005], and correlation between radar-derived climate variability and NAO reflect this lack of relationship.

5.2 Implications of the thesis for current theories about near surface radar

Existing near-surface radar studies attribute internal reflection horizons to changes in density and conductivity for the depths discussed in this thesis (surface down to 200m) [Kanagaratnam et al., 2004; Spikes et al., 2004; Arcone et al., 2005; Frezzotti et al., 2005; Steinhage et al., 2005; Eisen et al., 2006, 2007]. Comparison of Electrical Conductivity Measurements from the ice cores to the radar layers support that reflection horizons can result from changes in conductivity. But, peaks in ECM recorded within a single ice core do not ensure that an intensely reflecting radar horizon will result from this change in conductivity. With the benefit of concurrently collected ice core and radar data, Arcone et al. [2005] confirmed that at the firn/ice transition, in which density values become constant with increasing depth, weak radar reflections were observed at similar depths. These findings contributed to the theory that radar layers are the result of changes in density. If radar layers are the result of changes in density, and density values below the firn/ice transition are constant, it would then be expected that no reflection of radar data would occur at depths below the firn/ice transition. Yet, the radar layers observed in this thesis extend well below the firn/ice transition. As discussed above, some layers may be due to changes in conductivity from volcanic eruptions or changes in acidity, but can these layers account for all layers observed below the firn/ice transition? There is no apparent change in the thickness, frequency, or intensity of the radar layers near the depth of the observed firn/ice transition in the GRIP and GISP2 deep ice cores. Thus, it seems unlikely that changes in conductivity pick up where the changes in density left off at the firn/ice transition. The radar reflection layers observed in this thesis occur at depths far exceeding the firn/ice transition. Thus, another explanation must be offered for how "density" might be impacting reflection horizons. Around the firn-ice transition, individual snow grains are metamorphosed into solid ice containing nearly spherical bubbles, whose size and appearance varies from summer to winter, causing changes in the visible signal of depth hoar [Alley et al., 1997]. This change in visible signal is the basis for visual stratigraphy analysis of ice cores and borehole optical stratigraphy of boreholes. Empirical tests by Alley et al. [1997] show that the annual signal remains recognizable below the firn-ice transition. Previous near-surface radar studies have not had the power or resolution to detect annual layers below the depths of the firn-ice transition. It therefore follows that the "density" or "conductivity" argument sufficed in explaining the cause of the radar layers. Based on the prevalence of radar layers persisting well below the firn/ice transition, where density is constant, the results from this thesis indicate that the radar layers are caused by a combination of changes in density, conductivity, and air bubble size.

5.3 Limitations of the thesis and recommendations for further research

The primary limitation of this thesis was the limited physical snow property data collected. Two shallow 2m snowpits were dug in conjunction with a separate pulse-wave radar and were not useful for comparison to the FM-CW radar used to collect the data for this thesis [Rink, 2006]. Shallow ice cores drilled during the 2005 field season were not specifically coordinated with the PRISM radar campaign. The deep ice cores used for comparisons, GRIP and GISP2, pre-date the radar data by ∼17 years, thus creating an offset from the radar's 2005 "surface" and the deep ice cores 1988 "surface".

The density profile used to calculate water-equivalent accumulation rates is a combination of several ice density profiles from shallow and deep ice cores. Though ice density profiles fall within a certain range, the small variations are not depicted when using the same composite density profile across the entire radar transect. Using a different density profile to convert accumulation layers into water-equivalent can result in a slightly different accumulation rate (though Hawley et al. [2008] have shown that the choice of a density profile has limited impact on the estimated accumulation rate). The impact of secondary warming periods on changes in dielectric constant is unclear.

In order to overcome the limitations described above and improve upon future near-surface radar surveys, multiple ground truthed data should be collected in conjunction with the remotely sensed radar data. Ground-truthing methods, such as Borehole Optical Stratigraphy, neutron probing, and continuous-flow chemical analysis (all three of which are collected in the process of drilling a shallow ice core) would allow radar and core stratigraphy, and ice core properties (density, ECM, dust, etc.), to be compared on a common time scale. Synchronous collection of this data is the optimal approach that will allow for the eventual determination of which physical, chemical, and other unknown properties and processes are the source of the radar reflections. The results from this thesis indicate that radar-derived accumulation rates present an opportunity to gain a more detailed understanding of accumulation on the Greenland ice sheet.

Bibliography

Ackley, S.F., and T.E. Keliher. 1979. Ice sheet internal radio-echo reflections and associated physical property changes with depth. *J. Geophys. Res.* 84(B10):5675–5680.

Alley, R. B., and B.R. Koci. 1990. Recent warming in central greenland? *Annals of Glaciology* 14:6–8.

Alley, R. B., C. A. Shuman, D. A. Meese, A. J. Gow, K. C. Taylor, K. M. Cuffey, Fitzpatrick J. J., P. M. Grootes, G. A. Zielinski, M. Ram, G. Spinelli, and B. Elder. 1997. Visual-stratigraphic dating of the gisp2 ice core: Basis, reproducibility, and application. *J. Geophys. Res.* 102(C12):26367–26381.

Anklin, M., R. C. Bales, E. Mosley-Thompson, and K. Steffen. 1998. Annual accumulation at two sites in northwest greenland during recent centuries. *Journal Of Geophysical Research-Atmospheres* 103(D22):28775–28783.

Arcone, S.A, V.B. Spikes, and G.S. Hamilton. 2005. Stratigraphic variation within polar firn caused by differential accumulation and ice flow: interpretation of a 400mhz short-pulse radar profile from west antarctica. *Journal of Glaciology* 51(174):407–422.

Arcone, S.A, V.B. Spikes, G.S. Hamilton, and P. A. Mayewski. 2004. Stratigraphic continuity in 400mhz short-pulse radar profiles of firn in west antarctica. *Annals of Glaciology* 39:195–200.

Bamber, J. L., and A. J. Payne. 2004. *Mass balance of the cryosphere*. Cambridge University Press.

Banta, J.R., and J. R. McConnell. 2007. Annual accumulation over recent centuries at four sites in central greenland. *J. Geophys. Res.* 112(D10114).

Bogorodsky, V.V., V.I. Pozdnynak, G.V. Trepov, and A.M. Shremetâyev. 1982. Radar sounding measurements of the thickness of annual snow strata in the antarctic. *Doklady of the Academy of Sciences of the U.S.S.R. Earth science sections* 264(4):909–911.

Bolzan, J., and M. Strobel. 1994. Accumulation-rate variations around summit, greenland. *Journal of Glaciology* 40:56–66.

Box, J. E. 2002. Survey of greenland instrumental temperature records: 1873-2001. *International Journal of Climatology* 22:1829–1847.

Box, J. E., D. H. Bromwich, and L. S. Bai. 2004. Greenland ice sheet surface mass balance 1991 - 2000: Application of polar mm5 mesoscale model and in situ data. *J. Geophys. Res.* 109(D16105).

Bromwich, D. H., F.M. Robasky, R.A. Keen, and J.F. Bolzan. 1993. Modeled variations of precipitation over the greenland ice sheet. *Journal of Climate* 6:1253–1268.

Burt, J.E., and G.M. Barber. 1996. *Elementary statistics for geographers*. 2nd ed. New York: The Guilford Press.

University of California-Merced, California. 2008. About summit camp home.

Cappelen, J. 2006. Dmi annual climate data collection 1873-2005, denmark, the faroe islands and greenland. Tech. Rep., Danish Meteorological Institute.

Chuah, T.S., S.P Gogineni, C. Allen, and B. Wohletz. 1996. Radar thickness measurements over the northern part of the greenland ice sheet. Tech. Rep., University of Kansas Center for Research Inc. Radar Systems and Remote Sensing Laboratory.

Clausen, H. B., C.U. Hammer, C. S. Hvidberg, D. Dahl-Jensen, J. P. Steffensen, J. Kipfstuhl, and M. Legrand. 1997. A comparison of the volcanic records over the past 4000 years from the greenland ice core project and dye 3 greenland ice cores. *J. Geophys. Res.* 102(C12):26,707 – 26,723.

Clough, J.W. 1977. Radio-echo sounding: reflections from internal layers in ice sheets. *Journal of Glaciology* 18(78):3–14.

Colbeck, S. C. 1983. Snow particle morphology in the seasonal snow cover. *Bulletin of the American Meteorological Society* 64(6):602–609.

Colbeck, S.C., and B.J. Jamieson. 2001. The formation of faeted layers above crusts. *Cold Regions Science and Technology* 33.

Craig, H. 1961. Isotopic variations in meteoric waters. *Science* 133(3465):1702–1703.

Cuffey, K. M., and G.D. Clow. 1997. Temperature, accumulation, and ice sheet elevation in central greenland through the last deglacial transition. *Journal of Geophysical Research* 102(C12):26,383–26,396.

Dahl-Jensen, D., N. S. Gundestrup, K. Keller, S. J. Johnsen, S. P. Gogineni, C. T. Allen, T. S. Chuah, H. Miller, S. Kipfstuhl, and E. D. Waddington. 1997. A search in north greenland for a new ice-core drill site. *Journal Of Glaciology* 43(144):300–306.

Dahl-Jensen, D., S. J. Johnsen, C.U. Hammer, H. B. Clausen, and J. Jouzel. 1993. Past accumulation rates derived from observed annual layers in the grip ice core from summit, central greeland. *Ice in the Climate System, NATO ASI Ser. I* 12:517–532. Springer-Verlag, New York.

Dansgaard, W. 1964. Stable isotope in precipitation. *Tellus* 16(4):436–468.

Dansgaard, W., S. J. Johnsen, H. B. Clausen, and N. Gundestrup. 1973. Stable isotope glaciology. *Meddedelser om GrÃ¸nland* 197(2).

Dethloff, K., M. Schwager, J.H. Christensen, S. Kiilsholm, A Rinke, W. Dorn, Jung-RothenhÃ¤usler, H. Fischer, S. Kipfstuhl, and H. Miller. 2002. Recent greenland accumulation estimated from regional climate model simulations and ice core analysis. *Journal Of Climate* 15(19):2821–2832.

Eisen, O., M. Frezzotti, C. Genthon, E. Isaksson, O. Magand, M. R. van den Broeke, D.A. Dixon, A. Ekaykin, P. Holmlund, T. Kameda, L. KarlÃ¶f, S. Kaspari, V.Y. Lipenkov, H. Oerter, S. Takahashi, and D. G. Vaughan. 2008. Ground-based measurements of spatial and temporal variability of snow accumulation in east antarctica. *Reviews of Geophysics* 46(RG2001).

Eisen, O., I. Hamann, J. Kipfstuhl, D. Steinhage, and F. Wilhelms. 2007. Direct evidence for continuous radar reflector originating from changes in crystal-orientation fabric. *The Cryosphere* 1(1):1–10.

Eisen, O., U. Nixdorf, F. Wilhelms, and D.H.M. Millar. 2002. Electromagnetic wave speed in polar ice: validation of the common-midpoint technique with high-resolution dielectric-profiling and g-density measurements. *Annals of Glaciology* 34:150–156.

Eisen, O., U. Nixdorf, F. Wilhelms, and H. Miller. 2004. Age estimates of isochronous reflection horizons by combining ice core, survey, and synthetic radar data. *J. Geophys. Res.* 109(B04106).

Eisen, O., F. Wilhelms, D. Steinhage, and J. Schwander. 2006. Improved method to determine radio-echo sounding reflector depths from ice-core profiles of permittivity and conductivity. *Journal Of Glaciology* 52(177):299–310.

Fischer, H., D. Wagenbach, M. Laternser, and W. Haeberli. 1995. Glaciometerological and isotopic studies along the egig line, central greenland ice sheet. *Journal of Glaciology* 41: 515–527.

Fisher, D. A., N. Reeh, and H. B. Clausen. 1985. Stratigraphic noise in time series derived from ice cores. *Annals of Glaciology* 7:76–83.

Frezzotti, M., M. Pourchet, O. Flora, S. Gandolfi, M. Gay, S. Urbini, C. Vincent, S. Becagli, R. Gragnani, M. Proposito, M. Severi, R. Traversi, R. Udisti, and M. Fily. 2005. Spatial and temporal variability of snow accumulation in east antarctica from traverse data. *Journal of Glaciology* 51(172):113–124.

Frezzotti, M., S. Urbini, M. Proposito, C. Scarchilli, and S. Gandolfi. 2007. Spatial and temporal variability of surface mass balance near talos dome, east antarctica. *J. Geophys. Res.* 112(F02032).

Fujita, S., and S. Mae. 1994. Causes and nature of ice-sheet radio-echo internal reflections estimated fromthe dielectric properties of ice. *Annals of Glaciology* 20:80–86.

Fujita, S., H. Maeno, T. Furukawa, and K. Matsuoka. 2002. Scattering of vhfradio waves from within the top 700m of the antarctic ice sheet and its relation to the depositional environment: a case-study along the syowa-mizuho-dome fuji traverse. *Annals of Glaciology* 34:157–164.

Fujita, S., H. Maeno, and K. Matsuoka. 2006. Radio-wave depolarization and scattering within ice sheets:. *Journal of Glaciology* 52(178):407–424.

Fujita, S., H. Maeno, S. Uratsuka, T. Furukawa, S. Mae, Y. Fujii, and O. Watanabe. 1999. Nature of radio-echo layering in theantarctic ice sheet detected by a two-frequency experiment. *J. Geophys. Res.* 104(B6):13013–13024.

Fujita, S., T. Matsuoka, T. Ishida, K. Matsuoka, and S. Mae. 2000. A summary of the complex dielectric permittivity of ice in the megahertz range and its application for radar sounding of polar ice sheets. In *Physics of ice core records*, ed. T. Hondoh, 185–212. Sapporo, Japan: Hokkaido University Press.

GISP2. 1997a. Greenland summit ice cores cd-rom - gisp2 accumulation rate history.

———. 1997b. Greenland summit ice cores cd-rom - gisp2 b core depth age scale.

———. 1997c. Greenland summit ice cores cd-rom - gisp2 electrical conductivity measurements.

———. 1997d. Greenland summit ice cores cd-rom - gisp2 insoluble microparticles.

———. 1997e. Greenland summit ice cores cd-rom - gisp2 meltwater laser-light scattering dust concentration profile data.

———. 1997f. Greenland summit ice cores cd-rom - gisp2 stratigraphy.

———. 1997g. Greenland summit ice cores cd-rom - gisp2 visual stratigraphy.

Gogineni, P., D. Braaten, C. Allen, J. Paden, T. Akins, P. Kanagaratnam, K. Jezek, G. Prescott, G. Jayaraman, V. Ramasami, C. Lewis, and D. Dunson. 2007. Polar radar for ice sheet measurements (prism). *Remote Sensing of Environment - Special Issue: Cryosphere* 111:204–211.

Gregory, J.M., and P. Huybrechts. 2006. Ice-sheet contributions to future sea-level change. *Philos.Trans. R. Soc. London, Ser. A* 364:1709–1731.

Gregory, J.M., P. Huybrechts, and S.C.B. Raper. 2004. Threatened loss of the greenland ice-sheet. *Nature* 428.

GRIP. 1997a. Greenland summit ice cores cd-rom - grip accumulation rates ftp://ftp.ncdc.noaa.gov/pub/data/paleo/icecore/greenland/summit/grip/physical/gripacum.txt.

———. 1997b. Greenland summit ice cores cd-rom - grip electrical conductivity measurements.

Gudmandsen, P. 1975. Layer echos in polar ice sheets. *Journal of Glaciology* 15(73):95–101.

Hammer, C. 1986. Ice-core dating of the pleistocene holocene boundary applied to a calibration of the c-14 time scale. *Radiocarbon* 28(2a).

Harrison, C.H. 1973. Radio echo sounding of horizontal layers in ice. *Journal of Glaciology* 12(66):383–397.

Hawley, R. L., E. M. Morris, R. Cullen, U. Nixdorf, A. P. Shepherd, and D. J. Wingham. 2006. Asiras airborne radar resolves internal annual layers in the dry-snow zone of greenland. *Geophysical Research Letters* 33(4). L04502.

Hawley, R. L., E. M. Morris, and J.R. McConnell. 2008. Intruments and methods rapid techniques for determining annual accumulation applied at summit, greenland. *Journal Of Glaciology* 54(188):839–845.

Hempel, L., F. Thyssen, N. Gundestrup, H. B. Clausen, and H. Miller. 2000. A comparison of radio-echo sounding data and electrical conductivity of the grip ice core. *Journal Of Glaciology* 46(154):369–374.

Hurrell, J. 2009. Winter (dec-mar) station based nao index.

Huybrechts, O., P. Rybak, F. Pattyn, and D. Steinhage. 2009. Past and present accumulation rate reconstruction along the dome fuji-kohnen radio echo sounding profile, dronning maud land, east antarctica. *Annals of Glaciology* 50(51):112–120.

Huybrechts, P., J.M. Gregory, I. Janssens, and M. Wild. 2004. Modelling antarctic and greenland volume changes during the 20th and 21st centuries forced by gcm time slice integrations. *Global And Planetary Change* 42:83–105.

Jacobel, R. W., and S. M. Hodge. 1995. Radar internal layers from the greenland summit. *Geophysical Research Letters* 22(5):587–590.

Johnsen, S. J., H.B. Clausen, W. Dansgaard, K. Fuhrer, N.S. Gundestrup, C.U. Hammer, P. Iversen, J. Jouzel, B. Stauffer, and J. P. Steffensen. 1992. Irregular glacial interstadials recorded in a new greenland ice core. *Nature* 359:311–313.

Kanagaratnam, P. 2002. Airborne radar for high-resolution mapping of internal layers in glacial ice to estimate accumulation rate. phd dissertation. Ph.d., University of Kansas.

Kanagaratnam, P., S. P. Gogineni, V. Ramasami, and D. Braaten. 2004. A wideband radar for high-resolution mapping of near-surface internal layers in glacial ice. *Ieee Transactions On Geoscience And Remote Sensing* 42(3):483–490.

Kapsner, W.R., R. B. Alley, C. A. Shuman, S. Anandakrishnan, and P.M. Grootes. 1995. Dominant influence of atmospheric circulation on snow accumulation in greenland over the past 18,000 years. *Nature* 373:52–54.

Kingsley, S., and S. Quegan. 1992. *Understanding radar systems.* Raleigh, N.C.: SciTech Publishing Inc.

Kovacs, A., A. J. Gow, and R.M. Morey. 1995. The in-situ dielectric constant of polar firn revisited. *Cold Regions Science and Technology* 23:245–256.

LaChapelle, E.R. 1992. *Field guide to snow crystals.* 2nd ed. International Glaciological Society.

Matsuoka, K., H. Maeno, S. Uratsuka, S. Fujita, T. Furukawa, and O. Watanabe. 2002. A ground-based, multi-frequency ice-penetrating radar system. *Annals of Glaciology* 34: 171–176.

Meese, D. A., A. J. Gow, R. B. Alley, G. A. Zielinski, P. M. Grootes, M. Ram, K. C. Taylor, P. A. Mayewski, and J. F. Bolzan. 1997. The greenland ice sheet project 2 depth-age scale: Methods and results. *J. Geophys. Res.* 102(C12):26411–26423.

Meese, D. A., A. J. Gow, P. Grootes, P. A. Mayewski, M. Ram, M. Stuiver, K. C. Taylor, E. D. Waddington, and G. A. Zielinski. 1994. The accumulation record from the gisp2 core as an indicator of climate-change throughout the holocene. *Science* 266(5191):1680–1682.

Millar, D.H.M. 1981. Radio-echo layering in polar ice sheets and past volcanic activity. *Nature* 292(5822):441–443.

Moore, J. C. 1988. Dielectric variability of a 130m antarctic ice core: implications for radar sounding. *Annals of Glaciology* 11:95–99.

Mosley-Thompson, E., C.R. Readinger, P. Craigmile, L. G. Thompson, and C.A. Calder. 2005. Regional sensitivity of greenland precipitation to nao variability. *Geophysical Research Letters* 32(L24707).

NASA. 2009. Paleoclimatology: The oxygen balance.

Paren, J. G., and G. de Q. Robin. 1975. Internal reflections in polar ice sheets. *Journal of Glaciology* 14(71).

Parthasarathy, Rohit. 2003. A fine-resolution radar for near-surface layer mapping. M.s., The University of Kansas.

Paterson, W.S.B. 1994. *The physics of glaciers.* 3rd ed. Oxford, New York, Tokyo: Pergamon.

Pfeffer, W.T., and R. Mrugala. 2002. Temperature gradient and initial snow density as controlling factors in the formation and structure of hard depth hoar. *Journal of Glaciology.* 48(163).

Price, R.C., R.B. Stewart, J.D. Woodhead, and I.E.M. Smith. 1999. Petrogenesis of high-k arc magmas: Evidence from egmont volcano, north island, new zealand. *Journal of Petrology* 40(1):167 – 197.

Rink, Timothy P. 2006. Design and evaluation of a fine-resolution radar for mapping near-surface layers using plane-waves. Ph.D. thesis, University of Kansas.

Robin, G. de Q., S. Evans, and J.T. Bailey. 1969. Interpretation of radio echo sounding in polar ice sheets. *Philos.Trans. R. Soc. London, Ser. A* 265(1166):437–505.

Robin, G. de Q., and D.H.M. Millar. 1982. Flow of ice sheets in the vicinity of subglacial peaks. *Annals of Glaciology* 3:290–294.

Shuman, C. A., K. Steffen, J. E. Box, and C.R. Stearns. 2001. A dozen years of temperature observations at the summit: Central greenland automatic weather stations 1987-99. *Journal of Applied Meteorology* 40(4):741–752.

Spikes, V.B., G.S. Hamilton, S.A Arcone, S. Kaspari, and P. Mayewski. 2004. Variability in accumulation rates from grp profiling on the west antarctic plateau. *Annals of Glaciology* 39:238–244.

Steffen, K., W. Abdalati, and I. Sherjal. 1999. âfaceted crystal formation in the northeast greenland low-accumulation region.â. *Journal of Glaciology.* 45(149).

Steinhage, D., O. Eisen, and H. B. Clausen. 2005. Regional and temporal variation of accumulation around northgrip derived from ground-penetrating radar. *Annals of Glaciology* 42:326–330.

Survey, British Antarctic. 1997. Greenland ice core project (grip).

Taylor, K. C., R. B. Alley, R.J. Fiacco, P.M. Grootes, G. W. Lamorey, P. A. Mayewski, and M.J. Spencer. 1992. Ice core dating and chemistry by direct current electrical conductivity. *Journal of Glaciology* 38:325–332.

Taylor, K. C., R. B. Alley, G. W. Lamorey, and P. Mayewski. 1997. Electrical measurements on the greenland ice sheet project 2 core. *Journal Of Geophysical Research-Oceans* 102(C12):26511–26517.

Taylor, K. C., C. U. Hammer, R. B. Alley, H. B. Clausen, D. Dahljensen, A. J. Gow, N. S. Gundestrup, J. Kipfstuhl, J. C. Moore, and E. D. Waddington. 1993. Electrical-conductivity measurements from the gisp2 and grip greenland ice cores. *Nature* 366(6455):549–552.

Vaughan, D. G., H. F. J. Corr, C. S. M. Doake, and E. D. Waddington. 1999. Distortion of isochronous layers in ice revealed by ground-penetrating radar. *Nature* 398(6725): 323–326.

Van der Veen, C. J. 1993. Interpretation of short-term ice-sheet elevation changes inferred from satellite altimetry. *Climate Change* 23:383–405.

———. 2009a. Personal communication: assumptions about synoptic scale variability.

———. 2009b. Personal communication: Summit greenland accumulation characteristics.

Van der Veen, C. J., Y. Ahn, B.M. Csatho, E. Mosley-Thompson, and W.B. Krabill. 2009. Surface roughness over the northern half of the greenland ice sheet from airborne laser altimetry. *Journal of Geophysical Research* 114(F01001).

Van der Veen, C. J., and J.F. Bolzan. 1999. Interannual variability in net accumulation on the greenland ice sheet: Observations and implications for mass balance measurements. *Journal of Geophysical Research* 104(D2):2009–2014.

Van der Veen, C. J., W.B. Krabill, B.M. Csatho, and J.F. Bolzan. 1998. Surface roughness of the greenland ice sheet from airborne laser altimetry. *Geophysical Research Letters* 25(20):3887–3890.

Van der Veen, C. J., E. Mosley-Thompson, K. C. Jezek, M. Whillans, and J. F. Bolzan. 2001. Accumulation rates in south and central greenland. *Polar Geography* 25(2):79–162.

Vinther, B. 2008a. Personal communication: Firn compaction model/adjustment.

———. 2008b. Personal communication: Unpublished grip annual ecm data on the gicc05 time scale.

Vinther, B.M., H. B. Clausen, S. J. Johnsen, S. O. Rasmussen, K. K. Andersen, S.L. Buchardt, D. Dahl-Jensen, I.K. Seierstad, M. L. Siggaard-Andersen, J. P. Steffensen, A. Svensson, J. Olsen, and J. Heinemeier. 2006. A synchronized dating of three greenland ice cores throughout the holocene. *J. Geophys. Res.* 111(D13102).

Zielinski, G. A. 1995. Stratospheric loading and optical depth estimates of explosive volcanism over the last 2100 years derived from the greenland ice sheet project 2 ice core. *J. Geophys. Res.* 100(D10):20,937 – 20,955.